Scuola Normale Superiore
Classe di Scienze
PhD in Chemistry

Theoretical Models for the Calculation of Electric Properties and Raman Spectra of Molecules in Solution

Candidate:
Franco Egidi

Supervisors:
Prof. Vincenzo Barone
Prof. Chiara Cappelli

Academic Year 2013-2014

Preface

This thesis documents part of the work I have performed during my three years of graduate school at the Scuola Normale Superiore in Pisa, under the supervision of prof Vincenzo Barone and prof Chiara Cappelli.

The leitmotif of my work has been the combination of anharmonic vibrational and solvation effects in the *ab-initio* calculation of molecular properties. More in detail, anharmonicity was treated using vibrational perturbation theory, while for solvent effects we based our discussion on the Polarizable Continuum Model. Though the considerations that can be made are largely independent of the chosen electronic structure method, we mostly relied on Density Functional Theory (DFT) and Time-Dependent DFT to deal with the electronic part of the problem.

The first three chapters briefly present some of the underlying theory. Chapter 1, in particular, deals with the theory of Raman spectroscopy, chapter 2 presents the basis of vibrational perturbation theory, while chapter 3 gives an introduction on the solvation model employed, with an emphasis on the direct interaction between the environment and the electromagnetic radiation and on the dynamical aspects of solvation.

The remaining chapters present the numerical results. Chapter 4 focuses on the calculation of electric properties such such as polarizabilities,[1] chapter 5 deals with spectroscopic properties like infra-red,[2] and non-resonant Raman, while chapter 6 confronts the problem of calculating Raman intensities under resonance conditions.[3]

During my PhD I also did some additional work on other types of molecular properties, though they didn't quite make the final cut of the thesis manuscript. These include purely magnetic properties studied in the context of Nuclear Magnetic Resonance and Electron Paramagnetic Resonance spectroscopy,[4] as well as mixed electric-magnetic properties such as optical rotations.[5,6]

The most merciful thing in the world, I think, is the inability of the human mind to correlate all its contents. We live on a placid island of ignorance in the midst of black seas of infinity, and it was not meant that we should voyage far. The sciences, each straining in its own direction, have hitherto harmed us little; but some day the piecing together of dissociated knowledge will open up such terrifying vistas of reality, and of our frightful position therein, that we shall either go mad from the revelation or flee from the light into the peace and safety of a new dark age.

H.P. Lovecraft, *The Call of Cthulhu* (1926)

Contents

Chapter 1

Introduction

1.1 The nature of the Raman effect

Raman scattering can be defined as the inelastic scattering of an electromagnetic radiation by a molecular system.[7] Raman spectroscopy makes use of this effect to study the structure and properties of the systems responsible for the scattering, as well as for analytical purposes. The effect was discovered by Sir Chandrasekhara Venkata Raman in 1928,[8] who later earned the Nobel Prize for his work. One of the peculiar characteristics of the Raman effect is that it is *non-linear*, i.e. the frequency of oscillation of the scattered radiation is different than that of the incident radiation. The analogous phenomenon in which there is no change in energy of the radiation is instead called *Rayleigh scattering*, named after its discoverer, Lord Rayleigh. A Raman experiment involves the illumination of the sample by a laser source for extended periods of time. The radiation scattered along a direction which depends on the particular experimental configuration is collected, separated into its monochromatic components, and the intensity is measured as a function of the frequency is measured, long enough to ensure a good signal to noise ratio. In Raman scattering, the energy difference between the two radiations is often called *Raman shift* and, more in detail, it is referred to as *Stokes shift* if it is negative, and *anti-Stokes shift* if it is positive. In Stokes shift the scattered radiation

has less energy than the incident one and, in order to obey the energy conservation principle, this difference has to be absorbed by the molecular system. Indeed (in most cases) it is observed that if the intensity of the scattered radiation is plotted against the Raman shift, generating the Raman spectrum, a series of peaks appear, and their positions correspond to those observed in the Infra Red (IR) spectrum of the same system, which suggests that the expended energy has in fact been absorbed by the vibrational modes of the molecule. Contrary to IR spectroscopy however, the radiation usually employed in Raman spectroscopy lies in the visible range of the electromagnetic spectrum, which is usually associated with electronic (or vibronic) transitions rather than purely vibrational ones and in fact, as will be shown below, Raman spectroscopy (especially under resonance conditions) can be regarded as both an electronic and a vibrational phenomenon.

Even though Raman and IR spectroscopies both provide information on the vibrational structure of the molecule, from the experimental point of view, Raman spectroscopy can be very advantageous.[7] The main difficulty concerning IR spectra is that many common solvents (including water) and the glassware used in chemical laboratories strongly absorb IR radiation, therefore IR spectra are often recorded by placing the sample between plates made of salts such as sodium chloride. Aside from the laborious sample preparation, the difficulty associated with recording spectra of molecules in a solvated environment may preclude the study of systems whose solvated state is the most natural environment, such as biological molecules. In addition, the well-known selection rules for IR spectroscopy dictate that only the molecular vibrations along which there is a change in electric dipole moment give a non-zero intensity. The corresponding selection rule for Raman spectroscopy involves the polarizability instead of the dipole moment, which is a much less stringent condition. Raman spectra do not present such difficulties, however, being a higher-order phenomenon, the scattered intensity is naturally very low, therefore the source of the incident radiation must be much stronger that that required for IR spectroscopy. Lasers are commonly used in Raman

instrumentation, driving up the cost of the equipment, compared with the relatively inexpensive IR spectrometers. In addition, common laser sources are not continuously tunable to different frequencies, which can be problematic if one is interested in exposing resonance phenomena or recording a Raman excitation profile, i.e. a plot of the scattered intensity against the frequency of the incident radiation.

In the following sections the nature of the Raman effect will be analyzed in depth from a theoretical point of view, following the treatement by Long.[7]

1.2 The origin of second-order effects

The non-linearity of Raman scattering signals that it must be a higher-order phenomenon with respect to one-photon absorption and emission. For the sake of completeness, the derivation of the Raman effect from the perturbation treatment of the time-dependent Schrödinger equation will here be briefly reviewed.

Let us consider a molecular system described by its Hamiltonian operator $\hat{H}$ under the influence of a monochromatic electromagnetic radiation of frequency ω. For Raman scattering to emerge, we only need consider the electric component of the light-matter interaction[9] (the modeling of Raman Optical Activity, its chiral analog, would instead require us to keep other terms, such as those mediated by the magnetic field and the electric field gradient).[10] The perturbation can therefore be expressed by means of an operator $\hat{V}$ of the following form:

$$\hat{V} = -\mu \cdot \frac{\tilde{E}\, \mathrm{e}^{-i\omega t} + \tilde{E}^{*}\, \mathrm{e}^{i\omega t}}{2} = \hat{V}(-\omega) + \hat{V}(\omega) \tag{1.1}$$

Where μ is the electric dipole moment operator of the system and $\tilde{E}$ represents the electric field operator. In quantum mechanics the time evolution of a physical system is governed by the time dependent Schrödinger

equation:

$$i\hbar\frac{\partial}{\partial t}|\Psi(t)\rangle = (\hat{H}+\hat{V})|\Psi(t)\rangle \tag{1.2}$$

In the following treatment we shall only be concerned with the evolution of exact states, and will express the results in terms of linear combinations of exact eigenstates of the unperturbed Hamiltonian. The time evolution of the system may then be expressed as a perturbation series. To prove this statement it is useful to work in the so-called interaction picture in which one operates the following transformation:

$$|\Psi(t)\rangle_{\mathrm{I}} = \mathrm{e}^{i\hat{H}(t-t_0)/\hbar}\,|\Psi(t)\rangle \tag{1.3}$$

by inserting this into the Schrödinger equation one easily obtains:

$$i\hbar\frac{\partial}{\partial t}|\Psi(t)\rangle_{\mathrm{I}} = \mathrm{e}^{i\hat{H}(t-t_0)/\hbar}\,\hat{V}\,\mathrm{e}^{-i\hat{H}(t-t_0)/\hbar}\,|\Psi(t)\rangle_{\mathrm{I}} = \hat{V}_{\mathrm{I}}(t)|\Psi(t)\rangle_{\mathrm{I}} \tag{1.4}$$

The evolution of the wavefunction may be expressed through an appropriate time evolution operator defined by:

$$|\Psi(t)\rangle = \hat{U}(t,t_0)|\Psi(t_0)\rangle \tag{1.5}$$

which, in the interaction picture, becomes:

$$|\Psi(t)\rangle_{\mathrm{I}} = \mathrm{e}^{i\hat{H}_0(t-t_0)/\hbar}\,\hat{U}(t,t_0)\,\mathrm{e}^{-i\hat{H}(t-t_0)/\hbar}\,|\Psi(t_0)\rangle_{\mathrm{I}} = \hat{U}_{\mathrm{I}}(t,t_0)|\Psi(t_0)\rangle_{\mathrm{I}} \tag{1.6}$$

This may be used to rewrite the Schrödinger equation in terms of $\hat{U}_{\mathrm{I}}$ and $|\Psi(t_0)\rangle$. Since the equation remains valid irrespective of the particular initial state, the ket may be dropped and one is left with an equation involving only the operators:

$$i\hbar\frac{\partial}{\partial t}\hat{U}_{\mathrm{I}}(t,t_0) = \hat{V}_{\mathrm{I}}(t)\hat{U}_{\mathrm{I}}(t,t_0) \tag{1.7}$$

Integrating both sides, with $\hat{U}_{\mathrm{I}}(t_0, t_0) = 1$, yields:

$$\hat{U}_{\mathrm{I}}(t, t_0) = 1 - \frac{i}{\hbar} \int_{t_0}^{t} \hat{V}_{\mathrm{I}}(t_1) \hat{U}_{\mathrm{I}}(t_1, t_0) \, \mathrm{d}\, t_1 \tag{1.8}$$

which, by substituting the obtained expression for the evolution operator into itself, leads to the Dyson series:

$$\hat{U}_{\mathrm{I}}(t, t_0) = 1 - \frac{i}{\hbar} \int_{t_0}^{t} \hat{V}_{\mathrm{I}}(t_1) \, \mathrm{d}\, t_1 - \frac{1}{\hbar^2} \int_{t_0}^{t} \int_{t_0}^{t_1} \hat{V}_{\mathrm{I}}(t_1) \hat{V}_{\mathrm{I}}(t_2) \, \mathrm{d}\, t_2 \, \mathrm{d}\, t_1 + \dots \tag{1.9}$$

The term linear in the perturbation may be developed to yield the transition amplitudes for one-photon absorption and emission. Raman scattering may be found by developing the second order term.

To expose the Raman effect we must prove that the probability of going from an initial stationary state $|n\rangle \, \mathrm{e}^{-i\omega_n (t-t_0)}$ to a final stationary state $|m\rangle \, \mathrm{e}^{-i\omega_m (t-t_0)}$ is non-zero, which means proving that the perturbed wavefunction has components in the desired final state:

$$|\Psi(t)\rangle = \hat{U}(t, t_0) |\Psi(t_0)\rangle = \hat{U}(t, t_0) |n\rangle \tag{1.10}$$

$$|\Psi(t)\rangle = \sum_j |j\rangle \, \mathrm{e}^{-i\omega_j (t-t_0)} \, c_j(t) \tag{1.11}$$

Note that since the evolution operator is unitary, if the initial state is normalized so will be the time dependent wavefunction. The coefficients of the expansion, can be found using the time evolution operator:

$$\begin{aligned} c_m(t) &= \langle m | \hat{U}(t, t_0) | n \rangle \, \mathrm{e}^{i\omega_{mn}(t-t_0)} = \\ &= \langle m | \, \mathrm{e}^{-i\hat{H}_0 (t-t_0)/\hbar} \, \hat{U}_{\mathrm{I}}(t, t_0) \, \mathrm{e}^{i\hat{H}_0 (t-t_0)/\hbar} \, | n \rangle \, \mathrm{e}^{i\omega_{mn}(t-t_0)} = \\ &= \langle m | \hat{U}_{\mathrm{I}}(t, t_0) | n \rangle \end{aligned} \tag{1.12}$$

The zeroth term in the expansion of the evolution operator would give a zero transition probability for different states (a stationary state remains unchanged in the absence of a perturbation). The first-order term is easily

developed:

$$\begin{aligned}
\langle m|\hat{U}_{\mathrm{I}}^{(1)}(t,t_0)|n\rangle &= -\frac{i}{\hbar}\int_{t_0}^{t}\langle m|\hat{V}_{\mathrm{I}}(t_1)|n\rangle \,\mathrm{d}\,t_1 = \\
&= -\frac{i}{\hbar}\int_{t_0}^{t}\langle m|\,\mathrm{e}^{i\hat{H}(t_1-t_0)/\hbar}\,\hat{V}\,\mathrm{e}^{-i\hat{H}(t_1-t_0)/\hbar}\,|n\rangle \,\mathrm{d}\,t_1 = \\
&= -\frac{i}{\hbar}\langle m|\hat{V}|n\rangle\int_{t_0}^{t}\mathrm{e}^{i\omega_{mn}(t_1-t_0)}\,\mathrm{d}\,t_1 = \\
&= -\frac{1}{\hbar}\langle m|\hat{V}(-\omega)|n\rangle\frac{\mathrm{e}^{i(\omega_{mn}-\omega)(t-t_0)}-1}{\omega_{mn}-\omega} \\
&\quad -\frac{1}{\hbar}\langle m|\hat{V}(+\omega)|n\rangle\frac{\mathrm{e}^{i(\omega_{mn}+\omega)(t-t_0)}-1}{\omega_{mn}+\omega}
\end{aligned} \tag{1.13}$$

where ω_{mn} is the energy difference between the final and initial states. The result is the sum of two terms, the first accounts for absorption, the second for stimulated emission. The second-order term can be treated in a similar way:

$$\begin{aligned}
\langle m|\hat{U}_{\mathrm{I}}^{(2)}(t,t_0)|n\rangle &= -\frac{1}{\hbar^2}\int_{t_0}^{t}\int_{t_0}^{t_1}\langle m|\hat{V}_{\mathrm{I}}(t_1)\hat{V}_{\mathrm{I}}(t_2)|n\rangle \,\mathrm{d}\,t_2\,\mathrm{d}\,t_1 = \\
&= -\frac{1}{\hbar^2}\sum_j\int_{t_0}^{t}\int_{t_0}^{t_1}\langle m|\hat{V}_{\mathrm{I}}(t_1)|j\rangle\langle j|\hat{V}_{\mathrm{I}}(t_2)|n\rangle \,\mathrm{d}\,t_2\,\mathrm{d}\,t_1
\end{aligned} \tag{1.14}$$

The closure relation ($\sum_j |j\rangle\langle j| = 1$) has been employed. As in the case of first-order phenomena, multiple terms arise from the development of this expression, which give rise to various non-linear phenomena, including Raman scattering. Without the need to develop each expression in its entirety, it is possible to infer the mechanism of the underlying phenomena from equation 1.14 which, in the case of Raman scattering, shows the concerted absorption and emission of a photon, both mediated by the electromagnetic radiation (via the operator $\hat{V}_{\mathrm{I}}$), through the manifold of states j, which are often called *virtual* states. The final state m can, in general, be any molecular state, but the most common observed type of transition is by far of vibrational nature.

1.3 The Transition Polarizability

In the previous section it was shown that, as a second order effect, an electromagnetic radiation of frequency ω may cause a molecular transition even when the energy of the radiation is very far removed from the corresponding energy. For example by employing a radiation in the visible region of the spectrum it is possible to cause a vibrational transition. Conservation of energy is guaranteed by the fact that the molecule will scatter light at a different frequency than that of the incoming beam, so if energy has been absorbed the scattered light will be of lower frequency.

Using a semi-classical picture in which the molecular system is treated using quantum mechanics while the radiation is described by means of the classical equation of electrodynamics, light scattering can be viewed as being caused by the fact that the molecular charge density (which can be described by its multipole moments), starts oscillating when it interacts with the electromagnetic radiation. To calculate the intensity of the scattered radiation we must first calculate the multipole moments of the molecular charge density, i.e. the transition multiple moments between the initial and final states. The wavefunction can be written as $\Psi = c_n\Psi_n + c_m\Psi_m$ and the corresponding expectation value for the electric dipole moment will include terms of the following type:

$$(\mu_a)_{mn} = \langle\Psi_m|\mu_a|\Psi_n\rangle + \langle\Psi_n|\mu_a|\Psi_m\rangle \tag{1.15}$$

The expressions for the wavefunctions can be found using time dependent perturbation theory.[10] Upon substitution into the previous equation (the mn subscript is dropped henceforth for clarity) and keeping only the first

order terms one obtains:

$$\begin{aligned}\mu_a^{(1)} &= \langle m|\mu_a|n^{(1)}\rangle\, \mathrm{e}^{i\omega_{mn}t} + \langle m^{(1)}|\mu_a|n\rangle\, \mathrm{e}^{i\omega_{mn}t} + \text{c.c.} = \\ &= \frac{1}{2\hbar}\sum_{j\neq n}\left(\frac{\langle m|\mu_a|j\rangle\langle j|\mu_b|n\rangle}{\omega_{jn}-\omega}\tilde{E}_b + \frac{\langle m|\mu_a|j\rangle\langle j|\mu_b|n\rangle}{\omega_{jn}+\omega}\tilde{E}_b^*\right)\mathrm{e}^{i\omega_{mn}t} + \\ &\quad + \frac{1}{2\hbar}\sum_{j\neq m}\left(\frac{\langle m|\mu_b|j\rangle\langle j|\mu_a|n\rangle}{\omega_{jm}-\omega}\tilde{E}_b^* + \frac{\langle m|\mu_b|j\rangle\langle j|\mu_a|n\rangle}{\omega_{jm}+\omega}\tilde{E}_b\right)\mathrm{e}^{i\omega_{mn}t} + \text{c.c.}\end{aligned} \tag{1.16}$$

where c.c. denotes the complex conjugate. There are two types of terms in this expression: the first and the fourth, which are proportional to $\tilde{E}_0\,\mathrm{e}^{-i(\omega-\omega_{mn})t}$, and the second and third, which are proportional to $\tilde{E}_0^*\,\mathrm{e}^{i(\omega+\omega_{mn})t}$. The terms of the first kind describe Raman scattering, in particular they will generate Stokes (conventional) Raman scattering if $\omega_m > \omega_n$ and anti-Stokes scattering if $\omega_m < \omega_n$. The terms of the second kind describe and induced emission of two quanta $\omega + \omega_{mn}$ and ω from an excited level n to a lower energy level m.[10] They will be neglected from here on.

The Raman transition dipole moment may then be rewritten as:

$$\mu_a^{(1)} = \frac{1}{2\hbar}\sum_{j\neq n,m}\left(\frac{\langle m|\mu_a|j\rangle\langle j|\mu_b|n\rangle}{\omega_{jn}-\omega} + \frac{\langle m|\mu_b|j\rangle\langle j|\mu_a|n\rangle}{\omega_{jm}+\omega}\right)\tilde{E}_b\,\mathrm{e}^{i\omega_{mn}t} + \text{c.c.} \tag{1.17}$$

Here the summation has been simplified by neglecting a term proportional to $\langle m|\mu_a|m\rangle - \langle n|\mu_a|n\rangle$ which should be small for vibrational Raman scattering.

The transition dipole may be rewritten in complex form to simplify notation:

$$\mu_a^{(1)} = \frac{\tilde{\alpha}_{ab}\tilde{E}_b\,\mathrm{e}^{i\omega_{mn}} + \text{c.c.}}{2} = \mathrm{Re}\,\tilde{\mu}_a \tag{1.18}$$

where the transition dynamic polarizability is thus defined:

$$\tilde{\alpha}_{ab} = \frac{1}{\hbar}\sum_{j\neq n,m}\left(\frac{\langle m|\mu_a|j\rangle\langle j|\mu_b|n\rangle}{\omega_{jn}-\omega} + \frac{\langle m|\mu_b|j\rangle\langle j|\mu_a|n\rangle}{\omega_{jm}+\omega}\right) \tag{1.19}$$

This is the sum-over-states expression for the (nonresonant) polarizability

and is the quantity that must be calculated in order to simulate Raman spectra. The transition polarizability reduces to the complex dynamic polarizability when $m = n$, which is symmetric in the sense that $\tilde{\alpha}^*_{ab} = \tilde{\alpha}_{ba}$ (it is actually Hermitian). The transition version of the polarizability in general possesses no such symmetry. Like any other tensor however, it may be separated into a symmetric and an antisymmetric part, which are easily found:

$$\tilde{\alpha}_{ab} = \tilde{\alpha}^{\mathrm{s}}_{ab} + \tilde{\alpha}^{\mathrm{a}}_{ab} \qquad ; \qquad \tilde{\alpha}^{\mathrm{s}}_{ab} = \frac{\tilde{\alpha}_{ab} + \tilde{\alpha}_{ba}}{2} \quad \wedge \quad \tilde{\alpha}^{\mathrm{a}}_{ab} = \frac{\tilde{\alpha}_{ab} - \tilde{\alpha}_{ba}}{2} \tag{1.20}$$

and each of these polarizabilities may be separated into its real and imaginary parts:

$$\tilde{\alpha}^{\mathrm{s}}_{ab} = \alpha^{\mathrm{s}}_{ab} - i\alpha'^{\mathrm{s}}_{ab} \qquad ; \qquad \tilde{\alpha}^{\mathrm{a}}_{ab} = \alpha^{\mathrm{a}}_{ab} - i\alpha'^{\mathrm{a}}_{ab} \tag{1.21}$$

The expressions for these quantities are:

$$\begin{aligned}
\alpha^{\mathrm{s}}_{ab} =& \frac{1}{2\hbar} \sum_{j \neq n,m} \frac{\omega_{jn} + \omega_{jm}}{(\omega_{jn} - \omega)(\omega_{jm} + \omega)} \mathrm{Re}(\langle m|\mu_a|j\rangle\langle j|\mu_b|n\rangle + \langle m|\mu_b|j\rangle\langle j|\mu_a|n\rangle) \\
\alpha^{\mathrm{a}}_{ab} =& \frac{1}{2\hbar} \sum_{j \neq n,m} \frac{2\omega - \omega_{mn}}{(\omega_{jn} - \omega)(\omega_{jm} + \omega)} \mathrm{Re}(\langle m|\mu_a|j\rangle\langle j|\mu_b|n\rangle - \langle m|\mu_b|j\rangle\langle j|\mu_a|n\rangle) \\
\alpha'^{\mathrm{s}}_{ab} =& -\frac{1}{2\hbar} \sum_{j \neq n,m} \frac{\omega_{jn} + \omega_{jm}}{(\omega_{jn} - \omega)(\omega_{jm} + \omega)} \mathrm{Im}(\langle m|\mu_a|j\rangle\langle j|\mu_b|n\rangle + \langle m|\mu_b|j\rangle\langle j|\mu_a|n\rangle) \\
\alpha'^{\mathrm{a}}_{ab} =& -\frac{1}{2\hbar} \sum_{j \neq n,m} \frac{2\omega - \omega_{mn}}{(\omega_{jn} - \omega)(\omega_{jm} + \omega)} \mathrm{Im}(\langle m|\mu_a|j\rangle\langle j|\mu_b|n\rangle - \langle m|\mu_b|j\rangle\langle j|\mu_a|n\rangle)
\end{aligned} \tag{1.22}$$

If $m = n$ then clearly $\tilde{\alpha}^{\mathrm{a}}_{ab} = 0$ so antisymmetric Rayleigh scattering is only possible for degenerate states, so that $m \neq n$ while $\omega_{mn} = 0$. These four tensors diverge if there is a state j for which $\omega_{jn} \approx \omega$ or $\omega_{mj} \approx \omega$, i.e. if the incident radiation is resonant.

To remove the singularity and accommodate resonance phenomena one only needs to empirically include the finite lifetime of the excited states into the picture. This can be accomplished by means of the substitution

$\omega_j \to \omega_j - i\gamma_j$, where $2\gamma_j$ is the damping constant of the state j, and is zero for the ground state. The Raman transition polarizability then becomes:

$$\tilde{\alpha}_{ab} = \frac{1}{\hbar} \sum_{j \neq n,m} \left(\frac{\langle m|\mu_a|j\rangle\langle j|\mu_b|n\rangle}{\omega_{jn} - \omega - i\gamma_{jn}} + \frac{\langle m|\mu_b|j\rangle\langle j|\mu_a|n\rangle}{\omega_{jm} + \omega + i\gamma_{jm}} \right) \tag{1.23}$$

The sign of the damping factor in the second term is justified by the fact that it results from a complex conjugate. This expression is the most general form of the Raman transition polarizability and it can be used to describe a wide array of different phenomena.

1.4 Simplification of the Raman polarizability

The summation in equation 1.23 runs, in principle, over all possible energy eigenstates of the isolated molecule however, in order to apply the formula in practical computations, the expression must first be simplified through the separation of the different degrees of freedom of the system. Translational motion is always separable from the other molecular motions. This is not the case for rotations, vibrations, and electronic degrees of freedom. However, if one assumes both the Born-Oppenheimer and the rigid rotor approximations, the wavefunction may be written as a direct product and the corresponding energy is just the sum of the energies corresponding to the different degrees of freedom:

$$|j\rangle = |e_j v_j r_j\rangle = |e_j\rangle|v_j\rangle|r_j\rangle \qquad ; \qquad \omega_j = \omega_{e_j} + \omega_{v_j} + \omega_{r_j} \tag{1.24}$$

The Raman transition polarizability (1.23) then may be written as:

$$\tilde{\alpha}_{ab} = \langle r_m v_m e_m|\hat{\alpha}_{ab}|e_n v_n r_n\rangle \tag{1.25}$$

where the polarizability now takes the form of an operator:

$$\hat{\alpha}_{ab} = \frac{1}{\hbar} \sum_{j \neq n,m} \left(\frac{\mu_a |e_j v_j r_j\rangle\langle r_j v_j e_j| \mu_b}{\omega_{jn} - \omega - i\gamma_{jn}} + \frac{\mu_b |e_j v_j r_j\rangle\langle r_j v_j e_j| \mu_a}{\omega_{jm} + \omega + i\gamma_{jm}} \right) \tag{1.26}$$

This expression can, and must, be simplified. The only variable quantities that enter the formula are the initial state n, the final state m, and the angular frequency of the incoming radiation ω. Some assumptions may be made right away. If the temperature is not too high the system will initially be in the electronic and vibrational ground states, which will also be assumed to be nondegenerate. When Raman experiments are performed the radiation frequency is chosen by the experimentalist, and usually lies in the visible portion of the spectrum. This means that the radiation may lie well below any electronic transition frequency, which implies that the final state m will be in general an excited rotovibrational state lying on the ground electronic Potential Energy Surface (PES), and this is what happens in conventional Raman scattering. If, however, the incident radiation is close to or even higher than an electronic transition frequency of the molecule, then near resonance and resonance Raman scattering will take place. These arguments suggest that further simplification requires distinction between different cases.

The first thing that can be done is the removal of the rotational states from the summation. First we look at the numerators: as a general rule the transition dipole moment of two rotational or vibrational states with very different quantum numbers will be small. This is reflected in the selection rules for rotational and vibrational spectroscopy which only allow transitions where the quantum number varies by ± 1. Now we look at the denominators: since ω is in the visible range of the spectrum $\omega_{r_j r_n}$ and $\omega_{r_j r_m}$ will be negligible, unless ω is resonant with some vibronic transition, but even then the damping terms will dominate the denominator for they are of the order of at least tens of wavenumbers. The damping terms themselves will also not depend upon the rotational state since rotational excited states are long living. Therefore the closure relation $\sum_j |r_j\rangle\langle r_j| =$

1 implies that the polarizability operator may be written as:

$$\hat{\alpha}_{ab} = \frac{1}{\hbar} \sum_{j \neq n,m} \left(\frac{\mu_a |e_j v_j\rangle \langle v_j e_j| \mu_b}{\omega_{jn} - \omega - i\gamma_{jn}} + \frac{\mu_b |e_j v_j\rangle \langle v_j e_j| \mu_a}{\omega_{jm} + \omega + i\gamma_{jm}} \right) \tag{1.27}$$

and then this tensor must be integrated over the rotational coordinates obtaining:

$$(\tilde{\alpha}_{ab})_{mn} = \langle r_m | \tilde{\alpha}_{ab} | r_n \rangle = \tilde{\alpha}_{\alpha\beta} \langle r_m | l_{\alpha a} l_{\beta b} | r_n \rangle \tag{1.28}$$

where $l_{\alpha a}$ and $l_{\beta b}$ are the direction cosines of the space-fixed with respect to the molecule-fixed frames of reference. To further simplify this expression additional approximations must be made.

1.5 Vibrational Raman scattering

There are four cases that must be distinguished: whether the incident frequency is resonant or not, and whether the final electronic state is the same as the initial electronic state. In vibrational resonance Raman, as opposed to vibronic Raman scattering, $e_m = e_n$ so the latter assumption is satisfied. If we assume the incident frequency to be non-resonant, then we can remove all virtual vibrational states from sum-over-states expression, similarly to what was done in the case of rotations. We can also safely assume to be in the ground electronic state. In this case the polarizability is simply given by $\langle v_m | \hat{\alpha}^{\mathrm{el}} | v_n \rangle$, where $\hat{\alpha}^{\mathrm{el}}$ is the pure electronic polarizability, written as a sum over all electronic degrees of freedom:

$$\hat{\alpha}^{\mathrm{el}}_{\alpha\beta} = \frac{1}{\hbar} \sum_{j \neq 0} \left(\frac{\langle e_0 | \mu_\alpha | e_j \rangle \langle e_j | \mu_\beta | e_0 \rangle}{\omega_{j0} - \omega} + \frac{\langle e_0 | \mu_\beta | e_j \rangle \langle e_j | \mu_\alpha | e_0 \rangle}{\omega_{j0} + \omega} \right) \tag{1.29}$$

The quantities that appear in this expression are the familiar vertical excitation energies (ω_{j0}) and electronic transition dipole moments. While this sum-over-states expression is of great interest from a purely theoretical point of view, it is computationally to expensive to use it directly because of the very large number number of states needed to achieve convergence. The calculation of the purely electronic polarizability (and its derivatives)

can be alternatively be achieved by means of linear response theory.[11]

Computing the derivatives of the electronic polarizability is crucial because we still need to find its matrix element between the initial and final *vibrational* states. A simple way to do this is to express the geometrical dependence of the polarizability tensor using a Taylor expansion with respect to the normal modes of vibration:

$$\langle v_m|\hat{\alpha}^{\mathrm{el}}|v_n\rangle = \tilde{\alpha}^{\mathrm{el}}_{\alpha\beta}(0)\langle v_m|v_n\rangle + \sum_a \left(\frac{\partial\tilde{\alpha}^{\mathrm{el}}_{\alpha\beta}}{\partial Q_a}\right)_0 \langle v_m|Q_a|v_n\rangle + \ldots \qquad (1.30)$$

In vibrational Raman scattering $v_m \neq v_m$ so the zero order term does not contribute, therefore for a transition to be allowed there must be a change in the polarizability along the normal modes. In the harmonic approximation one obtains that the only one normal mode can be excited at a time with $v_m = v_m \pm 1$.

1.6 Vibrational resonance Raman scattering

If the incident frequency is close to an electronic transition of the molecule, then the damping factors in the denominators of the transition polarizability cannot be neglected. As a consequence, the closure over the vibrational states is not possible, however different simplifications may be done. If the incoming frequency is close to a electronic transition energy then the corresponding denominator will be very small, and the pertinent electronic state will dominate the sum over states, therefore the contributions from all other electronic states may be disregarded, unless they, too, are very close in energy. In addition, of the two terms that make up the polarizability, only the one with the resonant denominator will be significant (the first one, in the case of Stokes scattering). The dipole moment operators may be integrated over the electronic degrees of freedom ($\mu^{0j} = \langle e_0|\mu|e_j\rangle$), and expanded in a Taylor series around the equilibrium geometry similarly to what was done for the electronic polarizability. We are left with the

following expression:

$$\begin{aligned}\tilde{\alpha}_{\alpha\beta} =& \frac{1}{\hbar}\mu_{\alpha}^{0j}(0)\mu_{\beta}^{j0}(0)\sum_{v_j'}\frac{\langle v_m|v_j'\rangle\langle v_j'|v_n\rangle}{\omega_{jn}-\omega-i\gamma_j}+ \\ &+\frac{1}{\hbar}\sum_{v_j'}\sum_{a}\left(\frac{\partial\mu_{\alpha}^{0j}}{\partial Q_a}\mu_{\beta}^{j0}(0)\frac{\langle v_m|Q_a|v_j'\rangle\langle v_j'|v_n\rangle}{\omega_{jn}-\omega-i\gamma_j}+\right. \\ &\left.+\mu_{\alpha}^{0j}(0)\frac{\partial\mu_{\beta}^{j0}}{\partial Q_a}\frac{\langle v_m|v_j'\rangle\langle v_j'|Q_a|v_n\rangle}{\omega_{jn}-\omega-i\gamma_j}\right)+\ldots\Bigg)\end{aligned} \tag{1.31}$$

In these equations the "prime" indicates that the corresponding vibrational state belongs to the excited electronic PES, furthermore $\omega_{jn} = \omega_{e_j e_0} + \omega_{v_j' v_n}$ and the same goes for the damping term. In the case of resonance Raman scattering there are no selection rules available other than those arising from the symmetry of the vibrational states. For a given incident frequency those excited states that are closer to the resonance condition will contribute more to the summation because of the smaller denominator. For larger molecules there is a very high density of vibrational states though, which complicates things.

It is useful to derive a time dependent analog of the previous equations that allows for a different approach for the calculation of the RR intensity, starting with the resonant polarizability:

$$\tilde{\alpha}_{\alpha\beta} = \frac{1}{\hbar}\sum_{v_j'}\frac{\langle v_m|\mu_{\alpha}^{0j}|v_j'\rangle\langle v_j'|\mu_{\beta}^{j0}|v_n\rangle}{\omega_{jn}-\omega-i\gamma_j} \tag{1.32}$$

The frequency dependent denominator may be expressed via its half Fourier transform:

$$\tilde{\alpha}_{\alpha\beta} = \frac{i}{\hbar}\sum_{v_j'}\langle v_m|\mu_{\alpha}^{0j}|v_j'\rangle\langle v_j'|\mu_{\beta}^{j0}|v_n\rangle\int_0^{\infty}\mathrm{e}^{-i(\omega_{jn}-\omega-i\gamma_j)t}\,\mathrm{d}\,t \tag{1.33}$$

It is possible to get rid of the summation over the excited nuclear eigen-

states by considering the following relations:

$$\langle v'_j|\,\mathrm{e}^{-i\omega_j t} = \langle v'_j|\,\mathrm{e}^{-i(\omega_{e_j}+\omega_{v'_j})t} = \langle v'_j|\,\mathrm{e}^{-i\hat{H}_j t/\hbar} \tag{1.34}$$

The exponent now contains the nuclear Hamiltonian corresponding to the excited electronic state e_j defined by $\hat{H}_j = \hat{T}_\mathrm{N} + U_j(Q)$ which does not depend upon the vibrational quantum numbers v'_j and the closure relation may be employed, yielding:

$$\tilde{\alpha}_{\alpha\beta} = \frac{i}{\hbar}\int_0^\infty \langle v_m|\mu_\alpha^{0j}\,\mathrm{e}^{-i\hat{H}_j t/\hbar}\,\mu_\beta^{j0}|v_n\rangle\,\mathrm{e}^{i(\omega_n+\omega)t-\gamma_j t}\,\mathrm{d}\,t \tag{1.35}$$

By retaining only the Frank-Condon terms of the expansion of the electric dipole the expression is further simplified:

$$\tilde{\alpha}_{\alpha\beta} = \frac{i}{\hbar}\mu_\alpha^{0j}(0)\mu_\beta^{j0}(0)\int_0^\infty \langle v_m|\,\mathrm{e}^{-i\hat{H}_j t/\hbar}\,|v_n\rangle\,\mathrm{e}^{i(\omega_n+\omega)t-\gamma_j t}\,\mathrm{d}\,t \tag{1.36}$$

This means that the RR spectrum can be viewed as being determined by the time evolution of the initial vibrational wavepacket $|v_n\rangle$ on the excited state PES.

1.7 The experimentally measured quantity

As the molecular charge density oscillates, it emits an electromagnetic radiation in all directions. In the preceding sections we have shown that the induced molecular dipole moment $\tilde{\mu}$ oscillating with a frequency ω_s is related to the incident field $\tilde{E}^\mathrm{i}$ via the formula $\tilde{\mu}_a = \alpha_{ab}\tilde{E}^\mathrm{i}_b$. We must now find the intensity of the light generated by this dipole. The electric field at a point $\vec{R} = R\vec{n}$ can be shown to be:[10]

$$\begin{aligned}\tilde{E}^\mathrm{s}_a &= \frac{\omega_\mathrm{s}^2}{c^2}\frac{\mathrm{e}^{i\omega_\mathrm{s}(\frac{R}{c}-t)}}{R}(\tilde{\mu}_a - n_a n_b\tilde{\mu}_b) = \\ &= \frac{\omega_\mathrm{s}^2}{c^2}\frac{\mathrm{e}^{i\omega_\mathrm{s}(\frac{R}{c}-t)}}{R}(\tilde{\alpha}_{ac} - n_a n_b\tilde{\alpha}_{bc})\tilde{E}^\mathrm{i}_c\end{aligned} \tag{1.37}$$

Where the summation over repeated indices is implied, and $\vec{n}$ is the direction of propagation of the scattered light. The presence of the term $n_a n_b \tilde{\mu}_b$ ensures that the field $\tilde{E}^{\mathrm{s}}$ is perpendicular to the direction of propagation. The intensity of the scattered radiation is given by $\tilde{E}^{\mathrm{s}}\tilde{E}^{\mathrm{s}*}/4\pi$, which reduces to:

$$I_{\mathrm{s}} = \frac{1}{R^2}\frac{\omega_{\mathrm{s}}^4}{c^4}(\tilde{\alpha}_{ac} - n_a n_b \tilde{\alpha}_{bc})(\tilde{\alpha}^*_{ad} - n_a n_e \tilde{\alpha}^*_{ed})\frac{\tilde{E}^{\mathrm{i}}_c \tilde{E}^{\mathrm{i}*}_d}{4\pi} \tag{1.38}$$

At this point it is necessary to consider the particular experimental conditions one aims to reproduce. In particular, both the incident and the scattered radiation may or may not be polarized, and the angle between the two radiations must also be specified. A common experimental configuration involves scattering at a $\pi/2$ angle, with an incident radiation that is perpendicular to the plane described by the two light rays ($\perp^{\mathrm{i}}$), an unpolarized scattered radiation ($\|^{\mathrm{s}} + \perp^{\mathrm{s}}$). Let us assume that the incident radiation travels along the Y direction, and is polarized along the Z axis, while the scattered radiation travels along the X axis. The above expression becomes:

$$\begin{aligned} I_{\mathrm{s}}(\pi/2, \|^{\mathrm{s}} + \perp^{\mathrm{s}}, \perp^{\mathrm{i}}) =& \frac{1}{R^2}\frac{\omega_{\mathrm{s}}^4}{c^4}(\tilde{\alpha}_{aZ} - \delta_{aX}\tilde{\alpha}_{XZ})(\tilde{\alpha}^*_{aZ} - \delta_{aX}\tilde{\alpha}^*_{XZ})\frac{\tilde{E}^{\mathrm{i}}_Z \tilde{E}^{\mathrm{i}*}_Z}{4\pi} \\ =& \frac{1}{R^2}\frac{\omega_{\mathrm{s}}^4}{c^4}(\tilde{\alpha}_{YZ}\tilde{\alpha}^*_{YZ} + \tilde{\alpha}_{ZZ}\tilde{\alpha}^*_{ZZ})\frac{\tilde{E}^{\mathrm{i}}_Z \tilde{E}^{\mathrm{i}*}_Z}{4\pi} \end{aligned} \tag{1.39}$$

Raman intensity is usually reported in terms of the scattering cross-section σ', which can be defined as the ratio of the scattered intensity through a surface $R^2\,\mathrm{d}\,\Omega$ (where $\mathrm{d}\,\Omega$ denotes a solid angle) to the incident one (given by $\tilde{E}^{\mathrm{i}}\tilde{E}^{\mathrm{i}*}/4\pi$), which is simply:

$$\sigma'(\pi/2, \|^{\mathrm{s}} + \perp^{\mathrm{s}}, \perp^{\mathrm{i}}) = \frac{\omega_{\mathrm{s}}^4}{c^4}(\tilde{\alpha}_{YZ}\tilde{\alpha}^*_{YZ} + \tilde{\alpha}_{ZZ}\tilde{\alpha}^*_{ZZ}) \tag{1.40}$$

Now we must realize that this expression has been written in the laboratory reference frame, and if the sample is isotropic we must average this result over all possible molecular orientations. The molecular polarizabil-

ity expressed in the laboratory reference frame can be related to the one computed in the molecule reference frame through a linear transformation $\alpha_{ab} = l_{a\alpha} l_{b\beta} \alpha_{\alpha\beta}$, where the coefficients l are commonly called direction cosines.[12] Performing an orientational average then just requires the calculation of an integral of a product of direction cosines. If we denote the orientational average using a braket notation, we have $\langle \alpha_{ab} \rangle = \alpha_{\alpha\beta} \langle l_{a\alpha} l_{b\beta} \rangle$. For the calculation of the Raman cross-section we require the average of products of four direction cosines. The required integrals are:[12]

$$\langle l_{Z\alpha} l_{Z\beta} l_{Z\gamma} l_{Z\delta} \rangle = \frac{1}{15} (\delta_{\alpha\beta}\delta_{\gamma\delta} + \delta_{\alpha\gamma}\delta_{\beta\delta} + \delta_{\alpha\delta}\delta_{\beta\gamma}) \tag{1.41}$$

$$\langle l_{Y\alpha} l_{Z\beta} l_{Y\gamma} l_{Z\delta} \rangle = \frac{1}{30} (-\delta_{\alpha\beta}\delta_{\gamma\delta} + 4\delta_{\alpha\gamma}\delta_{\beta\delta} - \delta_{\alpha\delta}\delta_{\beta\gamma}) \tag{1.42}$$

These expressions can be used to rewrite the previous equation in terms of the molecular polarizability in the molecule reference frame. After some manipulation, we obtain the following expression for the Raman cross-section:

$$\sigma'(\pi/2, \|^{\mathrm{s}} + \perp^{\mathrm{s}}, \perp^{\mathrm{i}}) = \frac{\omega_{\mathrm{s}}^4}{c^4} \frac{45a^2 + 7g^2 + 5d^2}{45} \tag{1.43}$$

$$a^2 = \frac{1}{9} \operatorname{Re} \alpha^{\mathrm{s}*}_{\alpha\alpha} \alpha^{\mathrm{s}}_{\beta\beta} \qquad g^2 = \frac{1}{2} \operatorname{Re} (3\alpha^{\mathrm{s}*}_{\alpha\beta} \alpha^{\mathrm{s}}_{\alpha\beta} - \alpha^{\mathrm{s}*}_{\alpha\alpha} \alpha^{\mathrm{s}}_{\beta\beta}) \qquad d^2 = \frac{3}{2} \operatorname{Re} \alpha^{\mathrm{a}*}_{\alpha\beta} \alpha^{\mathrm{a}}_{\alpha\beta} \tag{1.44}$$

where we have introduced the mean polarizability a^2, the symmetric anisotropy g^2, and the antisymmetric anisotropy d^2,[13] in terms of the symmetric and antisymmetric components of the polarizability tensor, α^{s} and α^{a}.

Chapter 2

Molecular Vibrations

In this chapter we shall briefly review the theoretical foundations of the perturbational treatement of the anharmonic vibrational wavefunction, which will be used to include the harmonic and anharmonic vibrational effects in the calculation of Raman spectra, as well as other spectroscopic properties.

2.1 The Quantum Harmonic Oscillator

2.1.1 The one-dimensional case

Before we dive into the theoretical treatement of the anharmonic oscillator, it is first useful to retrace the steps involved in the treatement of its harmonic counterpart, both for completeness and to establish and better define the notation used throughout the chapter.

In the one-dimensional case, which is easily extended to three dimensions, the quantum analog of the harmonic oscillator is described by the following Hamiltonian:

$$\hat{H} = \frac{1}{2m}p_x^2 + \frac{1}{2}kx^2 = \frac{1}{2m}p_x^2 + \frac{1}{2}\omega^2 m x^2 \quad ; \quad \omega^2 = \frac{k}{m} \tag{2.1}$$

where, in the case of molecular systems, x and p_x may be regarded as a normal coordinate (in unit of length) and its conjugate momentum,

while m is the corresponding reduced mass and k is the force constant. Rewriting it in mass weighted normal coordinates defined as $Q = \sqrt{m}x$ and $P = p_x/\sqrt{m}$ one has:

$$\hat{H} = \frac{1}{2}P^2 + \frac{1}{2}\omega^2 Q^2 \tag{2.2}$$

It is useful to define yet another set of normal coordinates (q, p) that are adimensional, and carry all pesky constants within them:

$$Q = \sqrt{\frac{\hbar}{\omega}}q \quad ; \quad P = \sqrt{\hbar\omega}\, p \quad \Longrightarrow \quad [q, p] = i \tag{2.3}$$

The Hamiltonian can then be rewritten in this new system of coordinates as:

$$\hat{H} = \frac{1}{2}\hbar\omega(q^2 + p^2) = \frac{1}{2}\hbar\omega(q - ip)(q + ip) - \frac{1}{2}\hbar\omega i[q, p] = \hbar\omega\left(\frac{1}{2} + a^\dagger a\right) \tag{2.4}$$

where we have defined the creation and annihilation operators:

$$a = \frac{q + ip}{\sqrt{2}} \quad ; \quad a^\dagger = \frac{q - ip}{\sqrt{2}} \quad \Longrightarrow \quad [a, a^\dagger] = 1 \tag{2.5}$$

Clearly the creation operator is the adjoint of the annihilation operator and vice-versa. The two operators do not commute with the Hamiltonian, in fact it is easy to see that $[H, a] = -\hbar\omega a$ and $[H, a^\dagger] = \hbar\omega a^\dagger$.

From the commutation properties just defined it is possible to calculate eigenvalues and eigenstates of the Hamiltonian operator. We start by noting that the energy cannot be negative because the Hamiltonian is a sum of squares of self-adjoint operators (so for example $\langle v|p^2|v\rangle = \langle v|p^\dagger p|v\rangle \geq 0 \quad \forall\, |v\rangle$ because the scalar product is positive definite). The names "creation" and "annihilation" given to the operators stem from the fact that they can add or subtract a quantum of energy from an energy eigenstate.

If we take a generic energy eigenstate $|v\rangle$ such that $H|v\rangle = E_v|v\rangle$ we have:

$$\begin{aligned} Ha|v\rangle &= ([H,a] + aH)|v\rangle = (E_v - \hbar\omega)a|v\rangle \\ Ha^\dagger|v\rangle &= ([H,a^\dagger] + a^\dagger H)|v\rangle = (E_v + \hbar\omega)a^\dagger|v\rangle \end{aligned} \tag{2.6}$$

which means that if $|v\rangle$ is an energy eigenstate so are $a|v\rangle$ and $a^\dagger|v\rangle$ but the corresponding energy is respectively decreased or increased by $\hbar\omega$. By repeatedly applying the annihilation operator on an energy eigenstate it would be possible to lower the energy to negative values, unless at some point we find $a|v\rangle = 0$. Hence the lowest energy state is obtained by setting $a|0\rangle = 0|0\rangle$ which means:

$$\langle 0|a^\dagger a|0\rangle = \langle 0|\frac{H}{\hbar\omega} - \frac{1}{2}|0\rangle = \frac{E_0}{\hbar\omega} - \frac{1}{2} = 0 \quad \Longrightarrow \quad E_0 = \frac{1}{2}\hbar\omega \tag{2.7}$$

All other eigenstates with their energies can be found by applying the creation operator onto the ground state the desired number of times (there is in principle no upper bound for the energy):

$$E_v = \left(\frac{1}{2} + v\right)\hbar\omega \quad ; \quad |v\rangle = N_v a^{\dagger v}|0\rangle \tag{2.8}$$

Where N_v is a normalization constant which depends on the vibrational quantum number v. By employing the commutation relation it can be shown by induction that:

$$a|v\rangle = \sqrt{v}|v-1\rangle \quad ; \quad a^\dagger|v\rangle = \sqrt{v+1}|v+1\rangle \quad \Longrightarrow \quad |v\rangle = \frac{1}{\sqrt{v!}}a^{\dagger v}|0\rangle \tag{2.9}$$

The wavefunction corresponding to the ground and excited states can be found by switching to the Schrödinger representation. The ground state can be found from the identity $a|\Psi_0\rangle = 0$:

$$(q + ip)|\Psi_0\rangle = \left(q + \frac{\partial}{\partial q}\right)\Psi_0(q) = 0 \quad \Longrightarrow \quad \Psi_0'(q) = -q\Psi_0(q) \tag{2.10}$$

$$\Psi_0(q) = N_0\, \mathrm{e}^{-q^2/2} \tag{2.11}$$

Once normalized, the wavefunction for the ground state can be written as a function of the various variables previously defined:

$$\Psi_0 = \frac{1}{\pi^{1/4}} \mathrm{e}^{-q^2/2} = \left(\frac{m\omega}{\pi\hbar}\right)^{1/4} \mathrm{e}^{-\frac{m\omega}{2\hbar}x^2} = \left(\frac{\omega}{\pi\hbar}\right)^{1/4} \mathrm{e}^{-\frac{\omega}{2\hbar}Q^2} \tag{2.12}$$

The excited states wavefunction can then be obtained using the previously found formulas involving the creation operator written in the Schrödinger representation. The eigenstates of the harmonic oscillator possess many interesting properties, however the most useful for us is probably the simple expressions that arise when a position operator q acts on a vibrational state:

$$q|v\rangle = \sqrt{\frac{v+1}{2}}|v+1\rangle + \sqrt{\frac{v}{2}}|v\rangle \tag{2.13}$$

$$q^2|v\rangle = \frac{\sqrt{(v+2)(v+1)}}{2}|v+2\rangle + \frac{2v+1}{2}|v\rangle + \frac{v(v-1)}{2}|v-1\rangle \tag{2.14}$$

These expressions can be used to greatly simplify the formulas obtained in the perturbative treatement of anharmonicity and in other areas such as in the computation of Franck-Condon factors in vibronic and resonance Raman spectroscopy.[14–16]

2.1.2 Vibrational frquencies of molecular systems

The application of the former treatement to the calculation of the vibrational frequencies of a molecular system is not actually straightforward because of two main problems. First, the expression of the Born-Oppenheimer vibrational Hamiltonian, written in cartesian coordinates, includes both translational and rotational contributions. While the former can be exactly removed by placing the origin of the reference frame in the nuclear center of mass, the latter require the additional assumption that the kinetic coupling between the vibrational and rotational motions be weak. Second, the cartesian coordinates are coupled by the force constants, therefore a new set of coordinates must be defined to separate the Hamiltonian. In the following we shall assume that the considered sys-

tems are non-linear, therefore if the molecule is composed of N atoms, the number of vibrational modes is $N_{\text{vib}} = 3N - 6$.

In cartesian coordinates R the nuclear Hamiltonian of a molecule can be written as:

$$\hat{H}_{\text{nuc}} = \sum_{\alpha} \frac{p_\alpha^2}{2M_\alpha} + U(R) = \sum_{\alpha} \frac{p_\alpha^2}{2M_\alpha} + \frac{1}{2} \sum_{\alpha\beta} U''_{\alpha\beta} R_\alpha R_\beta + O(R^3) \quad (2.15)$$

where the summation runs over all atomic coordinates, $U(R)$ is the potential energy surface, and the matrix $\mathbf{U}''$ contains the force constants in cartesian coordinates. The Taylor expansion of the energy is centered around the equilibrium geometry, in which the first order term (i.e. the forces acting on the atoms) is zero. Similarly to the one-dimensional case, the atom masses are combined with the cartesian coordinates, and the Hamiltonian is first rewritten in terms of a new set of coordinates defined by $\mathbf{M}^{1/2}\mathbf{R}$, where $\mathbf{M}$ is the diagonal matrix containing the atom masses. In the new system the force constant matrix becomes $\mathbf{M}^{-1/2}\mathbf{U}''\mathbf{M}^{-1/2}$, which can be diagonalized:

$$\mathbf{F} = \mathbf{M}^{-1/2}\mathbf{U}''\mathbf{M}^{-1/2} = \mathbf{L}^\dagger \mathbf{\Omega}^2 \mathbf{L} \quad (2.16)$$

Six eigenvalues are expected to be null since they correspond to the tranlsational and rotational motions, which can alternatively be projected out before the diagonalization is performed. The remaining N_{vib} eigenvectors of $\mathbf{L}$ are used to define the normal modes $\mathbf{Q} = \mathbf{L}^\dagger \mathbf{M}^{1/2}\mathbf{R}$, while the corresponding eigenvalues are the square of the harmonic vibrational frequencies of the molecule, collected within the diagonal matrix $\mathbf{\Omega}$. A system of adimensional normal coordinates can also be defined by $\mathbf{q} = \mathbf{\Omega}^{1/2}\mathbf{Q}/\sqrt{\hbar}$.

2.2 Second Order Vibrational Perturbation Theory

The harmonic approximation is not sufficient if an accurate description of a molecule's vibrations is required. One of the methods that can be employed to introduce the effects of anharmonicity employs time-independent perturbation theory, where the zero-order (unperturbed) Hamiltonian is harmonic, and all anharmonic contributions are assigned to a first or second order perturbation, leading to second order vibrational perturbation theory (VPT2). The third and fourth order terms in the Taylor expansion of the electronic energy are thus recovered, and a kinetic energy term, accounting for the coupling of rotations and vibrations, is also included:[17–19]

$$\begin{aligned}\hat{H} &= \hat{H}_0 + \hat{H}_1 + \hat{H}_2 = \\ &= \frac{\hbar}{2}\sum_a \omega_a(q_a^2 + p_a^2) + \frac{1}{6}\sum_{abc} k_{abc} q_a q_b q_c + \\ &\quad + \frac{1}{24}\sum_{abcd} k_{abcd} q_a q_b q_c q_d + \sum_{\alpha=x,y,z} B_\alpha^e \sum_{abcd} \zeta_{ab}^\alpha \zeta_{cd}^\alpha q_a p_b q_c p_d\end{aligned} \tag{2.17}$$

where the cubic and quartic constants k are the third and fourth derivatives of the electronic energy with respect to the adimentional normal modes, and B^e and ζ denote the equilibrium rotational constant and the Coriolis coupling constants, respectively. The last term is included in $\hat{H}_2$ along with the quartic derivatives. It should be noted that the perturbation expansion has to include second-order terms, since a cubic potential would be unbounded, therefore its exact ground state would have a divergent energy.

The equations of perturbation theory typically involve infinite sum-over-states formulas, however the properties of the harmonic oscillator greately simplify the expressions. For instance, the first-order correction

to the state $|v\rangle$ is defined as:

$$|v^{(1)}\rangle = -\frac{1}{\hbar}\sum_{w\neq v}|w\rangle\frac{\langle w|\frac{1}{6}\sum_{abc}k_{abc}q_aq_bq_c|v\rangle}{\omega_w-\omega_v} \tag{2.18}$$

In principle the summation runs over all other vibrational states, however the numerator in the expression is only nonzero for states that differ from $|v\rangle$ for up to three quanta.

The well-known formulas of perturbation theory can then be applied as long as there are no degenerate states, which require a separate treatment, as can be seen from the denominator of the former expression, which becomes singular if $\omega_w \approx \omega_v$. In particular, the development of the numerators in the perturbation expansions shows that the resonances that can appear are of the type $\omega_a \approx \omega_b + \omega_c$ or $\omega_a = 2\omega_b$. Degenerate vibrational states always occur in the case of linear, symmetric top, and spherical top molecules, whose symmetry point groups possess irreducible representations with dimension greater than one. Therefore, in the following we restrict the treatment to asymmetric top molecules. Accidental degeneracy, however, may also be present regardless of symmetry, leading to resonances in the perturbation expressions. This is a major problem in VPT2 since it severely affects the ability to extend the method to large systems because, while the number of vibrational modes is proportional to the number of atoms, the spectral region where the energies of these modes lie remains the same, therefore the density of states increases with system size, so the larger the system the more likely it is to be affected by resonances.

The simplest way to treat resonances is to identify the offending terms by comparing the denominators in the perturbative expansions with an arbitrarily chosen threshold and simply removing them, a method known as Deperturbed VPT2 (DVPT2). To improve accuracy however, the resonant terms can be reintroduced by treating them variationally in the subspace of the near-degenerate states leading to the Generalized VPT2 (GVPT2).[20–22] This method can yield very accurate results, however the

identification of the resonant terms remains arbitrary and can lead to numerical problems and discontinuities if a particular term is very close to the threshold and, if the same system is treated using two different methods, can be classified as resonant or not. To overcome this limitation other methods have been proposed, such as the Degeneracy Corrected VPT2 (DCPT2)[23,24] and, more recently, the Hybrid DCPT2 (HDCPT2),[25] which overcomes some of the limitations still present in DCPT2.

In DCPT2 all potentially resonant terms are rewritten in the general form $k^2/2\varepsilon$, where S is the sign, k^2 carries the numerator and all multiplicative constants, while ε contains the combination of normal mode frequencies that may give rise to a resonance. The term is then replaced using the following transformation:

$$S\frac{k^2}{2\varepsilon} \longrightarrow S(\sqrt{k^2+\varepsilon^2}-\varepsilon) \tag{2.19}$$

The expression on the right is non-singular even as ε approaches zero. Otherwise, for small k, the two expresions coincide. However, if both k and ε are large, then the DCPT2 expression is no longer close to the correct VPT2 results. To fix this problem, the HDCPT2 method provides a smooth transition between the pure DCPT2 and the VPT2 expressions by weighting the two contributions by Λ and $(1-\Lambda)$, respectively, where the weight is defined as:[25]

$$\Lambda = \frac{\tanh(\alpha(|k\varepsilon|-\beta))+1}{2} \tag{2.20}$$

Where α and β are empirical parameters which control the smoothness of the transition between the DCPT2 and VPT2.

It should be emphasized that without a reliable, automatic, and reasonably black-box and user-firendly method for treating resonances, it would be practically impossible to apply VPT2 to larger molecular systems since the number of possible resonant states tends to increase with system size, so a manual analysis of all offending terms would be prohibitively laborious.

2.3 Anharmonic polarizabilities

Vibrational perturbation theory provides closed expressions for the anharmonic energies and wavefunctions, however the focus of this work is directed towards the application of these concepts to the linear and nonlinear light scattering of solvated systems. Light absorption and dispersion phenomena which are first order with respect to the light-matter interaction (i.e. purely electric phenomena) can be thought as originating from the induced oscillation of the molecular dipole moment, which is related to the external electric field through the molecular polarizability. Most common spectroscopic phenomena can then be related to the polarizability itself. For instance, in a one-photon absroption experiment it can be shown[10] that the intensity change $\mathrm{d}\, I$ due to absorption of monochromatic light of angula frequency ω traveling in the z direction within an isotropic sample can be expressed as:

$$-\frac{\mathrm{d}\ln I}{\mathrm{d}\, z} = N\frac{4\pi}{3}\frac{\omega}{c}\sum_{\alpha}\alpha_{\alpha\alpha}(g) \tag{2.21}$$

where N is the numeral density of the absorbing species and $\alpha(g)$ is the absorbitive (imaginary) component of polarizability. The simplification of the transition polarizability tensor in the context of resonant and nonresonant Raman scattering was presented in Chapter 1. We now analyze how the VPT2 model can be applied to the computation of the anharmonic contributions to the polarizability itself (both real and imaginary parts) as well as to the Raman transition polarizability.

Let's suppose that the molecule under investigation is in the electronic ground state and in a possibly excited vibrational state $|n\rangle$. The sum-over-states expression of the polarizability can be separated in an electronic contribution, which is a sum over all excited electronic states, and a purely vibrational one where the summation runs over the vibrational states lying

on the ground Potential Energy Surface (PES):[26,27]

$$\alpha_{\alpha\beta} = \langle \alpha^{\mathrm{el}}_{\alpha\beta} \rangle + \alpha^{\mathrm{vib}}_{\alpha\beta} = \\ = \langle n | \left(\frac{2}{\hbar} \sum_{j \neq 0}^{\mathrm{el}} \frac{\omega_{j0}}{\omega_{j0}^2 - \omega^2} \langle 0 | \mu_\alpha | j \rangle \langle j | \mu_\beta | 0 \rangle \right) | n \rangle + \frac{2}{\hbar} \sum_{m \neq n}^{\mathrm{vib}} \frac{\omega_{mn}}{\omega_{mn}^2 - \omega^2} \langle n | \mu^{\mathrm{el}}_\alpha | m \rangle \langle m | \mu^{\mathrm{el}}_\beta | n \rangle \tag{2.22}$$

The first term is a vibrational average of the purely electronic polarizability, the second term is the pure vibrational polarizability and the dipoles that appear in its expressions have already been integrated over the electronic degrees of freedom ($\vec{\mu}^{\mathrm{el}} = \langle 0 | \vec{\mu} | 0 \rangle$). Both expressions contain two types of quantities: electrical (the electronic polarizability and dipole moment), and mechanical (the vibrational wavefunctions), both of which can be a source of anharmonicity. The former quantities depend on the molecular geometry and can be expanded in Taylor series around the equilibrium structure using the normal modes as variables:

$$\alpha^{\mathrm{el}} = \alpha^{\mathrm{el}}_0 + \sum_a \left(\frac{\partial \alpha^{\mathrm{el}}}{\partial q_a} \right) q_a + \dots \tag{2.23}$$

$$\mu^{\mathrm{el}} = \mu^{\mathrm{el}}_0 + \sum_a \left(\frac{\partial \mu^{\mathrm{el}}}{\partial q_a} \right) q_a + \dots \tag{2.24}$$

The expansions can be truncated at the desired order, however usually one chooses to retain only the lowest-order terms that give a nonzero contribution once they are plugged in equation 2.22. If the VPT2 vibrational wavefunctions are used ($\langle v | = \langle v^{(0)} | + \langle v^{(1)} | + \langle v^{(2)} |$) then we can write the vibrationally averaged electronic polarizability as the sum of a purely electronic term computed at the equilibrium geometry, plus a vibrational correction:[26,27]

$$\langle \alpha^{\mathrm{el}}_{\alpha\beta} \rangle = \alpha^{\mathrm{el}}_0 + \Delta_{\mathrm{vib}} \alpha^{\mathrm{el}} \tag{2.25}$$

$$\Delta_{\mathrm{vib}} \alpha^{\mathrm{el}} = -\frac{1}{4} \sum_a \frac{1}{\hbar \omega_a} \left(\frac{\partial \alpha^{\mathrm{el}}}{\partial q_a} \right) \sum_b k_{abb} (2 n_b + 1) + \frac{1}{4} \sum_a \left(\frac{\partial^2 \alpha^{\mathrm{el}}}{\partial q_a^2} \right) (2 n_a + 1) \tag{2.26}$$

In this case the mechanical anharmonicity enters through the semi-diagonal cubic force constant k_{abb} and there is no contribution from the second-order terms. The pure vibrational contribution is much more difficult to handle because the full anharmonic wavefunction must be used, and the derivatives of the dipole moment up to the third order are included. The total anharmonic polarizability is partitioned into four contributions according to the degree of anharmonicity, specified using two apices, the frist one denoting the electric anharmonicity, and the second one denoting the mechanic anharmonicity, respectively:

$$\alpha^{\text{vib}}_{\alpha\beta} = [\mu^2]^{0,0} + [\mu^2]^{2,0} + [\mu^2]^{1,1} + [\mu^2]^{0,2} \tag{2.27}$$

$$[\mu^2]^{0,0} = \sum_a \lambda_a X_a Y_a$$

$$[\mu^2]^{2,0} = \frac{1}{4}\sum_{ab}\Big\{X_{ab}Y_{ab}\left[\lambda_{a+b}(n_a+n_b+1) - \lambda_{a-b}(n_a-n_b)\right] + (X_aY_{abb} + Y_aX_{abb})\lambda_a(2n_b+1)\Big\}$$

$$\begin{aligned}[\mu^2]^{1,1} = \frac{1}{4}\sum_{abc}\Bigg\{&(X_{ab}Y_c + Y_{ab}X_c)k_{abc}\left[\frac{\lambda_{a+b}\omega_c(n_a+n_b+1)}{(\omega_a+\omega_b)^2-\omega_c^2} - \frac{\lambda_{a-b}\omega_c(n_a-n_b)}{(\omega_a-\omega_b)^2-\omega_c^2}\right.\\ &\left.- \frac{\lambda_c\left[\omega_a(\omega_a^2-\omega_b^2-\omega_c^2)(2n_b+1) + \omega_b(\omega_b^2-\omega_a^2-\omega_c^2)(2n_a+1)\right]}{\Delta_{abc}}\right]\\ &- (X_{ab}Y_a + Y_{ab}X_a)k_{bcc}\frac{\lambda_a(2n_c+1)}{\omega_b}\Bigg\}\end{aligned}$$

$$\begin{aligned}[\mu^2]^{0,2} = &\frac{1}{8}\sum_{ab}\left\{-X_aY_ak_{aabb}\frac{\lambda_a(2n_b+1)}{\omega_a} + \sum_{c\neq a}(X_aY_c + Y_cX_a)\,k_{abbc}\frac{2\lambda_a\omega_c(2n_b+1)}{(\omega_a^2-\omega_c^2)}\right\}\\ &+\frac{1}{8}\sum_{abcd}\Bigg\{(X_cY_d + Y_cX_d)\,k_{abc}k_{abd}\omega_c\omega_d\left[\frac{\lambda_{a+b}(n_a+n_b+1)}{[(\omega_a+\omega_b)^2-\omega_c^2][(\omega_a+\omega_b)^2-\omega_d^2]}\right.\\ &\left.-\frac{\lambda_{a-b}(n_a-n_b)}{[(\omega_a-\omega_b)^2-\omega_c^2][(\omega_a-\omega_b)^2-\omega_d^2]}\right]\Bigg\} + \frac{1}{8}\sum_{abc}\Bigg\{X_aY_a\Bigg[k_{aab}k_{bcc}\frac{\lambda_a(2n_c+1)}{\omega_a\omega_b}\\ &-k_{abc}^2\frac{2\lambda_a\omega_b\left[(\omega_a^2-\omega_b^2)^2(3\omega_a^2-\omega_b^2) + (3\omega_a^4+2\omega_a^2\omega_b^2+3\omega_b^4)\omega_c^2 - (7\omega_a^2+3\omega_b^2)\omega_c^4 + \omega_c^6\right](2n_c+1)}{\Delta_{abc}^2\omega_a}\Bigg]\\ &+\sum_{d\neq c}(X_cY_d + Y_cX_d)\left[k_{aab}k_{bcd}\frac{2\lambda_d\omega_c(2n_a+1)}{\omega_b(\omega_c^2-\omega_d^2)}\right.\\ &\left.-k_{abc}k_{abd}\frac{2\lambda_c\omega_d\left[\omega_a(\omega_a^2-\omega_b^2-\omega_c^2)(2n_b+1) + \omega_b(\omega_b^2-\omega_a^2-\omega_c^2)(2n_a+1)\right]}{\Delta_{abc}(\omega_c^2-\omega_d^2)}\right]\Bigg\}\\ &-\frac{1}{2}\sum_{\alpha=x,y,z}B^e_\alpha\sum_{abc}\Bigg\{(X_aY_c + Y_aX_c)\zeta^\alpha_{ab}\zeta^\alpha_{bc}\lambda_a\Bigg[\frac{\sqrt{\omega_a\omega_c}}{\omega_b}\left(\frac{1}{\omega_a+\omega_c} + \frac{1-\delta_{ac}}{\omega_a-\omega_c}\right)\\ &-\frac{\omega_b}{\sqrt{\omega_a\omega_c}}\left(\frac{1}{\omega_a+\omega_c} - \frac{1-\delta_{ac}}{\omega_a-\omega_c}\right)\Bigg](2n_b+1)\Bigg\}\end{aligned}$$

To simplify notation and improve readability we make the substitutions $\mu_\alpha^{\mathrm{el}} \rightarrow X$ and $\mu_\beta^{\mathrm{el}} \rightarrow Y$, while the pedices indicate derivatives with respect to the adimentional normal modes. We also define the quantities $\lambda_a = \nu_a/(\nu_a^2 - \omega^2)$, $\lambda_{a\pm b} = (\nu_a \pm \nu_b)/((\nu_a \pm \nu_b)^2 - \omega^2)$, and $\Delta_{abc} = (\omega_a + \omega_b + \omega_c)(\omega_a - \omega_b + \omega_c)(\omega_a + \omega_b - \omega_c)(\omega_a - \omega_b - \omega_c)$, and ν_a denotes the *anharmonic* vibrational energy of mode a. This formula does not only allow the calculation of the anharmonic pure vibrational polarizability, but can be also used to quickly derive the anharmonic IR absorption intensities. To obtain the IR intensity for the generic transition $|m\rangle \rightarrow |n\rangle$ it is sufficient to take the limit $\omega \rightarrow (\nu_m - \nu_n)$ and only retain the singular terms. Intensities for the fundamental bands, first overtones, and 1+1 combination bands can be obtained this way. For example, in the case of a first overtone band $|0\rangle \rightarrow |2_i\rangle$, the singularity only appears within terms proportional to λ_{a+b}, with $a = b = i$. By discarding all other terms and setting all quantum numbers equal to zero we obtain:

$$\lim_{\omega \longrightarrow 2\nu_i} \alpha_{\alpha\beta}^{\mathrm{vib}} = \left(\frac{1}{4} X_{ii} Y_{ii} + \frac{1}{4} \sum_c (X_{ii} Y_c + Y_{ii} X_c) k_{iic} \frac{\omega_c}{4\omega_i^2 - \omega_c^2} + \right.$$
$$\left. + \frac{1}{8} \sum_{cd} (X_c Y_d + Y_c X_d) k_{iic} k_{iid} \frac{\omega_c \omega_d}{(4\omega_i^2 - \omega_c^2)(4\omega_i^2 - \omega_d^2)} \right) \lambda_{i+i} \tag{2.28}$$

The term λ_{i+i} is singular. As argued in section 1.3, to resolve the singularity we must introduce an imaginary component within the excited state energies to account for their finite lifetime, i.e. we make the substitution $\nu_i \longrightarrow \nu_i + i\gamma$. The denominator found in a generic term λ_j becomes:

$$\frac{1}{\nu_j^2 - \omega^2} \rightarrow \frac{(\nu_j^2 - \omega^2) + i2\omega\gamma}{(\nu_j^2 - \omega^2)^2 + 4\omega^2\gamma_j^2} = f(\omega) + ig(\omega) \tag{2.29}$$

Under resonance conditions (as the radiation frequency ω approaches the transition energy ν_j) the real part $f(\omega)$ is negligible, whereas the imaginary

part can be further simplified:*

$$\lambda_j = \frac{4\omega\nu_j\gamma}{\left(\nu_j^2 - \omega^2\right)^2 + 4\omega^2\gamma^2} \approx \pi\left(\frac{1}{\pi}\frac{\gamma}{\left(\omega - \nu_j\right)^2 + \gamma^2}\right) \tag{2.30}$$

The part enclosed in parentheses is a Lorentzian distribution. The polarizability can then be plugged in equation 2.21 to obtain the full IR intensity.

To compute anharmonic Raman intensities we must calculate the anharmonic transition polarizability. In Section 1.5 it was argued that the pure vibrational component of the transition polarizability can be neglected because the incident frequency, which appears in the denominator of the sum-over-state expansion, usually lies in the visible range of the spectrum. What remains is $\langle m|\alpha^{\mathrm{el}}|n\rangle$, where the electronic polarizability can be expanded in a Taylor series as shown in equation 2.23, while the anharmonic vibrational wavefunctions are used for both states $|n\rangle$ and $|m\rangle$. The actual Raman intensity I is quadratic in the polarizability, therefore it can be obtained by simply using a formula equivalent to equation 2.27:

$$I_{\mathrm{Raman}} \propto [\alpha^2]^{0,0} + [\alpha^2]^{2,0} + [\alpha^2]^{1,1} + [\alpha^2]^{0,2} \tag{2.31}$$

Each term is expanded in the same way, but the dipole moments are replaced by the polarizabilities ($\alpha^{\mathrm{el}}_{\alpha\beta} \rightarrow X$ and $\alpha^{\mathrm{el}}_{\gamma\delta} \rightarrow Y$) and, as in the case of IR absorption, only the residues corresponding to the desired transition are kept. The rotational invariants which form the Raman activity can then be computed, and the Raman cross-section is easily derived by further multiplication by the frequency dependent factor, as

*This procedure must be done with great care. The first part of the denominator is treated by using the relation $\left(\nu_j^2 - \omega^2\right)^2 = (\nu_j + \omega)^2(\nu_j - \omega)^2 \approx 4\omega^2(\nu_j - \omega)^2$, and the $4\omega^2$ is subsequently simplified. Since we want to keep a frequency dependence we can't just set $\nu_j = \omega$.

A Lorentzian distribution is normalized in the following way:

$$\frac{1}{\pi}\int_{-\infty}^{+\infty} \frac{\gamma}{(\omega-\omega_0)^2+\gamma^2}\,\mathrm{d}\,\omega = \frac{1}{\pi}\int_{-\infty}^{+\infty} \frac{1}{(\frac{\omega-\omega_0}{\gamma})^2+1}\,\mathrm{d}\,\frac{\omega}{\gamma} = \frac{1}{\pi}\Big[\arctan\frac{\omega-\omega_0}{\gamma}\Big]_{-\infty}^{+\infty} = 1$$

described in section 1.7.

There is an alternative and equally rigorous way of obtaining the VPT2 IR and Raman intensities: rather than expanding the intensities directly, one can first compute the anharmonic transition dipole moment (for IR) or polarizability (for Raman) and only then square the result to obtain the intensity.[28,29] The resulting expressions are slightly different because, when the transition property is squared, the products of higher order terms from the two factors are included, whereas they are discared when the intensities are expanded directly. High order perturbative corrections, however, are expected to be small, therefore there should be very little numerical difference between the two methods. Note that this difference only manifests itself for fundamental bands, in fact the overtone intensity shown in equation 2.28 exactly coincides with the one previously derived from the expansion of the transition dipole moment.[29,30] It should also be mentioned that the dipole-expression has also been generalized to the calculation of anharmonic vibrational circular dichroism spectra (VCD).[31] In the case of fundamental bands the resulting expression for the transition dipole moment, polarizability, or atomic axial tensor (used for VCD) is as follows:

$$
\begin{aligned}
\langle 0|X|1_i\rangle = {} & \frac{s_0}{\sqrt{2}} \times \mathrm{S} \times X_i + \frac{s_2}{12\sqrt{2}} \sum_j \{X_{jij} + X_{ijj} + \mathrm{S}X_{jji}\} - \frac{s_0}{8\sqrt{2}} \sum_{jk} k_{ijkk} X_j \left[\frac{1}{\omega_i + \omega_j} - \frac{\mathrm{S}(1-\delta_{ij})}{\omega_i - \omega_j}\right] \\
& - \frac{s_1}{16\sqrt{2}} \sum_{jk} \left\{ k_{ijk} \left(X_{jk} + X_{kj}\right) \left(\frac{1}{\omega_i + \omega_j + \omega_k} - \frac{\mathrm{S}}{\omega_i - \omega_j - \omega_k}\right) + \frac{k_{jkk}}{\omega_j} \left[2\mathrm{S}X_{ji} + (1+\mathrm{S})X_{ij}\right] \right\} \\
& + \frac{s_0}{2\sqrt{2}} \sum_{jk} \left(\sum_{\alpha=x,y,z} B^e_\alpha \zeta^\alpha_{ik} \zeta^\alpha_{jk} \right) X_j \left\{ \frac{\sqrt{\omega_i \omega_j}}{\omega_k} \left(\frac{1}{\omega_i + \omega_j} + \frac{\mathrm{S}(1-\delta_{ij})}{\omega_i - \omega_j}\right) - \frac{\omega_k}{\sqrt{\omega_i \omega_j}} \left(\frac{1}{\omega_i + \omega_j} - \frac{\mathrm{S}(1-\delta_{ij})}{\omega_i - \omega_j}\right) \right\} \\
& + \frac{s_0}{16\sqrt{2}} \sum_{jkl} k_{ikl} k_{jkl} X_j \left\{ (1-\delta_{ij})(1-\delta_{ik})(1-\delta_{il}) \left[\frac{1}{(\omega_i + \omega_j)(\omega_j + \omega_k + \omega_l)} - \frac{\mathrm{S}}{(\omega_i - \omega_j)(\omega_j + \omega_k + \omega_l)} \right.\right. \\
& \quad + \frac{\mathrm{S}}{(\omega_i + \omega_k + \omega_l)(\omega_j + \omega_k + \omega_l)} - \frac{1}{(\omega_i - \omega_k - \omega_l)(\omega_j + \omega_k + \omega_l)} + \frac{\mathrm{S}}{(\omega_i - \omega_j)(\omega_i - \omega_k - \omega_l)} \\
& \quad \left. + \frac{1}{(\omega_i + \omega_j)(\omega_i + \omega_k + \omega_l)} \right] \\
& + \delta_{ij}(1+\delta_{ik})(1-\delta_{il}) \left[\frac{1}{2\omega_i(\omega_i + \omega_k + \omega_l)} - \frac{1}{2\omega_i(\omega_i - \omega_k - \omega_l)} + \frac{\mathrm{S}}{2(\omega_i + \omega_k + \omega_l)^2} \right. \\
& \quad \left. - \frac{\mathrm{S}}{2(\omega_i - \omega_k - \omega_l)^2} \right] \\
& + (1-\delta_{ij})(1-\delta_{ik})\delta_{il} \left[\frac{1}{\omega_k(\omega_i + \omega_j)} + \frac{2}{(2\omega_i + \omega_k)(\omega_i + \omega_j)} + \frac{3}{(\omega_i + \omega_j)(\omega_i + \omega_j + \omega_k)} \right. \\
& \quad + \frac{\mathrm{S}}{(\omega_i - \omega_j)(\omega_i - \omega_j - \omega_k)} - \frac{2\mathrm{S}}{(\omega_i - \omega_j)(\omega_i + \omega_j + \omega_k)} - \frac{3\mathrm{S}}{\omega_k(\omega_i - \omega_j)} \\
& \quad \left.\left. - \frac{\mathrm{S}}{\omega_k(\omega_i - \omega_j - \omega_k)} + \frac{2\mathrm{S}}{(2\omega_i + \omega_k)(\omega_i + \omega_j + \omega_k)} + \frac{3}{\omega_k(\omega_i + \omega_j + \omega_k)} \right] \right\} \\
& + k_{ijk} k_{llk} X_j \left\{ \frac{\delta_{ij}}{\omega_i \omega_k} \left(1 + \frac{\delta_{ik}\delta_{il}(6 - 4\mathrm{S})}{9}\right) \right. \\
& \quad + (1-\delta_{ij})(1-\delta_{ik})(1-\delta_{il}) \left[\frac{1}{(\omega_i + \omega_j)(\omega_i + \omega_j + \omega_k)} + \frac{1}{\omega_k(\omega_i + \omega_j)} - \frac{\mathrm{S}}{\omega_k(\omega_i - \omega_j)} \right. \\
& \quad \left. + \frac{\mathrm{S}}{(\omega_i - \omega_j)(\omega_i - \omega_j - \omega_k)} + \frac{1}{\omega_k(\omega_i + \omega_j + \omega_k)} - \frac{\mathrm{S}}{\omega_k(\omega_i - \omega_j - \omega_k)} \right] \\
& \quad + \delta_{ik}(1-\delta_{ij}) \left[(1+\delta_{il}) \left(\frac{1}{(2\omega_i + \omega_j)(\omega_i + \omega_j)} - \frac{\mathrm{S}}{\omega_i(\omega_i - \omega_j)} + \frac{1}{\omega_i(2\omega_i + \omega_j)} \right) \right. \\
& \quad + \delta_{il} \left(\frac{1}{3\omega_i(\omega_i + \omega_j)} + \frac{\mathrm{S}}{3\omega_i(2\omega_i + \omega_j)} - \frac{\mathrm{S}}{(\omega_i - \omega_j)(2\omega_i + \omega_j)} \right) \\
& \quad \left.\left. + \frac{1}{\omega_i(\omega_i + \omega_j)} - \frac{\mathrm{S}}{\omega_j(\omega_i - \omega_j)} + \frac{\mathrm{S}}{\omega_i \omega_j} \right] \right\}
\end{aligned}
\tag{2.32}
$$

where the constants s_0, s_1, s_2, and S, depend on the type of spectroscopy: $s_0 = s_1 = s_2 = S = 1$ for IR and Raman, while $s_0 = i\hbar$, $s_1 = 2i\hbar$, $s_2 = 3i\hbar$, and $S = -1$ for VCD. One final issue must be addressed. It can be seen that in $[\mu^2]^{0,2}$, which accounts for the second-order mechanical anharmonicity, there are some terms whose denominators are of the type $\omega_a - \omega_b$. If any two normal modes are very close in energy, these denomi-

nators may cause the computed anharmonic intensities to be unphysically large compared to their harmonic counterparts. Unfortunately, the methods previously discussed used to treat resonances in the case of energies, do not apply. An simple, albeit approximate, way to deal with this type of resonances is to identify the resonant terms and, if the numerator is not small enough to mitigate the effect of the resonance, remove the whole term from the expression.

Chapter 3

Solvation effects on spectroscopic observables

One of the main themes in this work is the inclusion of solvation effects within the computational description of spectroscopic properties in general, and Raman spectroscopy in particular, with an emphasis on the inclusion of such effects both at the electronic and vibrational level, as well as the effect of the solvent on the electromagnetic radiation used to probe the spectroscopic response, and the dynamical aspects of solvation. Solvation effects are relevant in a multitude of chemical problems and in the realm of spectroscopy in particular since most spectroscopic experiments are actually carried out on solutions. The reason is not limited to the difficulty in the production, handling, and analysis of gaseous samples, but also to the fact that many systems' natural environment is the solvated state, and the definition of the "system" of interest is more appropriately attributed to the solution as a whole rather than the solute itself. Biological systems, for instance, owe part of their biochemical behavior to the properties of their environment, and neglecting completely such effects, while providing useful insights into the properties of the solute, may yield results which do not apply to the same system in the solvated state. The inclusion of solvent effects in the theoretical models allows the computation of spectroscopic properties which are directly comparable to

their experimental counterparts.

3.1 Computational modeling of solvated system

From the point of view of the computational modeling of molecular systems, solutions are particularly challenging because of the seemingly gargantuan increase in the dimensionality of the problem. A naïve approach to an atomistic treatment of the whole system would be to consider the solute surrounded by a sufficient number of solvent molecules to adequately describe the solute-solvent interactions, as well as the direct and indirect effects of the solvent on the molecular and spectroscopic properties of the solute, and then perform a quantum mechanical calculation on the resulting cluster, in the same way one would treat an isolated system. This approach however is problematic in two ways: first, the number of degrees of freedom that should be treated is too great to be amenable with most QM methods and, most importantly, a single solute-solvent configuration cannot possibly be considered to be representative of the real system.

To solve these two problems, two limiting approaches can be employed. On one end, one can rely on classical Molecular Dynamics (MD) to adequately sample the configuration space of the solute-solvent system, and thus generate a number of representative systems on which to perform the QM calculations. For the latter, the solvent molecules can be treated at a lower level of theory with respect to the solute part to reduce the computational cost. This approach has the advantage of preserving an atomistic description of the solvent, though the computational cost is much greater than a corresponding gas-phase calculation since, in addition to the need of defining the solute-solvent interaction and its inclusion in the Hamiltonian of the solute, the calculation has to be repeated for each system in the ensemble, and the reliability of the results is greatly affected by the quality of the dynamics, which typically relies on a parametrized force-field. A completely opposite approach is constituted by continuum solvation mod-

els where the atomistic description of the solvent is forsaken in favor of an implicit average over all solvent configurations.[32]

In this work we focused on the second choice of solvation models, using in particular the Polarizable Continuum Model (PCM).[32–36] In PCM the solute is placed inside a cavity carved within a polarizable continuum with given dielectric properties, which represents the solvent. The cavity is molecule-shaped and is usually constructed as the union of a set of interlocking spheres centered on the atoms, with radii equal to their van der Waals radii, though more complex shapes are also possible.[35]

The dielectric continuum is characterized by its static (ε_0) and optical (ε_∞) dielectric constants (the latter defined as the square of the refractive index) which are used to determine the response of the medium to static and dynamic electric fields, which can originate from either the solute charge density (determined quantum-mechanically), or from an external perturbation, and are commonly chosen to match those of the desired solvent.

The electric potential V_M due to the electron density and the nuclei of the solute induces a surface charge density σ on the cavity surface Γ, which can be computed using Poisson's equation.[37] The electrostatic potential obeys Maxwell's first law:

$$-\vec{\nabla}\cdot\varepsilon\vec{\nabla}V = 4\pi\rho_\mathrm{M} \tag{3.1}$$

where $\pi\rho_\mathrm{M}$ is the solute's charge density. The potential $V = V_\mathrm{M}+V_\mathrm{R}$ is also continuous, it vanishes at infinity, and its derivative obeys the boundary condition:

$$\left(\frac{\partial V}{\partial n}\right)_{\text{inside cavity}} = \varepsilon\left(\frac{\partial V}{\partial n}\right)_{\text{outside cavity}} \tag{3.2}$$

where n is a versor normal to the cavity surface. It can be shown that the surface charge density can then be obtained using this expression:[37]

$$\left(2\pi\frac{\varepsilon+1}{\varepsilon-1}-\hat{D}\right)\hat{S}\sigma(\vec{s}) = -(2\pi-\hat{D})V_\mathrm{M}(\vec{s}) \tag{3.3}$$

where $\vec{n}_s$ is versor normal to the cavity surface at the point $\vec{s}$, and the following integral operators are defined:

$$\hat{D}\sigma(\vec{s}) = \int_\Gamma \frac{\partial}{\partial \vec{n}_{s'}} \frac{1}{|\vec{s} - \vec{s}'|} \sigma(\vec{s}') \, \mathrm{d}\, \vec{s}' \qquad ; \qquad \hat{S}\sigma(\vec{s}) = \int_\Gamma \frac{1}{|\vec{s} - \vec{s}'|} \sigma(\vec{s}') \, \mathrm{d}\, \vec{s}' \tag{3.4}$$

These operators only depend on the shape of the cavity, while the electrostatic properties on the medium enter explicitly, which can be rewritten using a more compact notation as $\sigma = \hat{Q} V_\mathrm{M} = \langle \Psi | \hat{Q} \hat{V}_\mathrm{M} | \Psi \rangle$, where $\hat{V}_\mathrm{M}$ is the operator form of V_M. We can also define the operator $\hat{\sigma} = \hat{Q}\hat{V}_\mathrm{M}$. This method, which computes the charge density from the potential rather than the field, is called Integral Equation Formalism (IEFPCM).[38] The equations presented here employ an integral formalism and a continuous surface charge density, however all practical implementations have to rely on a discretization procedure in order to represent the charges on the cavity and all PCM operators using finite elements. All the results presented in this work employ the discretization by Scalmani and Frisch,[39] which represents the surface charge using a finite number of charges, lying on the cavity surface, described using spherical Gaussian functions. Other types of discretization exist,[35] and new numerical strategies for the solution of the IEFPCM equations are still being developed.[40]

The electrostatic component of the solute-solvent interaction can then be computed by integrating the product of the electrostatic potential and the charge density over the cavity surface Γ:

$$E_\mathrm{R} = \int_\Gamma \sigma(\vec{s}) V_\mathrm{M}(\vec{s}) \, \mathrm{d}\, \vec{s} \tag{3.5}$$

This solute-solvent electrostatic interaction introduces an additional monoelectronic term in the Hamiltonian of the solute, therefore the electron density of the solute must be recomputed accounting for this additional interaction. Since the surface charge density depends upon the electrostatic potential, the interaction operator is non-linear, therefore the computation must be repeated until self-consistency is achieved. More in detail,

the Hamiltonian of the solvated system is:

$$\hat{H} = \hat{H}_{(\mathrm{g})} + \hat{H}_{\mathrm{R}} = \hat{H}_{(\mathrm{g})} + \int_{\Gamma} \sigma(\vec{s})[\Psi]\hat{V}_{\mathrm{M}}(\vec{s}) \, \mathrm{d}\, \vec{s} \tag{3.6}$$

Where $\hat{H}_{(\mathrm{g})}$ is the Hamiltonian of the isolated system. Solving the equation $\hat{H}|\Psi\rangle = E|\Psi\rangle$ yields the desired wavefunction. Because of the non-linearity of the interaction operator, the expectation value of this Hamiltonian is *not* stationary, in fact the stationarity condition (under the normalization constraint for the wavefunction) is satisfied by the following free energy functional:

$$G[\Psi] = \langle\Psi|\hat{H}_{(\mathrm{g})}|\Psi\rangle + \frac{1}{2}\int_{\Gamma} \sigma(\vec{s})[\Psi]V_{\mathrm{M}}(\vec{s}) \, \mathrm{d}\, \vec{s} \tag{3.7}$$

where the interaction term is halved. The strategy for the resolution of the QM problem for a molecule embedded in a PCM cavity follows what is commonly done for isolated systems, in fact most common quantum chemistry methods can be reformulated to include PCM.[35]

The effect of PCM on the energy alone can have strong consequences for the computed spectroscopic properties since it can cause changes in the conformational distribution of a molecule in solution, to the point the most stable conformer of a molecule in solution may not even exist for the same molecule in the gas phase.[41,42] The presence of the solute-solvent electrostatic interaction term in the Hamiltonian also carries over to the calculation of energy derivatives, including forces (which determine the molecular geometry) and response properties. Therefore, in addition to the direct effect of the polarizable continuum on the energy and electronic density of the solute, there is also an indirect effect on the shape of the whole Potential Energy Surface (PES), with a consequent change in the equilibrium geometry and vibrational manifold of the solute. All molecular properties are affected by the presence of the solvent, and differ from the gas-phase values.

PCM is capable of accurately treating the electrostatic component of solvation, however in its basic formulation it neglects nonelectrostatic in-

teractions such as dispersion and repulsion forces, as well as direct effects such as the directional component of hydrogen bonds. While it is possible to introduce the treatment of nonelectrostatic effects into the model,[43–46] the results presented here only take these effects into account in the estimation of solvation free energies whenever the population distribution of a molecule in solution needs to be accurately determined. Specific solvation effects can be introduced by means of explicit solvation models which treat some solvent molecules atomistically (super-molecule approach),[41,47–52] possibly with a polarizable QM/MM embedding[53–56] however their quality and applicability strongly depends on the system and the property. In general, whenever specific interactions greatly affect the computed property, the choice of a discrete model leads to better results. However, continuum models still play an important role, because the bulk of the solvent can be safely treated as a continuum. Much work has been done in the past in this direction, leading to strategies exploiting non-periodic boundary conditions,[57,58] recently extended to include solute-solvent mutual polarization effects.[6,59–62]

It should be mentioned that originally PCM followed an alternative formulation for the solution of the electrostatic equations:

$$\left(2\pi\frac{\varepsilon+1}{\varepsilon-1}-\hat{D}^{\dagger}\right)\sigma(\vec{s})=\vec{n}_s\cdot\vec{E}_{\mathrm{M}}(\vec{s}) \tag{3.8}$$

where $\vec{E}_{\mathrm{M}}$ is the electrostatic field generated by the solute. This formulation presented numerical instabilities and was therefore replaced by the aforementioned one, however this equation can still be useful for the modeling of cavity field effects (see below).

In the following sections we shall explore the different molecular properties classified according to the nature and the frequency of the probing electromagnetic field, but first it is necessary to investigate the effect of the solvent on the electromagnetic field itself, since it is the latter that generates the molecular response and, as will be shown later, the effect of the solvent on the electromagnetic field can be of the same order as the effect on the solute itself.

3.2 Spectroscopic properties in a PCM framework

One of the most powerful characteristics of PCM is the fact that it can be effectively used to not only model the energetics of solvated systems, but also employed for the calculation of molecular properties and spectroscopic intensities by redefining the quantum-mechanical quantities that relate to the target property to include PCM terms that can be derived from the expression of the Hamiltonian of the solute embedded within the cavity. In modern implementations the cost of such property calculations do not significantly differ from the corresponding calculations performed for the isolated system, making PCM a very cost-effective method to include solvation effects in most QM calculations.

In general, molecular properties, including electric and/or magnetic field-induced ones which can be related to spectroscopic responses, can be expressed by means of response theory, and then related to appropriate derivatives of the free energy of the (solvated) system. As detailed in the previous section, in PCM the molecular free energy contains explicit terms which must be carried in all analytical expressions of energy derivatives, and response equations. Note however that particular care has to be taken in this case, for the response of the medium to an oscillating field differs from the static case, therefore a *nonequilibrium* free energy must be employed in this case, depending on the timescale of the phenomenon under study. The phenomenological aspects of nonequilibrium solvation in the context of spectroscopy will be discussed in more detail in the following sections.

The extension of derivative methods commonly employed for the calculation of molecular properties of gaseous systems to PCM is possible thanks to the fact that the free energy obeys the Hellmann-Feynman theorem for variational wavefunctions:[63]

$$\frac{\mathrm{d}\,G}{\mathrm{d}\,x} = \langle\Psi|\frac{\partial H}{\partial x}|\Psi\rangle \tag{3.9}$$

PCM has thus been implemented for the calculation of molecular forces and harmonic frequencies[64–69] (related to the first and second geometrical derivatives of the energy, respectively), which paved the way for the calculation of Infra-Red spectroscopic intensities for molecules in solution under vibrational nonequilibrium conditions.[70,71] This formalism has also been extended to the calculation of Raman spectra,[72–74] which are related to the derivatives of the electronic polarizability, and its chiral variant, Raman Optical Activity.[75] PCM has also been used to model polarizabilities and higher-order electric field properties of solvated systems,[76–80] as well as magnetic-field properties,[81–86] for which the problem of the gauge-dependence of the computed values has also been addressed. Finally, PCM has also been extended to the modeling of excited-state properties of solvated systems,[87–90] allowing the simulation of absorption and emission spectra.

For these reasons, in this work, we chose to rely on PCM to include solvent effects in all our calculations, especially considering that the evaluation of anharmonic effects in a VPT2 approach, presented in the previous chapter, relies on a large number of numerical derivatives of the force constants and molecular properties, therefore we require a very reliable, cost-effective, and numerically stable method that is able to include solvation effects in both the PES, and in all molecular properties we wished to consider.

3.3 The effect of the solvent on the electromagnetic field

The most common method of choice for probing molecular properties is spectroscopy, where the system is exposed to an external static or dynamic electromagnetic field, and the response of the system (usually in the form of a scattered radiation) is recorded. From the theoretical and computational point of view, molecular properties can be related to the derivatives of the energy with respect to the electromagnetic field interacting with

the system or an internal perturbation, such as a molecular vibration or the magnetic moments of the nuclei.[26] As explained in the previous section, the presence of the solvent alters the electronic density and the PES of the solute, therefore there are both direct and indirect effects to all molecular properties of the solvated systems with respect to the gas phase values. The solvent, however, also affects the external electromagnetic field before it can reach the solute and generate the molecular response, therefore, from the theoretical point of view, all energy derivatives with respect to the electromagnetic field must be redefined to take this effect into account in order to compute quantities that can directly compared with their experimental counterparts.

Early attempts to address this problem lead to the widely used Onsager model,[91] which treats the solute as a point dipole $\vec{\mu}$ placed at the center of a spherical cavity of radius a within a polarizable medium, with dielectric constant ε, representing the solvent. The point dipole naturally induces a charge density on the cavity surface therefore, in the absence of external fields, the molecule experiences only what is commonly referred as the *reaction field* $\vec{E}_{\mathrm{R}}$ due to this dielectric polarization. If an external static electric field $\vec{E}_{\mathrm{ext}}$ is applied to the system, it will be screened by the dielectric before it can reach the molecule, resulting in a *cavity field* $\vec{E}_{\mathrm{C}}$ which is different than the external one. Under these strict assumptions the local electric field at the center of the cavity can be analytically computed as:[91]

$$\vec{E}_{\mathrm{loc}} = \vec{E}_{\mathrm{C}} + \vec{E}_{\mathrm{R}} = \frac{3\varepsilon}{2\varepsilon+1}\vec{E}_{\mathrm{ext}} + \frac{2(\varepsilon-1)}{2\varepsilon+1}\frac{\vec{\mu}}{a^3} \tag{3.10}$$

This equation is also valid in the case of dynamic fields if the dielectric constant ε is replaced with the square of the refractive index of the medium n^2 in the expression for E_{C}. While this model is very useful for the description of the phenomenological aspects of the problem, and for the definition of the different contributions that are present in the physical system, it relies on rather strong assumptions. A notable consequence is that the resulting cavity field factor is the same for all solutes, and only

depends on the dielectric properties of the solvent.

PCM can effectively model all these effects more realistically, as the dielectric continuum interacts with the whole density of the solute computed quantum-mechanically, rather than with the sole dipole term, while the cavity is molecule-shaped, therefore it differs for every solute. For gas-phase calculations of electric-field properties, such as the electronic polarizability, the energy is differentiated with respect to the external applied field, but for solutions the external field should be replaced with the cavity field actually experienced by the molecule. The problem can also be reformulated by considering the external field as acting on an *effective* dipole moment, which is the sum of the molecular dipole moment $\vec{\mu}$ and the dipole moment $\tilde{\mu}$ arising from the polarization induced by the solute on the cavity surface:[70,79,92]

$$\vec{\mu}_{\text{eff}} = \vec{\mu} + \tilde{\mu} \tag{3.11}$$

It can be shown[70] that this formulation, based on an effective molecular dipole moment, is equivalent to the one previously introduced. As will be explained in greater detailed in the following sections, this effective dipole moment replaces the molecular dipole moment in all calculations involving the perturbing field, e.g. in the response calculations used to compute molecular polarizabilities.

The term $\tilde{\mu}$ only depends on the shape of the cavity and the dielectric properties of the medium. To derive a formula for its computation we can consider the interaction energy between the external field and the surface charge density on the cavity:

$$\int_\Gamma \sigma(\vec{s}) V^{\text{ext}}(\vec{s})\,\mathrm{d}\,\vec{s} = \int_\Gamma \hat{Q} V_{\text{M}}(\vec{s}) V^{\text{ext}}(\vec{s})\,\mathrm{d}\,\vec{s} = \int_\Gamma \sigma^{\text{ext}}(\vec{s}) V_{\text{M}}(\vec{s})\,\mathrm{d}\,\vec{s} \tag{3.12}$$

where the newly defined σ^{ext} is the surface charge density induced on the cavity surface by the external electric field. This interaction can be expanded in multipole moments, and the term that is linear in the external

electric field is, of course, the dipole term:

$$\begin{aligned} -\tilde{\mu}\cdot\vec{E}_{\text{ext}} &= \int_\Gamma V_{\text{M}}(\vec{s})\frac{\partial\sigma^{\text{ext}}(\vec{s})}{\partial\vec{E}_{\text{ext}}}\cdot\vec{E}_{\text{ext}}\,\mathrm{d}\,\vec{s} \quad\Longrightarrow \\ \Longrightarrow\quad \tilde{\mu} &= -\int_\Gamma V_{\text{M}}(\vec{s})\frac{\partial\sigma^{\text{ext}}(\vec{s})}{\partial\vec{E}_{\text{ext}}}\,\mathrm{d}\,\vec{s} = -\int_\Gamma V_{\text{M}}(\vec{s})\hat{U}\vec{n}_s\,\mathrm{d}\,\vec{s} \end{aligned} \tag{3.13}$$

therefore the calculation of the effective dipole only requires the molecular electrostatic potential computed at the cavity surface and the construction of the operator $\hat{U}$ (from equation 3.8), which only depends on the cavity shape and the dielectric constant. In particular, the static dielectric constant is used for static fields, while the optical dielectric constant is used in the case of dynamic fields. Note that the calculation of some properties requires the differentiation of the dipole moment (e.g. Infra-Red intensities). In those cases explicit cavity field terms may appear where the dipole moment $\tilde{\mu}$ is also differentiated.

3.4 Dynamic aspects of solvation

A solvated system is not a static entity, it evolves in time with all its degrees of freedom, each with its own characteristic timescale. Because of the coupling established by the solute-solvent interactions, the evolution of the solvent is not independent of the solute: the solvent responds to changes in the solute's electronic density, geometry, and vibrational state. However, since the translational, rotational, vibrational, and electronic degrees of freedom of any molecule naturally evolve with very different characteristic timescales, a solvent may not instantaneously readapt itself to fast changes in the solute, entering a nonequilibrium configuration. These considerations are of particular relevance in the context of molecular properties that are probed by dynamic electromagnetic fields. These include frequency-dependent electric polarizabilities and hyperpolarizabilities, spectroscopic observables such as infra-red or UV-vis spectra, nuclear magnetic shieldings, and mixed electric-magnetic properties such as optical rotations.

A dielectric medium's response to a dynamic electromagnetic field is usually modeled via its dynamic dielectric constant, which is in general separated into its real and imaginary parts, to model both dispersion and absorption phenomena, however the imaginary part can be neglected when the frequency of the radiation lies within regions of the spectrum where the material is not absorptive. Figure 3.1 shows, as an example, the real part of the water dielectric constant plotted against the frequency of the radiation.[93] In the visible region of the spectrum it assumes an almost constant value of 1.78, in contrast to the static value of 78.3. This huge difference is mainly due to the fact that, for static fields, the water molecules are able to respond to the perturbation with all their degrees of freedom, including the translational ones, resulting in a partial alignment of the water molecules along the direction of the applied electric field, whereas for a visible radiation the frequency of oscillation is too high for such a rearrangement to take place. Similar considerations apply in the context of molecular properties of solvated systems, where the charge density of the solute evolves in time with a frequency that, for first-order properties, is equal to the one of the incident radiation. The solvent cannot follow the evolution of the solute with all its degrees of freedom and, depending on the characteristic timescale of the perturbation, some of them shall remain static, hence a nonequilibrium configuration is created. If the radiation is in the UV range of the spectrum, the solvent can only respond with its electronic degrees of freedom, while the vibrational, rotational, and translational ones remain static.

These effects can be formalized in PCM by separating the solvent polarization $\vec{P}$ into an equilibrium and a nonequilibrium contribution, the first accounting for the degrees of freedom of the solvent which can be considered fast with respect to the time evolution of the solute, and the second accounting for the "slow" degrees of freedom, which remain static:[71,87]

$$\vec{P} = \vec{P}_{\text{fast}} + \vec{P}_{\text{slow}} \tag{3.14}$$

The selection of the fast and slow degrees of freedom is dependent on the

particular timescale of the phenomenon under study, so, for instance, if the incident radiation lies in the mid-infrared region then the vibrational degrees of freedom contribute to the fast component of the solvent polarization. This binary partitioning of the solvent polarization is, of course, an approximation, and may not hold for all frequencies.

In PCM the fast and slow components of the solvent polarization are represented by two distinct surface charge densities, and while the first is computed using the static dielectric constant of the solvent, the latter is computed using the frequency-dependent dynamic dielectric constant. The details of this kind of calculations depend on the specific type of properties to be computed. The relevant literature will be referred in later chapters.

Even in the absence of external fields, the problem of nonequilibrium solvation arises when the vibrational properties of the solute are taken into consideration. The laws of quantum mechanics require that, even if the temperature of a system approaches absolute zero, the vibrational motion of a system never disappears. The characteristic timescale of a molecular vibration is usually much faster than that of a rotation or translation, therefore as a solute vibrates the corresponding solvent degrees of freedom cannot instantaneously adapt to it, resulting in a nonequilibrium solute-solvent configuration. Conversely, the electronic and vibrational degrees of freedom of the solvent possess the ability to remain at equilibrium with the solute. This effect should be taken into consideration when using PCM to compute the vibrational frequencies and normal modes of a solvated system because, by using the static dielectric constant of the solvent in the computation of the solvent-specific terms involved in the calculation, one would implicitly assume that all degrees of freedom of the solvent are responding instantaneously to the (geometrical) perturbation of the solute. This problem can be addressed in the aforementioned way, by splitting the solvent polarization into two contributions, with the "slow" contribution computed using the *optical* dielectric constant of the solvent.[71] Note that the issue of vibrational nonequilibrium does not only arise in the context of vibrational properties, but also in the computation

of vibrational contributions to electronic properties such as electric polarizabilities and magnetic shieldings, as well as when dealing with vibronic contributions to electronic absorption spectra.[3] Note that in the case of vibrational contributions to electronic properties, as well as for properties that are intrinsically mixed electronic and vibrational, such as Raman spectra, there are two levels of nonequilibrium solvation that should, in principle, be treated:[72] an electromagnetic field in the UV-vis region of the spectrum induces a perturbation on the solute whose timescale is much higher than a molecular vibration, therefore the vibrational motion of the solvent contributes to the "slow" part of the solvent polarization in the determination of the electronic property, while for the computation of the derivatives of the energy and the property itself with respect to the nuclear displacements of the solute (which are used to compute the solute vibrational frequencies, and for the vibrational averaging of the property under consideration) the vibrational degrees of freedom of the solvent contribute to the "fast" component of the solvent polarization (since the characteristic time of a solvent vibration is not significantly different than that of a solute vibration). In the case of pure-vibrational properties, such as Infra-Red (IR) intensities, only the vibrational nonequilibrium need be considered. It should be clear from this brief discussion that any theoretical calculation involving a solvated system should be performed with care, and with a clear understanding of the underlying physical phenomenon in mind, in order to identify the different contributions that give rise to the molecular response, and the best way to compute them.

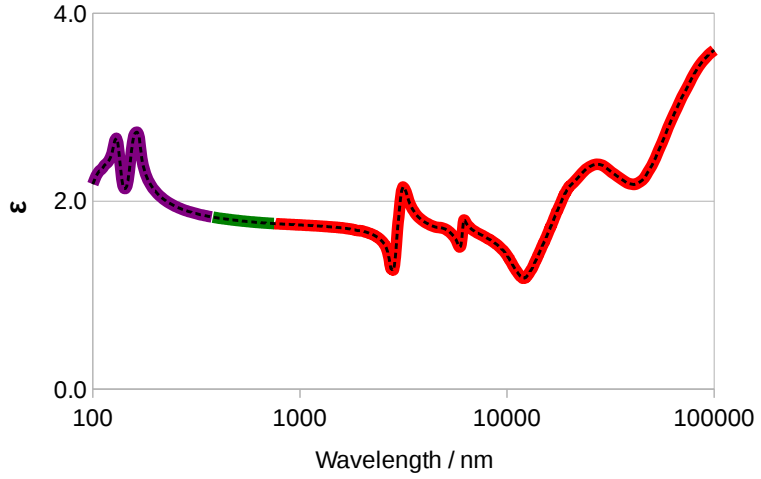

Figure 3.1: Real part of the dielectric constant of water.[93] The line is highlighted in purple, green, and red in the UV, visible, and IR regions of the spectrum, respectively. At infinite wavelength the dielectric constant of water approaches the static value of 78.3.

Chapter 4

The calculation of the electronic polarizability

At the harmonic level of theory, non-resonant Raman spectra can be simulated by computing the geometrical derivatives of the electronic polarizability with respect to the normal modes of vibration of the system. In addition to the Raman spectrum *per se*, however, the required geometrical derivatives are also the ingredients used to compute vibrational contributions to the polarizability itself. Before we attempt to simulated Raman spectra, therefore, it is interesting to assess the performance of the chosen model in reproducing electronic polarizabilities (both static and frequency-dependent) when all relevant contributions are included. The text has been readapted from the original publication.[1]

4.1 Linear and non-linear optical properties of solvated systems

Linear and nonlinear optical properties, especially (hyper)polarizabilities, of molecular systems are of remarkable and increasing interest in a number of research fields, on both a fundamental and a technological level.[94–96] In this context, the role of quantum mechanical approaches for complementing experimental studies is continuously increasing from both the

point of view of the dimensions of the systems amenable to accurate computations, and of the inclusion of dynamic and environmental effects in addition to intrinsic stereo-electronic ones. Even pending further developments for specific shortcomings, last-generation density functionals are providing sufficiently reliable results for the nonlinear properties of isolated molecules at their equilibrium geometries[97] to warrant consideration of additional effects. As a matter of fact, a number of studies have demonstrated the importance of both vibrational and environmental contributions to (hyper)polarizabilities.[77,98–100] These contributions can in many cases be significant and in some circumstances (especially for the static case) even dominate over the electronic equilibrium value of the isolated system (α^{eq}). Among the various terms, the zero-point contribution ($\Delta_{\mathrm{ZP}}\alpha$) arises from harmonic and/or anharmonic nuclear oscillations around the equilibrium geometry. This term is equivalent to vibrational averaging effects on other electronic properties[4,5,29,101] and can be computed once first and second derivatives of polarizability with respect to geometric parameters are available. Next, the pure vibrational contributions (α^{v}), including both harmonic and anharmonic terms, arise from excitations within the vibrational manifold of the electronic ground state, rather than the electronic excited states, as is the case for the electronic contributions to the (hyper)polarizabilities. Depending on the specificity of the system under study and the experimental conditions that one is set to reproduce with the chosen theoretical model, some, or even all, of these effects may be needed to achieve the desired accuracy. Finally, proper treatment of environmental effects, even in the context of continuum methods (i.e. in the absence of specific system-environment interactions) requires implementations going well beyond standard models and including nonequilibrium and local field effects. Following previous work in our group we have now implemented also these terms in the general anharmonic model sketched above. This allows the proper consideration of all the dominant effects and the disentanglement of their relative contribution to the overall experimental outcome. In this first report we will be concerned with polarizabilities (both static and frequency-dependent)

only, whereas hyperpolarizabilities will be dealt with in forthcoming studies. After a short presentation of the essential physical-mathematical background and of implementation and computational details, we will discuss specific examples in order to illustrate the possibilities and the reliability of this computational tool. The general aim is to show that, apart from the specific interest of the studied systems, a robust and user-friendly computational tool is now available for complementing experimental analyses.

4.2 Theory

4.2.1 The molecular polarizability

Whithin the Born-Oppenheimer approximation the molecular polarizability (both static and frequency-dependent) can be written as the sum of three terms:[26,27]

$$\alpha = \alpha^{eq} + \Delta_{\mathrm{ZP}}\alpha + \alpha^{v} \tag{4.1}$$

The first term denotes the electronic polarizability of the molecule at the equilibrium geometry, the second term is its zero-point vibrational correction, and the last term is the pure vibrational polarizability. When computing the two vibrational contributions we assume that only the ground vibrational state is populated. The electronic term, which can be computed by means of response theory with most electronic structure methods, is expected to be the most important of the three, both in the frequency-dependent case and in the static limit. Previous studies however have pointed out that in order to obtain accurate results, the effect of molecular vibrations should not be ignored.[98–100] The two vibrational terms in equation 4.1 are of very different nature. The pure vibrational polarizability can be related to the change of the electric dipole moment as the molecule vibrates, and can be expressed as a sum-over-states:[102,103]

$$\alpha^{v}_{\alpha\beta} = \frac{2}{\hbar}\sum_{w\neq 0}\frac{\omega_{w0}}{\omega^{2}_{w0}-\omega^{2}}\langle 0|\mu_{\alpha}|w\rangle\langle w|\mu_{\beta}|0\rangle \tag{4.2}$$

where μ is the electric dipole moment, ω_{w0} is the difference between the energy of the state w and the ground-state energy, ω is the angular frequency of the electric field, $|0\rangle$ is the vibrational state of the molecule, and the summation runs over all other vibrational states belonging to the same electronic level. It is clear from this expression that, as ω increases, the pure vibrational contribution goes to zero, it is therefore expected to be negligible in the case of light in the UV-visible range of the spectrum. This term can instead be significant in the case of the static polarizability. The zero-point correction to the electronic polarizability stems from the fact that the latter is computed for the molecule at the equilibrium geometry, but even at zero absolute temperature the nuclei cannot be considered fixed. Any electronic property, such as the electronic polarizability, can thus be averaged using the vibrational wavefunction of the system, giving rise to the remaining terms of equation 4.1. Contrary to the pure vibrational term, the vibrational correction can give a significant contribution both in the static and in the frequency-dependent case. The calculation of the vibrational terms requires a model for the potential energy surface (PES) of the system. The harmonic approximation is usually invoked in this case, where the electrostatic potential is expanded up to the second order, giving a description of the molecular vibrations in terms of normal modes. The harmonic approximation however may not be accurate enough to provide an adequate description of the system, and inclusion of anharmonicity effects has been shown to be crucial in the modeling of electronic properties.[4,5,29]

In the case of the static polarizability an additional term is usually included: a static electric field causes molecules with a non-zero dipole moment to partially reorient along the field axis,[104] so a direct experimental measurement of the static polarizability of a system naturally includes a term which depends on the dipole moment of the system and the temperature. This term, denoted in the following by α_μ, is equal to $|\mu|^2/3k_BT$ for a molecular system in the gas phase. This quantity should be added to the computed static polarizability before any meaningful comparison with experimental findings is made.

4.2.2 Anharmonicity effects on the polarizability

In this work we model the anharmonicity of the PES using our implementation[20,21,25,30] of second-order vibrational perturbation theory (VPT2) which is able to provide an accurate description of both anharmonic vibrational energies and wavefunctions. Within the framework of perturbation theory it is also useful to expand electronic properties which depend on the molecular geometry, such as the dipole moment or the electronic polarizability, in a Taylor series around the equilibrium structure and truncate the expansion at the required order. Usually, one only keeps the lowest-order that gives a non-zero contribution if combined with the harmonic vibrational wavefunction. However, if anharmonicity effects are introduced, the effects of the so-called electric anharmonicity (i.e. contributions from higher-order terms in the electronic property expansions) should also be considered. In the case of electronic properties we are considering here, the anharmonic wavefunction obtained via VPT2 can be combined with the Taylor expansions of the electric dipole moment and electronic polarizability to rewrite the previous equations, giving explicit expressions for both the vibrational average and the anharmonic pure vibrational polarizability. The vibrational average results in two terms, the first one accounting for the mechanical anharmonicity, and the second term accounting for the electric anharmonicity. This separation is denoted by the indices in the apex, the first one denoting the level of electric anharmonicity and the second one denoting the level of mechanical anharmonicity:[26,27]

$$\begin{aligned}\Delta_{\mathrm{ZP}}\alpha =& -\frac{\hbar}{4}\sum_a \frac{1}{\omega_a^2}\left(\frac{\partial\alpha}{\partial Q_a}\right)\sum_b \frac{K_{abb}}{\omega_b} + \frac{\hbar}{4}\sum_a \frac{1}{\omega_a}\left(\frac{\partial^2\alpha}{\partial Q_a^2}\right) \\ =& [\alpha]^{0,1} + [\alpha]^{1,0}\end{aligned} \tag{4.3}$$

The pure vibrational terms can be treated in a similar way obtaining explicit formulas that depend on the derivatives of the electric dipole moment, in addition to the cubic and quartic force constants. The total value is separated into a harmonic term and three anharmonic contributions which are distinguished according to their degree of mechanical and

electric anharmonicity:

$$\alpha^v = [\mu^2]^{0,0} + [\mu^2]^{0,2} + [\mu^2]^{1,1} + [\mu^2]^{2,0} \tag{4.4}$$

We compute these terms using the formulas obtained by Bishop et al.[26,27,102,103] albeit with a slightly different expression for the $[\mu^2]^{0,2}$ term, shown in the Appendix, since we found the original expression for this term reported in the literature to be incorrect. Anharmonic calculations tend to be very expensive for medium-large sized systems because they require the evaluation of force constants up to the fourth order, as well as high-order geometrical derivatives of the electronic properties under investigation. If the harmonic frequencies can be computed analytically, all the required anharmonic terms (i.e. all third derivatives and fourth derivatives with up to 3 different indices) can be found by numerical differentiation of lower-order terms by displacing the atoms along each normal mode both in the positive and in the negative directions. This number of separate calculations that must be performed scales with system size, therefore particular care should be taken in the case of larger systems. Fully analytical implementations for the calculation of zero point vibrational corrections to the polarizability have also been proposed.[105–107]

4.2.3 The molecular polarizability of solvated systems

Polarizabilities and hyperpolarizabilities describe a system's response to an external static or dynamic electric field. If the system under consideration is a solution, the mutual interactions between the solvent, solute, and the electromagnetic field, should all be considered in determining the system's response. Even in the absence of an external radiation a solvent induces profound changes in solute molecules: the electron density, ground-state geometry, and conformational distribution are all affected, and these changes are reflected in all molecular properties, including response properties. When considering electric-field induced responses, in

addition to the effect on the solute, the effect of the solvent on the field itself should be considered.[108] The solute's response is caused by the field locally acting on it, which is different than the external field because of the solvent's screening effect. Traditionally the problem is addressed via the Onsager-Lorentz model,[91] which is based on the assumption that the molecule can be treated as a point-like electric dipole at the center of a spherical cavity within a polarizable continuum, the latter representing the solvent. The local field can then be related to the external field through a simple multiplicative factor which only depends on the solvent's static dielectric constant (ε) for static fields ($\vec{E}^{\,\mathrm{loc}}$), and on the solvent's optical dielectric constant ($\varepsilon_{\mathrm{opt}}$) for dynamic fields ($\vec{E}^{\,\mathrm{loc}}_{\omega}$):

$$\vec{E}^{\,\mathrm{loc}} = \frac{\varepsilon + 2}{3}\vec{E}^{\,\mathrm{ext}} \qquad ; \qquad \vec{E}^{\,\mathrm{loc}}_{\omega} = \frac{\varepsilon_{\mathrm{opt}} + 2}{3}\vec{E}^{\,\mathrm{ext}}_{\omega} \tag{4.5}$$

The Onsager-Lorentz model has often been used in reverse, to estimate a molecule's gas-phase polarizability and hyperpolarizabilities from experimental data measured in solution. This model is, however, very crude, as it only reduces the solute's electron density to the sole dipole term, and assumes a spherical cavity regardless of the molecular shape. Notably, the computed factors are the same for every solute as they only depend on the solvent's dielectric properties.

In this work we treat solvation effects by means of the polarizable continuum model (PCM),[35,36] which treats the solvent as a polarizable continuum with given dielectric properties. The molecule, treated quantum-mechanically, is placed inside of a molecule-shaped cavity carved within the polarizable continuum, and a mutual polarization between the solute's electronic density and the dielectric continuum is established. The solvent's polarization affects the solute through appropriate terms that are added to the Hamiltonian, which can be carried over to molecular property calculations, including response properties. PCM, therefore, can treat both the "direct" solvent effect on the electronic density and the "indirect" effect on the molecular geometry. PCM can also be used to integrate local-field effects in the calculation in a more accurate way than the

Onsager-Lorentz model, by introducing the concept of "effective" molecular response properties, which directly describe the response of the solute to the external field in the liquid.[109] As in the Onsager-Lorentz model, local field effects on the static (hyper)polarizabilities are computed using the solvent's static dielectric constant, whereas their dynamical counterparts are computed using the optical dielectric constant (i.e. the square of the refractive index). Note that the sum-over-state expression for the polarization P in the case of a general first-order process can be written as follows:[110]

$$P_\omega = -\frac{1}{\hbar}\sum_{m\neq n}\left(\frac{\langle n|\hat{\mu}|m\rangle\langle m|\hat{V}_\omega|n\rangle}{\omega_{mn}-\omega}+\frac{\langle n|\hat{V}_\omega|m\rangle\langle m|\hat{\mu}|n\rangle}{\omega^*_{mn}+\omega}\right) \tag{4.6}$$

In the case of the electronic polarizability of a system in the gas phase we have $\hat{V}_\omega = -\vec{\mu}\cdot\vec{E}_\omega$. In the condensed phase we should use the local field $\vec{E}^{\,\mathrm{loc}}$ instead of the external field. Alternatively, as already mentioned above, we may consider the external field acting on an effective dipole moment $\mu^{\,\mathrm{eff}}$ which, in the PCM framework, can be easily computed as a sum of the dipole moment of the solvated molecule and a contribution due to the charge density induced by the molecule on the cavity surface. The effective dipole moment replaces the molecular dipole moment in the $\hat{V}_\omega$ term only, therefore calculations including local-field effects must be done with care, using the two different dipole moments where appropriate.[92]

In the case of response properties induced by time-dependent fields, additional solvent effects, related to the dynamical aspects of solvation, should be considered. Dynamical polarizabilities and hyperpolarizabilities describe a system response to oscillating fields, usually in the visible range of the spectrum. The solute's electronic density evolves in time according to the characteristic time-scale of the perturbation, and while some degrees of freedom of the solvent are able to instantaneously rearrange to the new solute electronic density, others remain static, entering a nonequilibrium configuration. For visible light, it can be assumed that only the electrons of the solvent molecules will be able to rearrange themselves to the oscil-

lating solute electronic density, while the nuclei will remain fixed. This effect is included in the calculation of the electronic component of optical rotation within the PCM framework by separating the solvent polarization into two different contributions,[89] one accounting for the "fast" degrees of freedom of the solvent, and one induced by the "slow" degrees of freedom, responsible for the nonequilibrium effect. This electronic nonequilibrium effect does not apply to the case of static polarizabilities.

4.2.4 Combining solvation and vibrational effects

Solvent effects described so far apply to the calculation of the electronic polarizability, however, the focus of this work is the modeling of vibrational effects on polarizabilities of solvated systems. The presence of a solvent alters the PES of the solute molecules, with repercussions on all vibrational properties, including vibrational frequencies,[111,112] infra-red (IR) and vibrational circular dichroism (VCD) spectroscopic intensities,[28,31] and, of course, pure vibrational components and vibrational averages of electronic properties. PCM can be effectively used to include these effects in ab-initio calculations, however, special care should be taken when considering the appropriate solvation regime to be adopted. The solute's vibrational motion causes an additional nonequilibrium polarization in the solvent because its translational and rotational degrees of freedom cannot evolve within the time-scale characteristic of a molecular vibration. As in the case of electronic nonequilibrium, in PCM a separate set of polarization charges can be defined to account for the nonequilibrium polarization. The free-energy of the system can thus be rewritten and differentiated to yield the nonequilibrium vibrational wavefunction and vibrational frequencies. This treatment can also be extended to the calculation of the anharmonic force field, and to the geometrical derivatives of all molecular properties. In the case of (hyper)polarizabilities we require the property first and diagonal second derivatives with respect to the normal modes to compute the vibrational correction, and also the derivatives of the dipole moment to compute the pure vibrational contributions. Note that all quantities

are computed with the inclusion of local field effects and, in the case of dynamical (hyper)polarizabilities, electronic nonequilibrium effects. For example, the harmonic contribution to the pure vibrational polarizability becomes:[77]

$$[\mu^2]^{0,0}_{\omega} = \sum_a \frac{\partial \mu_\alpha}{\partial \bar{Q}_a} \frac{\partial \mu^{\text{eff}}_\beta}{\partial \bar{Q}_a} \bar{\lambda}_a \tag{4.7}$$

Where the summation runs over all normal modes, $\lambda_a = (\omega_a^2 - \omega^2)^{-1}$, and all quantities bearing an over-line are computed in the vibrational nonequilibrium regime. Anharmonic contributions and the zero point correction can also be treated in a similar way.

This approach yields physically consistent quantities that can be directly compared with experimental data, which no longer need to be empirically corrected to estimate the solvent's contributions.

4.3 Computational details

All calculations were performed using a locally modified version of the Gaussian09 quantum chemistry suite of programs.[113] The CAM-B3LYP[114] functional was used for all systems since it has been reported to yield reliable results for both the electronic and pure vibrational polarizability.[97,115,116] Different functionals were also tested, including B3LYP,[117,118] M06-2X,[119] PBE0,[120] and ωB97X,[121] with consistent results, reported in the Appendix, showing the computed property to be rather robust with respect to the change of functional, especially for the long-range corrected CAM-B3LYP and ωB97X, which are particularly appropriate for the push-pull systems here analyzed.

The considered systems are shown in figures 4.1 and 4.3. For all calculations concerning pNA and dNA we used the aug-cc-pVDZ[122] basis set, whereas we employed the 6-31+G* basis set for DPDCP and the bichromophoric system in figure 4.3. Solvent effects were accounted for using PCM,[35,36] with the addition of local field and nonequilibrium effects. Molecular cavities were built using a set of interlocking spheres centered on the atoms, with radii according to the Gaussian09 defaults. The solvents'

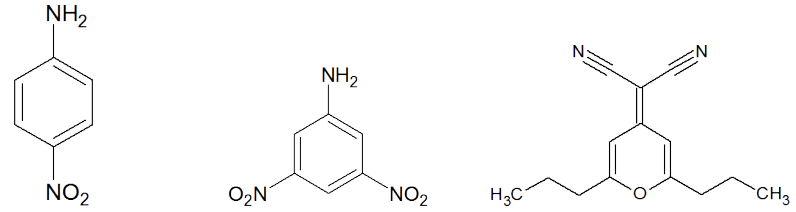

(a) pNA **(b)** dNA **(c)** DPDCP

Figure 4.1: Structures of the first three systems studied.

static and optical dielectric constants used are $\varepsilon = 2.27$ and $\varepsilon_{\text{opt}} = 2.25$ for benzene, $\varepsilon = 2.23$ and $\varepsilon_{\text{opt}} = 2.13$ for CCl_4, and $\varepsilon_0 = 2.21$ and $\varepsilon_{\text{opt}} = 2.02$ for 1,4-dioxane. In the following tables we report the isotropic polarizabilities (the trace of the polarizability tensor divided by 3) α_{is}, as well as the longitudinal component (along the molecular axis) α_{zz}. All polarizabilities are reported in $\text{cm}^3\,\text{mol}^{-1}$, and all solution values include local field effects and are computed in the vibrational nonequilibrium regime, unless otherwise stated.

4.4 Numerical results

Para-nitroaniline (pNA, figure 4.1a) is a prototypical push-pull system whose linear and nonlinear optical properties have received much attention in the literature, both theoretically and experimentally, and previous results allow us to test the model and make useful comparisons.[123–129] We optimized the geometry of the molecule in the C_{2v} symmetry. This geometry however results in a vibrational mode with an imaginary frequency with modulus 238 cm^{-1}, meaning it is actually a saddle point. The incriminated mode is the umbrella motion of the aminic group, so the lowest-energy geometry would have a C_s symmetry and a pyramidalized NH_2 group. We computed the energy profile for the umbrella motion and found that the energy barrier is very low (about 50 cm^{-1}), too low to support a single vibrational mode. At the present time we lack a rigorous treatment for double-well potentials, though some approaches have

been proposed,[130–132] therefore we preferred to perform all calculations on the C_{2v} structure, which is surely more representative of than the C_s one, and discard the contribution of the imaginary frequency mode to the pure vibrational and zero-point contributions. Figure 4.2 shows the contribution of each normal mode (except the imaginary frequency one) to the zero-point and harmonic pure vibrational static polarizability of pNA in vacuo. It must be emphasized that the two contributions are unrelated since the first is computed from the polarizability derivatives while the second depends on the dipole derivatives. For a C_{2v} molecule such as pNA this implies that they obey different symmetry rules, e.g. a_2 modes give a vanishing pure vibrational polarizability but they contribute to the $[\alpha]^{1,0}$ term in the zero-point polarizability, while the $[\alpha]^{0,1}$ term originates solely from the total symmetric modes. The greatest contribution to the pure vibrational polarizability comes from mode 30 (a symmetric N-O stretching), followed by modes 25 and 36, which are symmetric bending motions of the hydrogen atoms (see the Appendix at the end of this chapter for a graphical representation of the modes mentioned in the article), while modes 19 and 30 contribute the most to the zero-point polarizability. While some modes give particularly high contributions, it is not possible to discard some of them *a priori* with the aim of reducing the computational cost, as the contributions from other modes add up to give non-negligible values. A similar conclusion was previously reached in the case of different molecular properties, including magnetic and mixed electric-magnetic properties.[4,5]

Table 4.1 reports the computed static polarizability of pNA in the gas phase and in 1,4-dioxane solution. To better decouple the different solvation effects considered here we also report the values computed in a vibrational equilibrium regime, along the vibrational nonequilibrium values computed with and without the inclusion of cavity field effects. Solvent effects cause a significant change to the computed polarizability at both the electronic and vibrational level, with some of the computed components of the pure vibrational contribution even showing a change of sign, which is particularly noticeable in the case of $[\mu^2]^{0,2}_{zz}$, the term that

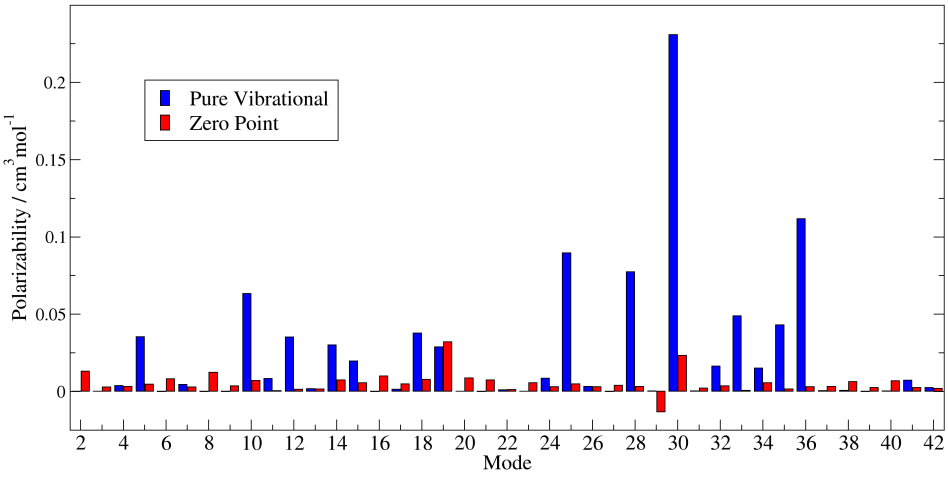

Figure 4.2: Contribution of each normal mode to the zero-point (red) and harmonic pure vibrational (blue) static polarizability of pNA in vacuo.

originates from the mechanical anharmonicity. Switching to a vibrational nonequilibrium regime causes a change in all computed contributions; the electronic component changes because of the slight change in equilibrium geometry (which is reoptimized with a fixed PCM cavity), and a much more significant effect is observed in the case of the pure vibrational part, particularly for the term which includes mechanical anharmonicity to second order. Overall the vibrational nonequilibrium effect does not cause significant changes to the computed polarizability in this particular case, owing to the fact that the chosen solvent's static and optical dielectric constants are very similar ($\varepsilon_0 = 2.21$ and $\varepsilon_\infty = 2.02$), however this might not hold for different systems or different solvents: we performed a test calculation on the same molecule in acetonitrile ($\varepsilon_0 = 35.69$ and $\varepsilon_\infty = 1.81$) and obtained that the pure vibrational contribution changes by 8% when going from vibrational equilibrium to nonequilibrium (data reported in the Appendix at the end of the chapter). A much greater change is observed when local field effects are included in the calculation. Even though 1,4-dioxane doesn't have a particularly high polarity it still perturbs the field experienced by the system quite significantly, affecting all contributions to the polarizability.

Overall, the vibrational contributions account for about 15% of the electronic polarizability polarizability, with the greatest contribution originating from the harmonic pure vibrational term. We also obtain an orientational contribution (originating from the non-zero dipole moment) of 401.2 $cm^3\,mol^{-1}$, which makes the total computed static polarizability equal to 416.0 $cm^3\,mol^{-1}$. This is to be compared with the value of 404 $\pm$ 6 $cm^3\,mol^{-1}$ measured by Wortmann et al.[133] which means that there is a mere 3% discrepancy between theory and experiment. Of course, in this case the greatest contribution is by far the orientational one, which only depends on the dipole moment, so a more meaningful comparison should be done when the former contribution is absent. We therefore computed the frequency-dependent polarizability at 589 nm, in vacuo and in solution (table 4.2). We do not report the pure vibrational component because it is negligible for the considered wavelength. The computed values are only slightly different than the static ones, and solvent effects remain very relevant, leading to an increase in the computed polarizability, like in the static case. Vibrational nonequilibrium only causes very slight changes on the computed values, while local field effects, computed in this case using the solvent's optical dielectric constant, significantly affect the electronic part.

From the same paper by Wortmann et al.[133] we find that the experimental value is 14.1 $\pm$ 0.4 $cm^3\,mol^{-1}$, which happens to be exactly the same as the total computed value (14.08 $cm^3\,mol^{-1}$), confirming the validity of our methodology.

The second system we studied is 3,5-dinitroaniline (dNA, figure 4.1b) in gas phase and 1,4-dioxane solution. dNA has a similar structure to pNA and analogous push-pull properties. As in the case of pNA, the equilibrium structure of dNA in both the gas phase and in solution is predicted to be non-planar because of the pyramidalized aminic group. As for pNA, we perform all calculations on the molecule optimized with a C_{2v} geometry and discard the mode with imaginary frequency in the calculation of the pure vibrational components of the polarizability and of the vibrational averaging.

Table 4.1: Static polarizability of pNA in vacuo and 1,4-dioxane solution. The solution values are shown in the vibrational equilibrium regime (sol, vib eq), vibrational nonequilibrium (sol, vib neq), and vibrational nonequilibrium with the addition of local field effects (sol, vib neq + lf).

		α^{eq}	$[\mu^2]^{0,0}$	$[\mu^2]^{2,0}$	$[\mu^2]^{1,1}$	$[\mu^2]^{0,2}$
gas	α_{zz}	13.650	1.861	0.011	-0.057	0.942
	α_{is}	9.206	0.931	-0.001	-0.024	0.112
sol, vib eq	α_{zz}	16.597	3.063	0.003	-0.017	-0.552
	α_{is}	10.833	1.425	-0.003	-0.006	-0.392
sol, vib neq	α_{zz}	16.604	3.001	-0.001	-0.016	-0.212
	α_{is}	10.837	1.430	-0.005	-0.007	0.041
sol, vib neq + lf	α_{zz}	18.342	3.285	-0.001	-0.047	-0.201
	α_{is}	12.781	1.647	-0.002	-0.021	0.039
		$[\alpha]^{1,0}$	$[\alpha]^{0,1}$	α_μ	α_{tot}	α_{exp}[133]
gas	α_{zz}	0.197	0.094	266.2	282.9	-
	α_{is}	0.149	0.061	266.2	276.6	-
sol, vib eq	α_{zz}	0.282	0.131	362.3	381.8	-
	α_{is}	0.199	0.079	362.3	374.4	-
sol, vib neq	α_{zz}	0.256	0.140	362.1	381.9	-
	α_{is}	0.193	0.085	362.1	374.7	-
sol, vib neq + lf	α_{zz}	0.281	0.156	401.2	423.0	-
	α_{is}	0.224	0.099	401.2	416.0	404±6

Table 4.2: Dynamic polarizability of pNA in vacuo and 1,4-dioxane solution computed for a 589 nm wavelength. The solution values are shown in the vibrational equilibrium regime (sol, vib eq), vibrational nonequilibrium (sol, vib neq), and vibrational nonequilibrium with the addition of local field effects (sol, vib neq + lf).

		α_ω^{eq}	$[\alpha]_\omega^{1,0}$	$[\alpha]_\omega^{0,1}$	α_{tot}	α_{exp}[133]
gas	α_{zz}	15.29	0.28	0.12	15.69	-
	α_{is}	9.91	0.19	0.07	10.17	-
sol, vib eq	α_{zz}	19.09	0.45	0.19	19.73	-
	α_{is}	11.80	0.27	0.10	12.17	-
sol, vib neq	α_{zz}	19.10	0.41	0.20	19.71	-
	α_{is}	11.81	0.25	0.11	12.17	-
sol, vib neq + lf	α_{zz}	20.91	0.45	0.22	21.58	-
	α_{is}	13.67	0.29	0.12	14.08	14.1±0.4

Table 4.3 reports all the contributions to the longitudinal (along the molecular axis) and isotropic static polarizability. The vibrational correction $\Delta_{\mathrm{ZP}}\alpha$ to the isotropic polarizability is about 2% of the corresponding electronic value, with the greatest contribution coming from $[\alpha]^{1,0}$, which accounts for the electric anharmonicity of the electronic polarizability. An opposite conclusion can be reached in the case of the pure vibrational component, whose most important term is $[\mu^2]^{0,2}$, which is entirely due to the anharmonicity of the PES. This is not surprising as the pure vibrational component is computed from the electric dipole derivatives rather than the polarizability derivatives, and the former may have a less pronounced dependence on the molecular geometry compared to the latter. In addition, the vibrational correction $[\alpha]^{0,1}$ depends on the mechanical anharmonicity only through the semi-diagonal cubic force constants K_{abb} whereas the pure vibrational component $[\mu^2]^{0,2}$ requires all third derivatives as well as the semi-diagonal fourth derivatives of the electronic energy (the complete expression of the $[\mu^2]^{0,2}$ term can be found in the Appendix). Introducing solvent effects has a dramatic effect on all quantities, with a 40% increase in the electronic isotropic value and the vibrational correction, and an even greater effect on the pure vibrational part, which becomes very considerable with respect to the electronic polarizability, highlighting the usefulness of including both vibrational and environmental effects in a coherent manner.

Table 4.3: Static polarizability of dNA in vacuo and 1,4-dioxane solution.

		α^{eq}	$[\mu^2]^{0,0}$	$[\mu^2]^{2,0}$	$[\mu^2]^{1,1}$	$[\mu^2]^{0,2}$
gas	α_{zz}	12.970	1.513	-0.004	-0.008	0.584
	α_{is}	10.420	1.555	0.004	-0.006	0.656
sol	α_{zz}	17.335	2.406	0.009	-0.008	1.000
	α_{is}	14.211	1.872	-0.007	-0.007	2.005
		$[\alpha]^{1,0}$	$[\alpha]^{0,1}$	α_{μ}	α_{tot}	α_{exp} [133]
gas	α_{zz}	0.185	0.088	202.0	217.3	-
	α_{is}	0.160	0.066	202.0	214.9	-
sol	α_{zz}	0.268	0.130	300.4	321.6	-
	α_{is}	0.244	0.097	300.4	318.8	330±6

Table 4.4 reports the electronic and vibrational corrections to the dynamic polarizability computed at the sodium-D wavelength (589 nm). We only show the vibrational correction in this case because the pure vibrational term is negligibly small for this wavelength. The results for the dynamic polarizability mirror the static ones: solvent effects produce an increase in both the electronic polarizability and the vibrational corrections, and for the latter the electric anharmonicity is the dominant effect.

The static and dynamic polarizability of dNA in 1,4-dioxane has also been studied experimentally by Wortmann et al,[133] who obtained values of 330 ± 6 and 15.5 ± 0.1 cm^3 mol^{-1} for α and α_ω, respectively. The static value includes the orientational contribution discussed above, which we also computed obtaining a value of 300.4 cm^3 mol^{-1}. By summing all contributions we obtain total calculated values of 319 and 15.3 cm^3 mol^{-1} for α and α_ω, respectively. The experimental values are very well reproduced in both cases, confirming the validity of our approach.

Table 4.4: Dynamic polarizability of dNA in vacuo and 1,4-dioxane solution computed for a 589 nm wavelength.

		α_ω^{eq}	$[\alpha]_\omega^{1,0}$	$[\alpha]_\omega^{0,1}$	α_{tot}	α_{exp}[133]
gas	α_{zz}	13.75	0.23	0.10	14.08	-
	α_{is}	11.07	0.21	0.07	11.35	-
sol	α_{zz}	18.12	0.35	0.15	18.61	-
	α_{is}	14.88	0.32	0.11	15.32	15.5±0.1

The next system we analyze is 2,6-di-n-propyl-4H-pyran-4-ylidenemalononitrile (DPDCP), shown in figure 4.1c, in CCl_4 solution. In this case we only limit ourselves to the dynamic polarizability computed at 633 nm, for which experimental measurements exist.[134] Results are summarized in table 4.5. The discussion is very similar as in the two previous cases: the electric anharmonicity gives again the greatest contribution to the zero-point polarizability, whose inclusion shifts the computed value in the right direction with respect to the experimental measurement.

Table 4.5: Dynamic polarizability of DPDCP in CCl_4 solution computed for a 633 nm wavelength.

	α_ω^{eq}	$[\alpha]_\omega^{1,0}$	$[\alpha]_\omega^{0,1}$	α_{tot}	α_{exp} [134]
α_{zz}	33.70	1.64	0.01	35.35	-
α_{is}	23.67	1.36	0.01	25.04	27.3

4.4.1 Bichromophoric system

After testing the method we moved to the larger system shown in figure 4.3 (1,4-bis(4'-dimethylamino-3',5'-dicyanophenil)bicyclo[2,2,2]octane) in benzene solution. The molecule is composed of two aromatic chromophores bridged by an aliphatic bicyclooctane structure. We computed the static and dynamic polarizability of the system as a whole (A), and of the chromophore (B) and bridging structure (C) alone, to test whether the polarizability of the whole structure might be the sum of the three independent terms. Table 4.6 shows both the static and dynamic electronic polarizabilities of the molecule (the latter computed at a 1086 nm wavelength), as well as the respective harmonic pure vibrational contributions.

In the case of the static polarizability, the harmonic pure vibrational contribution represents about 8% of the electronic value, whereas its dynamic counterpart appears to be negligible, for both the whole molecule and its structural building blocks. The results also suggest that the purely electronic polarizability can be safely computed by summing the contributions three separate pieces (2B+C). The total electronic polarizability obtained this way has only a 3% error with respect to the one computed for the whole system. This is not surprising as molecular polarizabilities can sometimes be estimated by summing atomic and/or functional groups contributions.[135] Unfortunately, the same cannot be said for the pure vibrational polarizability: the values obtained for the A structure differ significantly from the 2B+C ones. This is expected as the vibrational modes of the whole molecule tend to be highly delocalized and, owing to its C_2 symmetry, they often appear as symmetric and antisymmetric combinations of local vibrations.

The dynamic polarizability of molecule A in benzene has been mea-

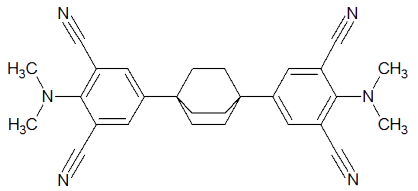

(a) A

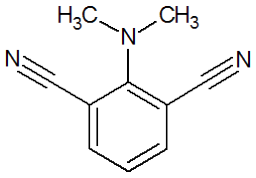

(b) B

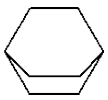

(c) C

Figure 4.3: Structure of the bichromophoric system and its constituent parts studied.

sured by Liptay et al.[136] who report a value of 560 ± 6 $cm^3\,mol^{-1}$. This is one order of magnitude greater than the value we computed. Given the accuracy of the results obtained for the other systems described here with respect to their experimental counterparts we believe this discrepancy may be due to an error in the experimental measurement. This result may stimulate new experimental studies on this system.

Table 4.6: Static and dynamic polarizability of the bichromophoric system in benzene solution.

		α^{eq}	$[\mu^2]^{0,0}$	α^{eq}_{ω}	$[\mu^2]^{0,0}_{\omega}$
A	α_{zz}	52.55	4.25	53.67	-0.08
	α_{is}	43.97	3.34	44.64	-0.04
B	α_{zz}	20.62	1.29	20.83	-0.01
	α_{is}	16.31	2.00	16.60	-0.02
C	α_{zz}	10.17	0.12	10.22	-0.01
	α_{is}	10.17	0.11	10.22	-0.01
2B+C	α_{zz}	51.41	2.70	51.88	-0.03
	α_{is}	42.79	4.11	43.42	-0.05

4.5 Conclusions and perspectives

We have presented a methodology for computing static and frequency-dependent polarizabilities of molecular systems in the condensed phase that takes into account both vibrational and electronic effects. All contributions to the computed polarizability, i.e. the orientational component, the purely electronic contribution, and the zero-point and pure vibrational corrections, were computed with the inclusion of solvent effects modeled via PCM. Vibrational effects were computed using an anharmonic PES via perturbation theory, and the geometrical dependence of the electronic properties under consideration, be it the polarizability or the dipole moment, were also taken into account by means of Taylor expansions truncated at the appropriate order. We took particular care when including electronic and/or vibrational nonequilibrium effects on the different terms that constitute the computed physical quantity, so the purely electronic component and its zero-point correction were calculated under the electronic nonequilibrium solvation regime, while vibrational nonequilibrium effects were included in the latter and in the pure vibrational polarizability, both at the harmonic and anharmonic levels. Local field effects were also included in all contributions,[77] as it has been shown that they may lead to substantial changes to the computed values. The ability of this model to introduce non-specific solvent effects on all components of the computed polarizability should discourage the use of the popular, albeit very approximate, Onsager-Lorentz model to estimate the cavity field and reaction field factors and obtain the gas-phase value from its solution one and vice-versa. Specific solvation effects can be easily introduced by adding explicit solvent molecules to the portion of the system treated quantum-mechanically, or through mixed quantum-mechanical/classical models such as the QM/FQ/PCM model we have recently implemented.[59–61] This model provides a consistent description of the electronic properties of molecular systems in solution and yields computed values that can be directly compared with experimental measurements, as exemplified by the accuracy of the computed values

presented here. We believe these results show that while the use of more accurate (and expensive) electronic structure methods in conjunction with larger basis sets can surely increase the accuracy of the purely electronic component, this should not come at the cost of forsaking the other contributions.

4.6 Appendix

4.6.1 Anharmonic pure polarizability expression

We used the following expression for the $[\mu^2]^{0,2}$ term in the pure vibrational polarizability (i.e. the one due to the mechanical anharmonicity only):

$$
\begin{aligned}
[\mu^2]^{0,2} = &-\frac{\hbar}{8}\sum \hat{P}_{\alpha\beta}\sum_{ab}\frac{1}{\omega_a}\Bigg\{\frac{1}{2}F_{aabb}\frac{\partial\mu_\alpha}{\partial Q_b}\frac{\partial\mu_\beta}{\partial Q_b}\frac{\lambda_b}{\omega_b^2}+\sum_{c\neq b}F_{aabc}\frac{\partial\mu_\alpha}{\partial Q_b}\frac{\partial\mu_\beta}{\partial Q_c}\lambda_b\lambda_c+\\
&-\sum_c\Bigg[\frac{1}{2}F_{aab}F_{bcc}\frac{\partial\mu_\alpha}{\partial Q_c}\frac{\partial\mu_\beta}{\partial Q_c}\frac{\lambda_c}{\omega_b^2\omega_c^2}+F_{abc}F_{abc}\frac{\partial\mu_\alpha}{\partial Q_c}\frac{\partial\mu_\beta}{\partial Q_c}\lambda_{ab}\lambda_c\frac{(\omega_a+\omega_b)^2-2\omega_c^2-\omega^2}{(\omega_a+\omega_b)^2-\omega_c^2}+\\
&+\sum_{d\neq c}\left(F_{aab}F_{bcd}\frac{\partial\mu_\alpha}{\partial Q_c}\frac{\partial\mu_\beta}{\partial Q_d}\frac{\lambda_c\lambda_d}{\omega_b^2}+2F_{abc}F_{abd}\frac{\partial\mu_\alpha}{\partial Q_c}\frac{\partial\mu_\beta}{\partial Q_d}\lambda_{ab}\lambda_c\lambda_d\right)\Bigg]\Bigg\}
\end{aligned}
$$

where F_{abc} and F_{abcd} are the cubic and quartic force constants, ω_a denotes the angular harmonic frequency of normal mode a, ω is the angular frequency of the applied electric field, and the operator $\sum \hat{P}_{\alpha\beta}$ permutes the two dipole components ($\sum \hat{P}_{\alpha\beta}f(\mu_\alpha,\mu_\beta) = f(\mu_\alpha,\mu_\beta)+f(\mu_\beta,\mu_\alpha)$). We also use the quantities $\lambda_{ab} = ((\omega_a+\omega_b)^2-\omega^2)^{-1}$ and $\lambda_c = (\omega_c^2-\omega^2)^{-1}$. All derivatives are understood to be performed with respect to the mass-weighted normal modes at the equilibrium geometry.

4.6.2 Polarizability computed with different functionals

In table 4.7 we report the electronic static and dynamic (computed at 589 nm) polarizabilities (in $\mathrm{cm}^3\,\mathrm{mol}^{-1}$) of para-nitroaniline (pNA) in vacuo and 1,4-dioxane, computed with different functionals with the aug-cc-pVDZ basis set. The bottom two rows show the ratios between the solvent and gas phase values. The molecular geometry was reoptimized with

each functional before computing the polarizabilities. CAM-B3LYP and ωB97X are both range corrected functionals which are especially suitable for the push-pull systems considered in this work, and give rather similar results both in vacuo and in solution, though the ωB97X polarizabilities are consistently lower than the CAM-B3LYP ones. While the accord with experimental findings, reported in section 4 of the manuscript, would certainly change if ωB97X were used instead of CAM-B3LYP (e.g. the accord with the experimental dynamic polarizability of pNA would most likely decrease, while the accord in the case of the static value, which is overestimated by CAM-B3LYP, could very well increase) we believe that the relative importance of all the vibrational and solvation effects considered would likely be unaltered. M06-2X yields results which are very similar to the ωB97X ones, while PBE0 and B3LYP, which are not long-range corrected functionals, give greater values for both the static and dynamic polarizability. Note however that the ratio between the solvent and gas phase values is very similar with all functionals.

Table 4.7: Longitudinal and isotropic components of the static and dynamic (at 589nm) polarizabilities of para-nitroaniline in vacuo and 1,4-dioxane, computed with different functionals with the aug-cc-pVDZ basis set. The bottom two rows show the ratios between the solvent and gas phase values.

		CAM-B3LYP		ωB97X		M06-2X		PBE0		B3LYP	
		α^{eq}	α_ω^{eq}	α^{eq}	α_ω^{eq}	α^{eq}	α_ω^{eq}	α^{eq}	α_ω^{eq}	α^{eq}	α_ω^{eq}
gas	α_{zz}	13.65	15.29	13.22	14.58	13.38	14.87	14.16	16.14	14.63	16.98
	α_{is}	9.21	9.92	9.07	9.68	9.09	9.74	9.37	10.19	9.60	10.56
sol	α_{zz}	16.57	19.05	15.88	17.83	16.16	18.35	17.31	20.39	18.03	21.83
	α_{is}	10.82	11.78	10.60	11.39	10.65	11.52	11.06	12.23	11.39	12.81
sol/gas	α_{zz}	1.21	1.25	1.20	1.22	1.21	1.23	1.22	1.26	1.23	1.29
	α_{is}	1.18	1.19	1.17	1.18	1.17	1.18	1.18	1.20	1.19	1.21

4.6.3 Polarizability of pNA in a highly polar solvent

Table 4.8 reports the electronic and harmonic pure vibrational static and dynamic (at 589 nm wavelength, and denoted by a subscript ω) polarizability of pNA in acetonitrile (whose static and optical dielectric constants are $\varepsilon_0 = 35.69$ and $\varepsilon_\infty = 1.81$, respectively). The results show that the

vibrational nonequilibrium has a much greater effect on the pure vibrational component when compared with the analogous values obtained for 1,4-dioxane reported in the paper, owing to the much greater difference between the static and optical dielectric constants of acetonitrile. The purely electronic component changes negligibly between the two solvation regimes since its variation is only caused by a very slight change in the equilibrium geometry.

Table 4.8: Static and dynamic (at 589 nm) polarizability of pNA in acetonitrile solution computed at the CAM-B3LYP/aug-cc-pVDZ level of theory. The solution values are shown in the vibrational equilibrium (vib eq), and vibrational nonequilibrium (vib neq) solvation regimes.

		α^{eq}	$[\mu^2]^{0,0}$	α_ω^{eq}	$[\mu^2]_\omega^{0,0}$
vib eq	α_{zz}	21.53	6.08	20.74	-0.04
	α_{is}	13.53	2.67	12.23	-0.02
vib neq	α_{zz}	21.56	4.62	20.72	-0.03
	α_{is}	13.54	2.46	12.21	-0.01

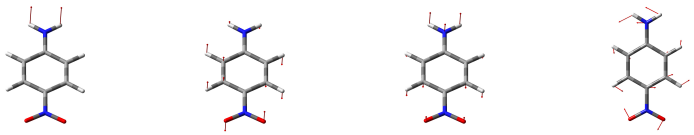

(a) Mode 1 (b_1) **(b)** Mode 2 (a_2) **(c)** Mode 3 (b_1) **(d)** Mode 4 (b_2)

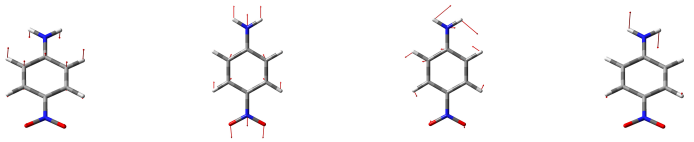

(e) Mode 5 (b_1) **(f)** Mode 6 (a_1) **(g)** Mode 7 (b_2) **(h)** Mode 8 (a_2)

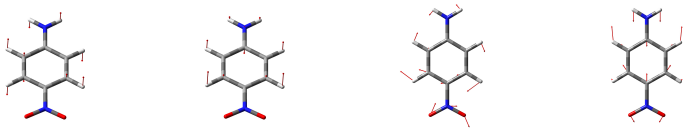

(i) Mode 9 (a_2) **(j)** Mode 10 (b_1)**(k)** Mode 11 (b_2)**(l)** Mode 12 (a_1)

(m) Mode 13**(n)** Mode 14 (b_1)**(o)** Mode 15 (b_1)**(p)** Mode 16 (a_2) (b_2)

(q) Mode 17 (a_1)**(r)** Mode 18 (b_1)**(s)** Mode 19 (a_1)**(t)** Mode 20 (b_1)

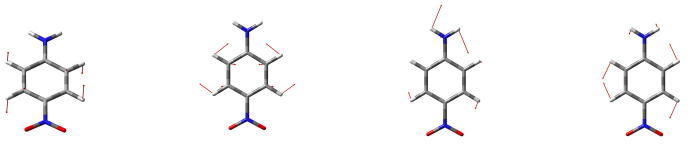

(u) Mode 21 (a_2)**(v)** Mode 22 (a_1)**(w)** Mode 23 (b_2)**(x)** Mode 24 (b_2)

Figure 4.4: Normal modes of pNA. The symmetry of each mode is reported in parenthesis.

(a) Mode 25 (a_1)**(b)** Mode 26 (a_1)**(c)** Mode 27 (b_2)**(d)** Mode 28 (a_1)

(e) Mode 29 (b_2)**(f)** Mode 30 (a_1)**(g)** Mode 31 (b_2)**(h)** Mode 32 (a_1)

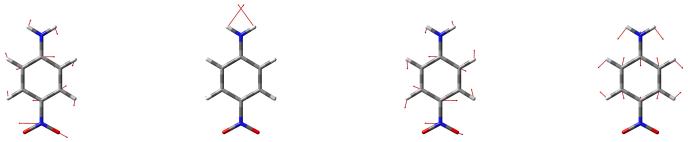

(i) Mode 33 (b_2)**(j)** Mode 34 (a_1)**(k)** Mode 35 (b_2)**(l)** Mode 36 (a_1)

(m) Mode 37**(n)** Mode 38 (a_1)**(o)** Mode 39 (b_2)**(p)** Mode 40 (a_1) (b_2)

(q) Mode 41 (a_1)**(r)** Mode 42 (b_2)

Figure 4.5: Normal modes of pNA (cont.) The symmetry of each mode is reported in parenthesis.

Chapter 5

Vibrational spectroscopies

In this chapter we present some applications of the methods previously introduced in the case of vibrational spectroscopies, i.e. Infra-Red (IR), Vibrational Circular Dichrosm (VCD), and Raman. The emphasis is given to the coupling of an anharmonic description of the ground state Potential Energy Surface (PES) and property surfaces to a continuum description of the solvent, with all relevant effects included, as detailed in the preceding chapters. Most of the text has bee readapted from the original publication.[2]

5.1 Introduction

The space and time scales for systems and processes of current biological and/or technological interest (e.g. nanotechnologies, nanobiomedicine, etc.) are approaching more and more the molecular level, and can be most effectively probed by techniques related to molecular spectroscopy. The diverse spectroscopic techniques available today provide a wealth of information about widely different aspects of the molecular systems for strongly different environments. The most powerful approaches involve the integration of several spectroscopic techniques combined together and further supported by reliable computational tools. As a matter of fact, spectroscopic features are only indirectly related to structural and dy-

namical characteristics of the systems under study, so that interpretation of the experimental outcome in terms of stereo-electronic effects and of their tuning by dynamics and changing environment is seldom straightforward. In this context, computational spectroscopy represents an increasingly indispensable aid for unraveling the various contributions to the spectroscopic signal, allowing a deeper understanding of the underlying elementary effects.[137–139] The predictive and interpretative power of computational spectroscopy is ever increasing from small rigid molecules in gas phase to large flexible systems in condensed phases thanks in part to the development of so-called virtual spectrometers, which make this kind of studies accessible to non-specialists via their inclusion on robust and user-friendly computational packages.[140] In recent years, we have been deeply involved in the development of a multifrequency virtual spectrometer, which can be tuned to provide more and more reliable vibrational, electronic, and magnetic spectra.[29,101,141,142] Here we will be concerned with our recent activity regarding the support of vibrational spectroscopies. Rather than providing a lengthy theoretical development and a number of more or less interesting applications, we decided to concentrate on a multispectroscopic approach to a two prototypical systems, namely (S)-nicotine and *p*-nitroaniline (pNA) (see figure 5.1). We first computed the optical rotation and the infra-red (IR) Vibrational and Circular Dichroism (VCD) spectra of nicotine, we then computed the frequency dependent Raman spectra of pNA. Because of its well-known biological activity, (S)-nicotine has been the subject of several studies aimed at providing better insights into its structure and properties.[143–146] To the best of our knowledge, however, nicotine lacks a thorough computational study in spite of the availability of nuclear magnetic resonance (NMR)[147], circular dichroism (CD),[148–150] Raman and ROA spectra.[151] Taking also into account that nicotine is a medium-size semirigid molecule, soluble in a variety of environments, it represents indeed an ideal benchmark for our developments. The choice of pNA for the calculation of Raman spectra was instead motivated by the availability of experimental spectra measured in different solvents with varying polarity, allowing us to better assess the perfor-

mance of the chosen solvation model in conjunction with the anharmonic calculation of both frequencies and intensities.

5.2 Spectroscopic Properties of Solvated Systems

In this work we used the Polarizable Continuum Model (PCM)[35,36] to couple solvent effects to the quantum mechanical (QM) description of the spectroscopic properties both at the purely electronic and vibrational levels. The PCM approach gives an accurate description of the electrostatic component of solvation at a very low computational cost, and can be coupled to a variety of QM methods, extended to treat spectroscopic and response properties[152] and to surfaces,[153] interfaces,[154] metal nanoparticles,[73] and polymeric materials.[155] In PCM, the molecule is placed in a cavity carved within a dielectric continuum representing the solvent. The dielectric properties of the polarizable continuum, i.e. its static and optical dielectric constants, are set equal to those of the chosen solvent. The presence of the solute induces a charge density on the cavity surface, which is modeled using a set of point charges. The latter generate a "reaction field" which acts on the solute, modifying its charge density, therefore the surface charges must be calculated self-consistently.[35] Thus, the presence of the solvent has a direct effect on the electron density of the solute, but also an indirect effect on its molecular geometry, and all molecular geometries must be re-optimized when going from the gas phase to the solvated phase.

Inclusion of solvent contributions on spectroscopic properties calls for additional care because the solvent has a direct interaction with the electromagnetic radiation, in addition to the one mediated by the solute, and because of the dynamical nature of spectroscopic phenomena. The presence of the solvent changes the electromagnetic field that stimulates the spectroscopic response within the molecule, therefore the "local field" acting on the molecule will not be the same as the external field physically

imposed on the system. Classically, this problem is solved via the Onsager-Lorentz model,[91] which approximates the molecule as a point-like electric dipole, while the solvent is modeled with a polarizable continuum. If the dipole is placed at the center of a spherical cavity within the polarizable continuum the local field can be related to the external field through a multiplicative factor which depends on the solvent static dielectric constant for static fields ($\vec{E}^{\,\mathrm{loc}}$), and on the solvent optical dielectric constant for dynamic fields ($\vec{E}^{\,\mathrm{loc}}_{\omega}$):

$$\vec{E}^{\,\mathrm{loc}} = \frac{\varepsilon + 2}{3}\vec{E}^{\,\mathrm{ext}} \qquad ; \qquad \vec{E}^{\,\mathrm{loc}}_{\omega} = \frac{\varepsilon_{\mathrm{opt}} + 2}{3}\vec{E}^{\,\mathrm{ext}}_{\omega} \tag{5.1}$$

this rather crude approximation for the local field effect does not substantially improve the quality of the results with respect to the experimental values,[156] because it acts as a simple scaling factor that only depends on the solvent and therefore it is the same for any molecule and any type of spectroscopy. In PCM the molecule is described using the whole electronic density calculated quantum-mechanically, and not just the dipole term, and the cavity is molecule-shaped rather than spherical. The electric field experienced by the molecule is then the sum of the reaction field and the local field. Consequently, rather than modifying the electric field itself, the attention is equivalently switched to the electric dipole of the system, which is written as the sum of the molecule dipole moment and the dipole moment arising from the molecule-induced dielectric polarization (denoted by $\tilde{\mu}$):[70]

$$\vec{\mu}^{\,\mathrm{eff}} = \vec{\mu}^{\,\mathrm{mol}} + \tilde{\mu} \tag{5.2}$$

In the case of IR and VCD, $\vec{\mu}^{\,\mathrm{eff}}$ denotes the transition dipole moment between two vibrational states, while in the case of optical rotation it denotes the oscillating dipole moment of the system. The effective dipole moment can also be used to compute the electronic polarizability and its derivatives, in order to include local field effects in the computed Raman intensities.

Another aspect that should be taken into account by the model is the

so-called nonequilibrium regime which pertains to the dynamical aspects of solvation. The electromagnetic field acting on the system causes the electronic density of the solute, and solute-induced solvent polarization, to oscillate. Depending on the time scale of the phenomenon, not all degrees of freedom of the solvent can remain at equilibrium with the solute. This effect is treated within PCM by splitting the solvent polarization in two contributions, a "fast" polarization attributed to the degrees of freedom of the solvent that remain at equilibrium with the solute, and a "slow" component which accounts for the degrees of freedom that remain static. The partition of the different degrees of freedom of the solvent into the two contributions depend on the property under study.

Optical rotation is usually measured using light in the visible range of the electromagnetic spectrum, and can be seen as a consequence of the interference between the incident radiation and the radiation generated by the molecule's oscillating electronic density.[10] The electronic degrees of freedom of the solvent are able to follow the time evolution of the electronic density of the solute maintaining an equilibrium configuration, whereas the vibrational, rotational, and translational degrees of freedom, whose characteristic timescales are much lower than the period of oscillation of visible radiation, will remain static, so they account for the "slow" component of the solvent polarization. If vibrational corrections to the OR are also to be computed, an additional nonequilibrium contribution arises, which stems from a different partition of the solvent polarization. In this case the electronic and vibrational degrees of freedom are related to the "fast" component, while the "slow" component arises from the translational and rotational degrees of freedom.[71,72]

The vibrational nonequilibrium solvation regime also affects the calculation of IR and VCD spectra, both at the level of the vibrational analysis (normal modes and normal mode frequencies) and the spectroscopic IR and VCD intensities. It is therefore crucial to include nonequilibrium effects while performing the harmonic vibrational analysis and the subsequent calculation of the anharmonic contributions, in order to compute all terms constituting the observables in a consistent manner.[28]

Raman spectroscopy is not a purely vibrational phenomenon: the incident light usually lies in the visible part of the spectrum, with an oscillation frequency that calls for the use of the *electronic* nonequilibrium in the electronic part of the calculation, i.e. when computing the electronic polarizability. Raman activity is the recovered by computing the geometrical derivatives of the polarizability. As in the case of IR and VCD spectroscopy, this differentiation can be performed by considering the vibrational degrees of freedom of the solvent as either "fast" or "slow" compared to the solute's vibrational motion, i.e. by using a vibrational equilibrium or nonequilibrium solvation regime.[72] Therefore, there are two levels of nonequilibrium which should be considered that enter different stages of the *ab-initio* calculation of Raman intensities. In this work, in order to partially account for these effects we assume the PCM cavity to be fixed in space, i.e. the geometrical arrangement of the solvent stay equilibrated to the solute equilibrium geometry. All PCM cavity geometric derivatives of both the energy and polarizability shall then be discarded.

5.2.1 Vibrational averaging of electronic properties

From a theoretical point of view, the optical rotation of a molecular system can be calculated from the isotropic average of the electric dipole-magnetic dipole dynamic polarizability tensor[10] G'_{ab}:

$$[\alpha] = -\frac{4\pi}{3}\frac{\omega}{c}\frac{N_{\mathrm{A}}}{M_{\mathrm{w}}}\sum_{a} G'_{aa} \tag{5.3}$$

where ω is the angular frequency of the incident radiation, N_{A} is Avogadro's number, and M_{w} is the molar mass of the chiral substance. To compute the optical rotation of isotropic media the isotropic average of the G' tensor (i.e. the trace) is calculated. Optical rotation is a mixed electric-magnetic property and, because of the fact that in all *ab initio* calculations only a finite and therefore not complete basis set is used, it suffers from the so-called gauge problem, which causes the calculated values to depend on the origin of the chosen reference frame.[157] This origin-dependence is,

of course, unphysical and must be corrected. To circumvent this problem a number of techniques have been developed, and in this work origin independence was ensured by employing *Gauge Including Atomic Orbitals* (GIAOs).[158,159] In the particular case of PCM calculations of magnetic (or mixed electric-magnetic) properties, an additional PCM term is to be included in the Fock operator.[81,160]

Previous studies[161–166] have pointed out the need to include vibrational contributions in the calculation of molecular properties. In this work we have included vibrational effects by performing a vibrational averaging[167] of the molecular property P using an anharmonic vibrational nuclear wavefunction described by means of second order perturbation theory (VPT2).[20,21] In this framework the averaged property is expressed as the sum of the purely electronic property calculated at the equilibrium geometry and a temperature-dependent anharmonic vibrational correction given by:[5,29,167]

$$\Delta_{\mathrm{VC}}P = -\frac{\hbar}{4}\sum_a \frac{1}{\omega_a^2}\left(\frac{\partial P}{\partial Q_a}\right)_0 \sum_b \frac{K_{abb}}{\omega_b}\coth\frac{\hbar\omega_b}{2k_{\mathrm{B}}T} + \frac{\hbar}{4}\sum_a \frac{1}{\omega_a}\left(\frac{\partial^2 P}{\partial Q_a^2}\right)_0 \coth\frac{\hbar\omega_a}{2k_{\mathrm{B}}T} \tag{5.4}$$

Equation (5.4) depends explicitly on the temperature T and contains the first and diagonal second derivatives of the molecular property P (i.e. the OR) calculated with respect to the mass-weighted normal modes and evaluated at the equilibrium geometry of the molecule, the angular frequencies of the normal modes ω_a, the anharmonic semi-diagonal third derivatives of the electronic energy K_{abb}. The first term in the expression is a consequence of the anharmonicity of the potential energy surface (PES) while the second term would be present even at the harmonic level of the PES, and both terms are sums that run over all normal modes of vibration. Note that, because of the anharmonicity of the PES, increasing the temperature changes the vibrational corrections of all modes, not just the low energy ones, which become more populated. For a mode a with high energy (compared to k_BT) the first term of the vibrational corrections can change significantly provided the mode is strongly coupled to a low energy mode b through the anharmonic cubic constant K_{abb}, while the second term will be practically temperature-independent. For low energy

modes the same reasoning applies for the first term, but there will also be a significant temperature-dependence in the second term. As temperature increases, the single terms of the vibrational correction tend to increase, but since they may have different signs the total correction may increase or decrease. In this work, anharmonic terms and property derivatives are calculated numerically by automatically displacing the molecular geometry along each normal mode by a fixed amount, and computing the property and force constants matrix at each geometry. The above expression is valid for a molecule in the gas phase, and needs to be re-adapted in the case where solvent effects are included in the model. The presence of the solvent, treated in this work using PCM, alters both the electronic density and the PES of the molecular system. Therefore the vibrational analysis, which yields the normal modes of vibration, must be repeated for all solvents considered, as the normal modes and their frequencies will be affected. As pointed out in the Introduction, when computing spectroscopic properties in solution additional solvent effects should be included in the model, namely those arising from the local field and nonequilibrium effects.[168] These effects are included in the model at all stages of the calculation, therefore both the electronic property and the anharmonic vibrational correction are calculated in the presence of the solvent.

5.2.2 Anharmonic vibrational spectroscopic calculations with the inclusion of solvent effects

The IR, VCD, and Raman intensities corresponding to a vibrational transition from the ground state $|0\rangle$ to an excited vibrational state $|n\rangle$ are proportional respectively to the dipole strength, rotational strength, and Raman activity, which are defined as:[10]

$$D_{0n} = \{\langle 0|\mu_\alpha|n\rangle\langle n|\mu_\beta|0\rangle\}_\Omega \tag{5.5}$$

$$R_{0n} = \{\langle 0|\mu_\alpha|n\rangle\langle n|m_\beta|0\rangle\}_\Omega \tag{5.6}$$

$$A_{0n} = \{\langle 0|\alpha_{\alpha\beta}|n\rangle\langle n|\alpha_{\gamma\delta}|0\rangle\}_\Omega \tag{5.7}$$

Where μ, m, and α denote the electric and magnetic dipole moments and the polarizability, respectively. $\{\cdot\}_\Omega$ denotes the isotropic average over all possible molecular orientations, and in the case of IR and VCD corresponds to computing the trace of the tensor, while for the Raman activity it reduces to a linear combination of the isotropic polarizability and symmetric anisotropy, with coefficients that depend on the particular experimental configuration one is trying to reproduce.[7] The peak positions are equal to the energy difference between the ground and excited states, which can be computed from the vibrational analysis of the system. Usually these quantities are calculated by employing a harmonic description for the nuclear wavefunction, while the electric and magnetic dipole moments are expanded in a Taylor series about the equilibrium geometry, and the second or higher order terms are neglected. The combination of these two methods to treat the PES and the dipole moments is often referred to as the double harmonic approximation.

It has been pointed out in previous works[29,31,112] that neglecting the effects due to the anharmonicity of the PES and the higher order terms in the expansion of the dipole moments may yield substantial errors in the calculation of vibrational energies and peak intensities. Another drawback of the harmonic approximation is that all overtones and combination bands have vanishing intensity, giving rise to a much less detailed spectrum, with the exploration of some frequency ranges entirely precluded. In this work we treated this problem using VPT2[20,21,25,29,30] which allows to compute anharmonic corrections to both vibrational energies and spectroscopic intensities. In addition to the anharmonicity of the PES, the method extends the Taylor expansion of the dipole moments and polarizability up to third order, and by combining it with the anharmonic vibrational wavefunction yields the anharmonic vibrational intensities, which will be non-zero for single overtones and combination bands of two different normal modes, producing a much more realistic and detailed spectrum with respect to the one obtained by means of the double harmonic approximation. Recent works[28,31,168] have pointed out the need to include environment effects in the calculation of vibrational spectra in order to

obtain results directly comparable to experiment. Also in this case the solvent was treated by means of the PCM method.

5.3 Computational Details

All DFT calculations were performed with a locally modified version of the Gaussian 09 development version[113] program using the popular B3LYP[117,118] exchange-correlation functional. The equilibrium geometries of (S)-nicotine in the two conformations considered were optimized using the aug-N07D[169] basis set. For optical rotation we used the aug-cc-pVTZ[122] basis set to compute the electronic part of the property, and the aug-N07D basis set for the vibrational corrections, to reduce their computational cost. The use of a smaller basis set for the vibrational corrections than the one used for the electronic property is justified by the fact that the former are expected to be small compared to the latter, therefore the relative error due to the incompleteness of the basis set will have a smaller impact on the final calculated value. The use of different levels of theory in the calculation of the various contributions to a molecular property has been shown to be a reliable method by Puzzarini et al.[170] The aug-N07D basis set was also used to calculate the anharmonic IR and VCD spectra. Origin independence was ensured by using *Gauge Including Atomic Orbitals* (GIAOs).[158]

The optical rotation of (S)-nicotine was calculated for the system *in vacuo* and 2-propanol solution. The solvents were chosen because of the availability of experimental values to compare to our results. The vibrational corrections to both properties were calculated at 0 K and 298 K, the latter temperature chosen to reflect the experimental conditions. Optical rotations were evaluated at the wavelength of the sodium D line (589.3nm). The IR and VCD spectra were computed for nicotine in chloroform solution.

All geometry optimizations and Raman spectra calculations of *p*-nitroaniline (pNA) were performed using the range-separated CAM-B3LYP[114] functional, because of the push-pull charge-transfer character of the system.

All calculations on pNA employed either the the aug(sp)-cc-pVDZ, which removes diffuse d functions from the standard aug-cc-pVDZ[122] basis, or the m-aug-cc-pV(T+d)Z basi set by Truhlar et al.[171] again with the diffuse d functions removed. Cheeseman and Frisch[172] showed that removing diffuse d functions, in the case of the former basis set, while leading to much faster calculations compared to its parent, it does not lead in a significant reduction in accuracy in the computed Raman and Raman Optical Activity intensities.

Solvent effects were included in the calculations by means of the Polarizable Continuum Model (PCM)[35,36], with local field effects[5,47,70] and within the electronic[89] and vibrational[28,71] nonequilibrium regimes. The PCM cavity was built using a set of interlocking spheres centered on the atoms and with the following radii (in Ångstroms): 1.443 for hydrogen, 1.926 for carbon, and 1.830 for nitrogen, each multiplied by a factor of 1.1. The solvents' static and optical dielectric constants (the latter used for the nonequilibrium and local field calculations) used are $\varepsilon = 19.3$ and $\varepsilon_{\text{opt}} = 1.9$ for 2-propanol, and $\varepsilon = 4.7$ and $\varepsilon_{\text{opt}} = 2.1$ for chloroform. Gauge invariance in PCM calculations was assured by exploiting the method developed by Cammi.[81]

5.4 Results and Discussion

5.4.1 Nicotine conformations

The conformational distribution of nicotine *in vacuo* and in solution has been previously studied both theoretically and experimentally.[143–146] As a result, it has been established that both in the gas phase and in solution nicotine can assume any of four conformations (figure 5.2), whose relative populations depend on the solvent. Elmore and Dougherty[143] also computed the potential energy barriers separating the conformers, verifying the assumption that the different conformers may be treated as individual molecular species, each with its own equilibrium geometry and normal modes of vibration. In all conformations the pyrrolidinic ring assumes an

	trans-A	*trans*-B
Vacuo	69	31
$CHCl_3$	65	35
2-PrOH	62	38

Table 5.1: Boltzmann populations (in %) of the nicotine conformers in chloroform and 2-propanol.

envelope conformation while the pyridinic ring lies perpendicular to it. The pyridinic ring and the methyl group can be either *cis* or *trans* with respect to each other (hence the names of the conformations in figure 5.2) and the rotation of the pyridinic ring about the bond connecting the two rings gives the molecule additional conformational freedom which allows to distinguish the four different conformations. We calculated the population of the four nicotine conformers in each solvent taken into consideration in this work, i.e. chloroform and 2-propanol. The Boltzmann populations depend upon the relative free energies of the conformers, which were computed with the inclusion of solvent, vibrational, and thermal effects. Note that by employing PCM the computed electronic energy actually has the status of a free energy.[32,35] We also included non-electrostatic contributions calculated using the SMD molecular cavity,[45] which was specifically designed to estimate energies of solvated systems. The resulting populations of the *cis* conformers were below 1%, therefore in the following only the *trans* conformations were considered. Table 5.1 shows the relative Boltzmann populations of the nicotine conformers in the solvents considered in this work. The population of the *trans*-B conformer increases with increasing solvent polarity, and this is consistent with the fact that the dipole moment of the molecule in the *trans*-B conformation (2.88 Debye) is larger than that of the *trans*-A conformation (2.58 Debye).

Table 5.2 shows the electronic component ($[\alpha]_{\mathrm{D}}^{\mathrm{el}}$) and the vibrational corrections to the specific rotation of (S)-nicotine *in vacuo* and in 2-propanol solution at two different temperatures ($\Delta_{\mathrm{VC}}[\alpha]_{\mathrm{D}}$), as well as the total calculated specific rotation obtained by summing the electronic

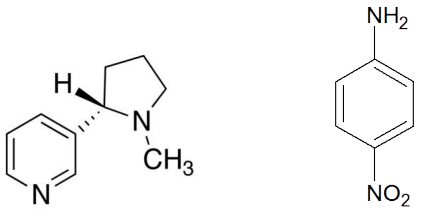

(a) (S)-nicotine **(b)** pNA

Figure 5.1: Structure of (S)-nicotine and *p*-nitroaniline (pNA).

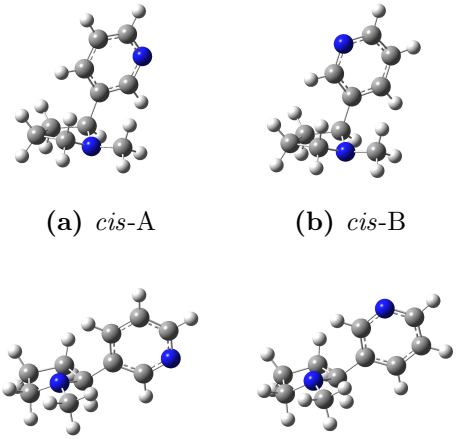

(a) *cis*-A **(b)** *cis*-B

(c) *trans*-A **(d)** *trans*-B

Figure 5.2: The four main conformations of nicotine.

	2-PrOH		vacuo	
	trans-A	*trans*-B	*trans*-A	*trans*-B
$[\alpha]_{\mathrm{D}}^{\mathrm{el}}$	-233.95	-227.59	-229.76	-210.31
$\Delta_{\mathrm{VC}}[\alpha]_{\mathrm{D}}^{\mathrm{0K}}$	-0.60	-1.73	-4.48	-3.03
$\Delta_{\mathrm{VC}}[\alpha]_{\mathrm{D}}^{\mathrm{298K}}$	7.22	6.24	-16.58	-1.38
$[\alpha]_{\mathrm{D}}^{\mathrm{298K\ tot}}$	-224.69		-235.58	
$[\alpha]_{\mathrm{D}}^{\mathrm{exp}}$	-250		-	

Table 5.2: Calculated and experimental[148] specific rotation of (S)-nicotine in deg dm^{-1} g^{-1} cm3.

component and the 298K vibrational correction for each conformer and by averaging the results according to Boltzmann populations ($[\alpha]_{\mathrm{D}}^{\mathrm{T\ tot}}$). The experimental value ($[\alpha]_{\mathrm{D}}^{\mathrm{exp}}$) for the optical rotation in 2-propanol is also reported. The purely electronic values calculated at the B3LYP/aug-N07D level of theory only differ from the B3LYP/aug-cc-pVTZ ones by about 2% both *in vacuo* and in solution, therefore the use of the smaller basis set in the vibrational corrections calculations is justified. At the electronic level the solvent causes the optical rotation to increase for both conformers, and a much more pronounced effect can be seen for the zero-point vibrational corrections which significantly decrease in magnitude when solvent effects are added. Temperature has a huge impact on the vibrational corrections, both *in vacuo* and in solution. Vibrational corrections are obtained by summing the contributions from all normal modes (see equation 5.4). The gas-phase vibrational correction at 298K increases greatly in magnitude for the *trans*-A conformer, while it decreases for the *trans*-B conformer, but the overall effect to the Boltzmann-weighted value is to increase the amount of the correction. The vibrational corrections calculated in 2-propanol increase in magnitude for both conformations and even change sign, demonstrating the importance of including solvent effects into the vibrational component, as well as the electronic value. We also computed the specific rotation of the two *cis* conformers to ensure that their contribution can indeed be discarded; we obtained a value of about +180 for both conformers which, because of their very low Boltzmann population, would not give a significant contribution to the average value.

The sign of the calculated specific rotation in 2-propanol is in agreement with the experimental value, and the relative error of the calculated value with respect to the experimental one is about -10%. While vibrational corrections do not improve the agreement, this might be due to explicit solvent effects originating from the directional nature of the hydrogen bonds that may be present in the nicotine/propanol system. Explicit solvent effects may be treated using hybrid QM/MM/PCM methods[60] and their application to nicotine is reserved for future work.

5.4.2 IR and VCD Spectroscopy

In order to compare our results with the experimental values, the calculated intensities were used to plot the IR spectra by convoluting the stick spectrum with Gaussian functions with an half-width at half-maximum chosen to be 10 cm^{-1} to match experimental data, and by assuming that the highest band in the spectrum corresponds to a 90% transmittance. The harmonic and anharmonic IR spectra of nicotine in chloroform are shown in figure 5.3a and 5.3b. The harmonic spectrum is manifestly separated in two different zones pertaining to different molecular vibrations: all C-C and C-N stretching and all bending motions appear in the 0-1650 cm^{-1} zone (modes 1-58), while C-H stretching motions emerge in the 2800-3200 cm^{-1} zone (modes 59-72), the rest of the spectrum appearing featureless due to the fact that the harmonic spectrum only shows fundamental bands. The modes are numbered by increasing harmonic frequency (see figure 5.5 for a pictorial representation of the normal modes of vibration mentioned throughout this work).

All the bands in the anharmonic spectrum appear red-shifted with respect to the harmonic one; the tendency of the anharmonic frequencies to be lower than the harmonic ones is general, and is particularly significant for the C-H stretching modes, whose anharmonic frequency is on average 145 cm^{-1} lower in with respect to the harmonic one, whereas the frequency of the other modes is on average 22 cm^{-1} lower. Furthermore anharmonic corrections change the ordering of some modes, so that wrong assignments would result from direct comparison between the experimental spectrum and its computed counterpart employing the harmonic approximation.

The anharmonic spectrum also shows a more complex structure due to the presence of the overtone and combination bands of two normal modes of vibration. This effect is especially noticeable in the 1600-2700 cm^{-1} region of the spectrum, which shows a large number of bands with small intensity. In the C-H stretching region the spectrum shows additional peaks with high intensity that are not present in the harmonic spectrum and arise from the combinations of modes 52 and 50, 54 and 48, and 56 and

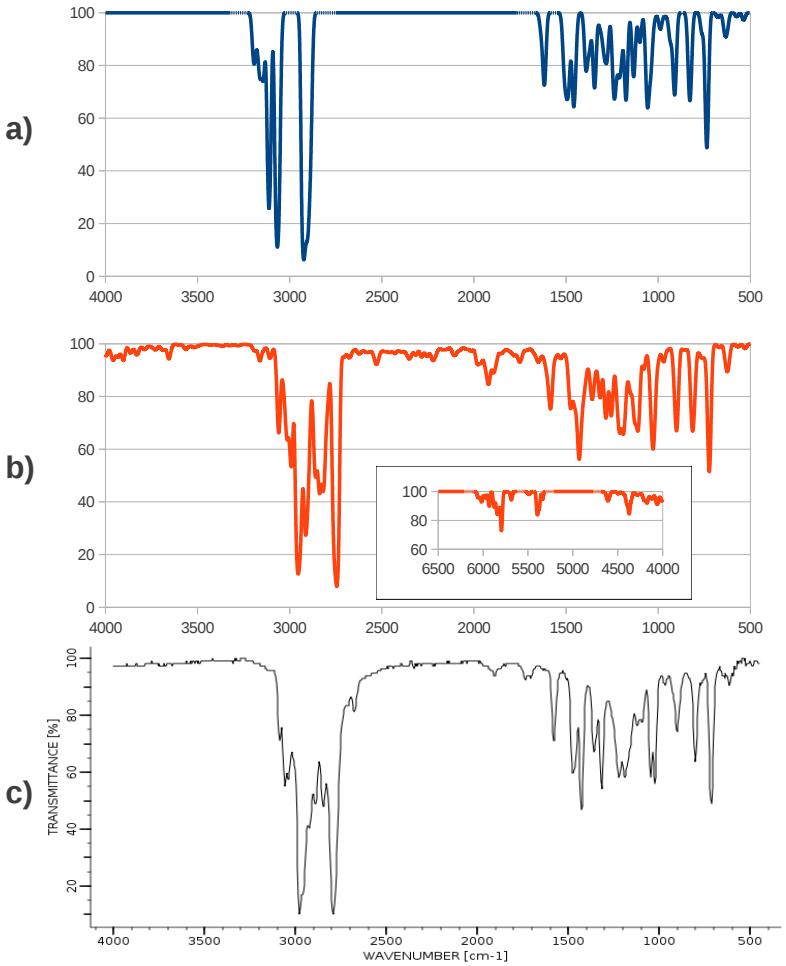

Figure 5.3: IR spectra of Nicotine. a) Harmonic spectrum. b) Anharmonic spectrum, the inset shows the 4000-6500 cm^{-1} region. c) Experimental spectrum.[173] Wavenumbers are reported in cm^{-1} and intensities % Transmittance.

47. Finally in the 4000-6500 cm^{-1} region (inset of figure 5.3b) overtone and combination bands of the higher energy modes can be seen. Around 5800 cm^{-1} there is a band which arises from the combinations of modes 66 and 62, 65 and 63, and 67 and 64, which are all C-H stretching localized on the pyrrolidinic ring. In the 5400 cm^{-1} region there is a band which is the superposition of the first overtones of mode 59 and mode 60, which are again C-H stretchings on the pyrrolidinic ring. Finally there is a band at 4380 cm^{-1}, which is mainly a combination band of modes 66 and 51.

The inclusion of the anharmonicity into the model also has a visible effect on the relative intensity of the fundamental bands. To give one example, a close inspection of the bands in the 0-1650 cm^{-1} zone reveals that the two peaks arising from the excitation of modes 50 and 55, which appear at 1460 cm^{-1} and 1510 cm^{-1} in the harmonic spectrum and at 1427 cm^{-1} and 1476 cm^{-1} in the anharmonic spectrum, have an almost identical intensity in the harmonic spectrum, while in the anharmonic spectrum the excitation of mode 50 is enhanced and that of mode 55 is quenched.

The experimental spectrum[173] is reported in figure 5.3c. The resemblance between the experimental spectrum and the calculated anharmonic one is remarkable: the positions of the peaks are in excellent agreement, whereas the harmonic spectrum fails dramatically to reproduce them, especially in the C-H stretching region. The calculation allows for a ready assignment of the spectral bands that can be seen in the experimental spectrum: the two highest peaks which appear at about 2980 cm^{-1} and 2785 cm^{-1} in the experimental spectrum can be respectively assigned to the fundamental bands of modes 65 and 60 respectively. As suggested by further inspection of the anharmonic and experimental spectra, the overtone and combination bands contribute heavily in delineating the band shape, and some combination bands are also separately identifiable, for example the two small bands near 1990 cm^{-1} and 1720 cm^{-1} that appear beyond the region where all bendings and heavy atom stretchings fall. Some of the bands in the 4000-6500 cm^{-1} region of the anharmonic spectrum have an intensity that is comparable to that of some bands that are

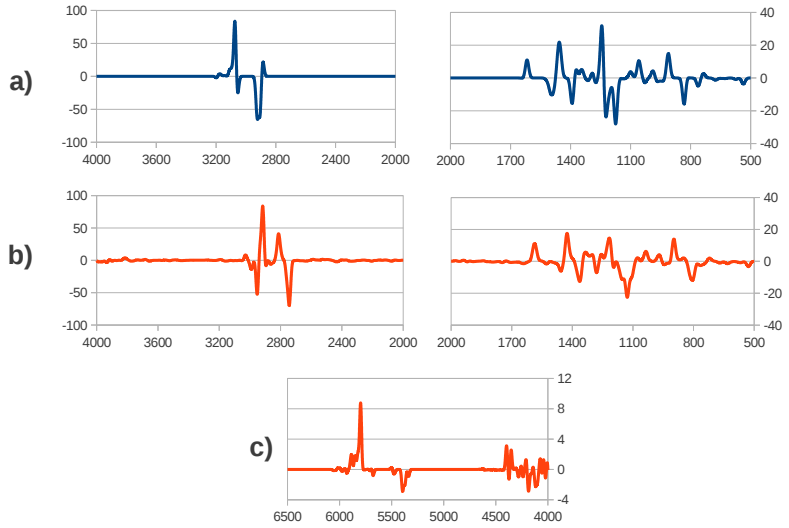

Figure 5.4: Calculated VCD spectra of Nicotine. a) Harmonic spectrum. b) Anharmonic spectrum. c) Anharmonic spectrum, overtones region. Wavenumbers are reported in cm^{-1} and intensities in arbitrary units.

clearly visible in the bending region, therefore it can be safely assumed that they would have also been visible in the experimental spectrum had it been recorded beyond 4000 cm^{-1}. Overall the inclusion of anharmonic effects in the calculation greatly increases the quality of the calculation with respect to the experimental data.

The calculated VCD intensities were convoluted with non-normalized Gaussian functions with half-width at half-maximum arbitrarily chosen to be 10 cm^{-1}. The calculated VCD spectra are shown in figure 5.4. To improve clarity, the spectra have been split into different zones with a different scale. Figure 5.4a shows the harmonic spectrum, figure 5.4b the anharmonic spectrum, and figure 5.4c shows the 4000-6500 cm^{-1} zone of the anharmonic spectrum. Both the harmonic and anharmonic VCD spectra appear much less detailed than the corresponding IR spectra, though VCD is a chiral method so the spectrum carries information about the absolute configuration of the system. The difference between the harmonic and anharmonic frequencies discussed for the IR spectra also applies in the case of the VCD spectra in exactly the same way. Frequency shift

aside, the two spectra appear similar in the 500-2000 cm^{-1} zone. A noticeable difference can still be observed, mainly due to two combination bands which have a substantial intensity, i.e. the combination of modes 22 and 7 found at 1130 cm^{-1}, and the combination of modes 19 and 11 found at 1215 cm^{-1}, and due to the quenching of the two negative fundamental bands of modes 35 and 38, and of the positive fundamental band of mode 39, found at 1175 cm^{-1}, 1230 cm^{-1}, and 1240 cm^{-1} respectively, in the harmonic spectrum.

A much more pronounced difference between the harmonic and anharmonic spectra can be appreciated in the C-H stretching region, where the presence of the high intensity combinations of modes 56 and 47 and modes 54 and 48 produce an additional positive band, and the combination of modes 57 and 49 gives rise to a visible negative band, all of which are not present in the harmonic spectrum. Unfortunately, to the best of our knowledge, experimental VCD spectra have never been reported in the literature for this system, so that a direct comparison with experiment is not possible.

5.4.3 Raman Spectroscopy

Before moving to the calculation of Raman spectra of pNA in solution we analyzed the effect of the basis set on the harmonic spectrum. Figure 5.7 shows the harmonic Raman spectra of pNA in vacuo computed for an incident wavelength of 520 nm using the aug(sp)-cc-pVDZ basis set and the triple-zeta quality m-aug-cc-pV(T+d)Z basis set. The two spectra are very similar, both in terms of peak positions (i.e. harmonic frequencies) and intensities. The most noticeable frequency change is observed for the band at 1430 cm^{-1}, for which the second basis set yields a redshift of 16 cm^{-1}. Changes in relative Raman intensities are also rather small, therefore in all subsequent calculations we employed the smaller and cheaper double-zeta quality basis.

We computed the harmonic and anharmonic Raman spectra of pNA in three different solvents of varying polarity: chloroform, methanol, and

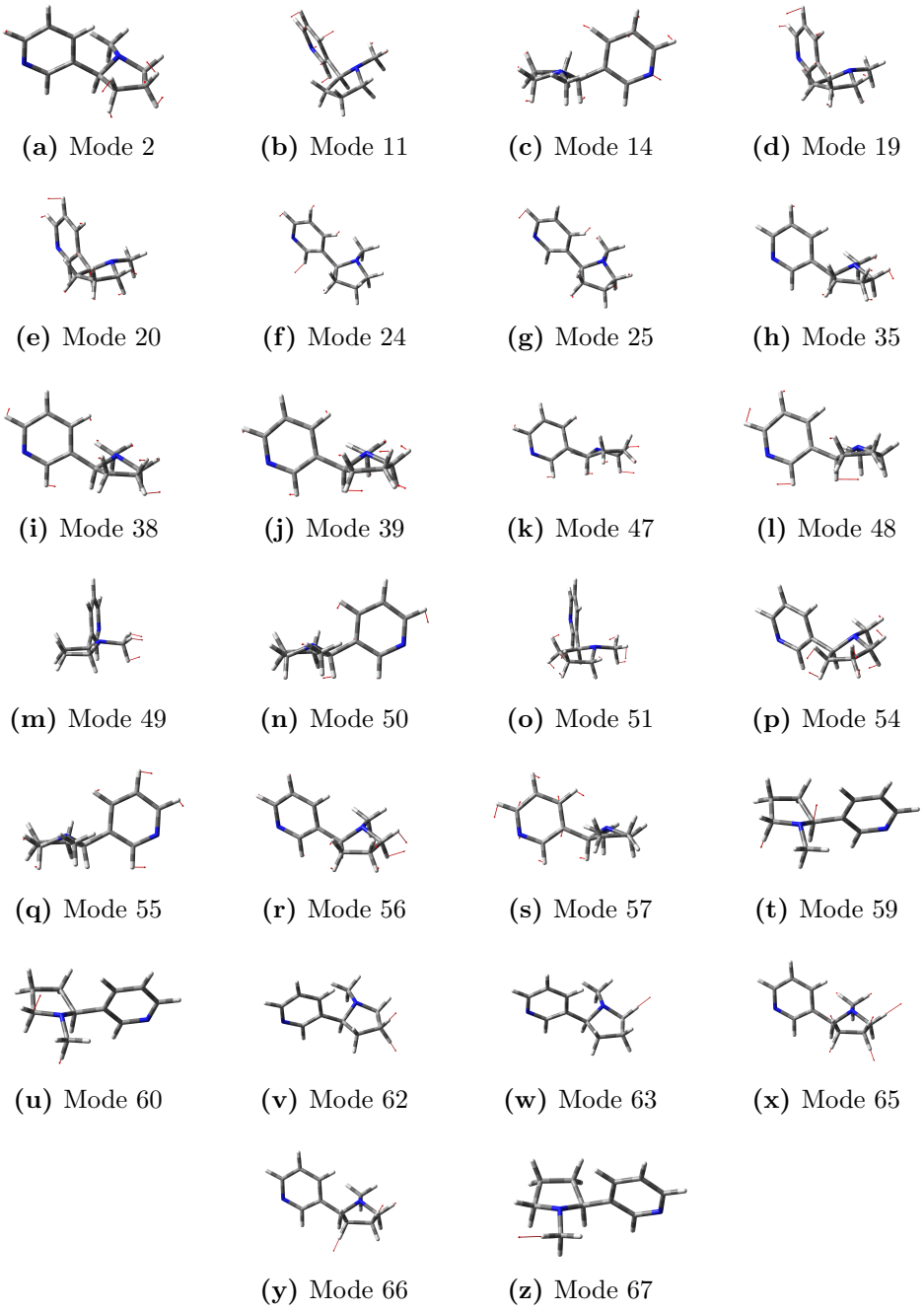

(a) Mode 2 **(b)** Mode 11 **(c)** Mode 14 **(d)** Mode 19

(e) Mode 20 **(f)** Mode 24 **(g)** Mode 25 **(h)** Mode 35

(i) Mode 38 **(j)** Mode 39 **(k)** Mode 47 **(l)** Mode 48

(m) Mode 49 **(n)** Mode 50 **(o)** Mode 51 **(p)** Mode 54

(q) Mode 55 **(r)** Mode 56 **(s)** Mode 57 **(t)** Mode 59

(u) Mode 60 **(v)** Mode 62 **(w)** Mode 63 **(x)** Mode 65

(y) Mode 66 **(z)** Mode 67

Figure 5.5: Normal modes of nicotine.

water. In addition, in the case of methanol, we also investigated the effect of changing the frequency of the incident radiation. The computed absolute Raman cross-sections were convoluted with Gaussian functions with a half-width at half-maximum of 10 cm^{-1}. Results are reported in figure 5.8. The effect of changing the solvent polarity can be appreciated by looking at the experimental spectra[174] (black lines). The most evident feature is the change in the relative intensity of two strong bands that appear at 1300 cm^{-1}, which are assigned, in order of increasing energy, to the symmetric and antisymmetric stretching of the two C-N bonds present in the molecule, with a contribution from the in-plane C-H bending motions (figure 5.6c and 5.6d). In chloroform, the symmetric stretching has a much higher intensity than the antisymmetric one, whereas in methanol and water the situation is reversed. The other peaks have a smaller intensity and appear less affected by the solvation environment. The effect of the incident frequency on the computed spectrum can be evaluated by comparing the spectra recorded in methanol for a 1064 nm and a 514 nm wavelength. The greatest difference, in this case, is the change in relative intensity of the two peaks at 900 cm^{-1} (a C-NO_2 stretching with contributions from a ONO symmetric bending and symmetric C-C stretching, figure 5.6a) and 1150 cm^{-1} (a C-NO_2 stretching, figure 5.6b), with the former showing a significant increase in intensity for the smaller wavelength.

The computed harmonic (red line) and anharmonic (blue line) spectra present several differences. As expected, anharmonicity has the effect of redshifting all bands, overall significantly increasing the agreement with experimental data. The effect of anharmonicity, however, is not limited to band positions, and small differences can be observed in the case of intensities as well. Anharmonicity also has interesting effects when combined with solvation: it can be seen that, in the case of methanol, the intensity pattern of the two highest peaks is only reproduced when both solvation and anharmonicity are included in the calculation, since at the harmonic level the symmetric C-N stretching still has a higher intensity with respect to the antisymmetric one. In the case of water the pattern is correct at the harmonic level as well, however anharmonicity further

enhances the difference between the two peaks. The high intensity of the band of mode 5.6b for methanol and water is not well reproduced by either the harmonic and the anharmonic calculation. One possible reason is the neglect of specific solvation effects which are likely present in protic solvents, in fact it has been shown[175] that nitro groups in substitued benzene rings can act as proton acceptors in hydrogen bonding, with appreciable effects on the resulting IR spectra. Another possible explanation lies in the fact that the peaks of modes 5.6a and 5.6b appear to be strongly affected by the frequency of the incident radiation, with the former being enhanced and the latter quenched by an increase in the frequency. While the calculated spectra show a similar trend, the magnitude of this effect is much smaller than the one observed in the experimental results. The cause may be attributed to the chosen electronic structure method: the electronic polarizability can be written as a sum-over-states expression and, as the incident frequency increases, the contributions from the lowest-energy excited states increase as well. If the chosen DFT functional overestimates the excitation energies of the molecule then this effect will not be as pronounced. In fact, at the CAM-B3LYP/aug(sp)-cc-pVDZ level of theory, the first vertical excitation of pNA in water appears at 326 nm (or 30700 cm^{-1}), whereas the maximum of the experimental absorption spectrum recorded by Thomsen et al.[176] was found to be at 380 nm, with the onset of the band appearing at 430 nm. We therefore computed the Raman spectrum of pNA in water for a series of decreasing wavelengths (see figure 5.9). The two peaks of modes 5.6a and 5.6b at 900 cm^{-1} and 1150 cm^{-1} are greatly affected by the change in incident frequency, and the agreement with the experimental spectrum improves significantly for higher frequencies, wereas the other bands are largely unaffected.

The first dipole-allowed excitation computed for pNA in vacuo appears at a much higher energy, at 286 nm (or 35000 cm^{-1}), therefore we can expect a similar effect on peak intensities to appear at higher laser frequencies. We computed the Raman excitation profiles of of modes 5.6a and 5.6b for pNA in vacuo and water (see figure 5.10). Indeed, the pattern is very similar, but the two curves cross at higher energies for the gas

phase plot. The computed Raman activity diverges as the incident frequency approaches the first dipole-allowed excitation energy since we are only computing the real part of the polarizability, without the inclusion of an imaginary damping term. A more general treatment of the complex response function would remove the discontinuity and provide a continuous transition to a Resonance Raman spectrum.[177–182] Note that in vacuo the first computed excitation energy appears at 309 nm (or 32350 cm^{-1}), but it is of A_2 symmetry and, therefore, dipole-forbidden, whereas in water the first transition has an A_1 symmetry. If the transition dipole moment is null then the state does not contribute to the *harmonic* spectrum in the sum-over-state expression of the polarizability. To see this in more detail it is possible to compare the Taylor expansion of the electronic polarizability with the series obtained by expanding the transition dipole moments and the excitation energies directly:

$$\alpha^{\mathrm{el}} = \frac{1}{\hbar} \sum_{j \neq 0} \frac{2\nu_j}{\nu_j^2 - \omega^2} \vec{\mu}^j \vec{\mu}^j \tag{5.8}$$

where $\hbar\nu_j$ is the excitation energy from the ground state to the electronic state j and depends upon the molecular geometry, while $\vec{\mu}^j$ is the corresponding transition dipole moment. Both can be expanded in a Taylor series about the ground state equilibrium geometry (summation over the

normal modes Q is implied):*

$$\nu_j = \omega_j + F_a^j Q_a + \frac{1}{2} F_{ab}^j Q_a Q_b + \dots \tag{5.9}$$

$$\vec{\mu}^j = \vec{\mu}_0^j + \vec{\mu}_a^j Q_a + \frac{1}{2} \vec{\mu}_{ab}^j Q_a Q_b + \dots \tag{5.10}$$

where $\hbar\omega_j$ is the vertical excitation energy, and F_a^j and F_{ab}^j are the first and second derivatives of ω_j (the first derivatives are essentially the excited state forces since we are at the equilibrium geometry). The transition dipole moments and its derivatives can be used to define the Franck-Condon, Herzberg-Teller, and higher-order contributions to electronic one-photon spectra. If we plug these expansions into the polarizability expression we have:

$$\alpha^{\mathrm{el}} = \underbrace{\frac{2}{\hbar} \sum_{j \neq 0} \frac{\omega_j}{\omega_j^2 - \omega^2} \vec{\mu}_0^j \vec{\mu}_0^j}_{\alpha_0^{\mathrm{el}}} + \underbrace{\frac{2}{\hbar} \sum_{j \neq 0} \left(\frac{\omega_j}{\omega_j^2 - \omega^2} (\vec{\mu}_0^j \vec{\mu}_a^j + \vec{\mu}_a^j \vec{\mu}_0^j) - \frac{\omega_j^2 + \omega^2}{\left(\omega_j^2 - \omega^2\right)^2} F_a^j \vec{\mu}_0^j \vec{\mu}_0^j \right)}_{\left(\frac{\partial \alpha^{\mathrm{el}}}{\partial Q_a}\right)} Q_a + \dots \tag{5.11}$$

Clearly, if $\mu_0^j = 0$ then the electronic state j does not contribute to the harmonic spectrum. Note however that singularities in the computed Raman spectrum may arise at the anharmonic level, when higher derivatives of the polarizability are included. Special care must be taken in this case, especially since we compute the second and semi-diagonal third derivatives of the polarizability by numerical differentiation of the first derivatives, which are available analytically.[183–185]

It is clear from these results that computing the Raman spectrum by differentiating the *static* polarizability rather than the correct dynamic

*The frequency-dependent and dipole terms are expanded this way:

$$\frac{2\nu_j}{\nu_j^2 - \omega^2} = \frac{1}{\nu_j - \omega} + \frac{1}{\nu_j + \omega}$$

$$\frac{1}{\nu_j \pm \omega} = \frac{1}{\omega_j \pm \omega} - \frac{1}{(\omega_j \pm \omega)^2} F_a^j Q_a + \frac{1}{2} \left(\frac{1}{(\omega_j \pm \omega)^3} F_a^j F_b^j - \frac{1}{(\omega_j \pm \omega)^2} F_{ab}^j \right) Q_a Q_b + \dots$$

$$\vec{\mu}^j \vec{\mu}^j = \vec{\mu}_0^j \vec{\mu}_0^j + (\vec{\mu}_0^j \vec{\mu}_a^j + \vec{\mu}_a^j \vec{\mu}_0^j) Q_a + \frac{1}{2} (\vec{\mu}_0^j \vec{\mu}_{ab}^j + \vec{\mu}_{ab}^j \vec{\mu}_0^j + \vec{\mu}_a^j \vec{\mu}_b^j) Q_a Q_b + \dots$$

(a) (b) (c) (d)

Figure 5.6: Normal modes of pNA referenced in the text. They are all of a_1 symmetry.

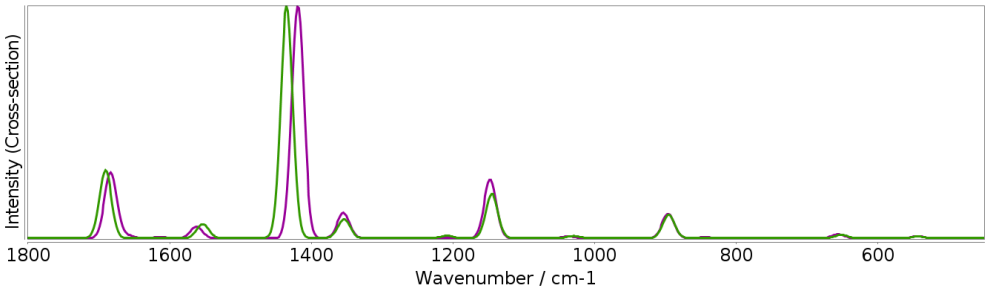

Figure 5.7: Harmonic Raman spectra of pNA in vacuo calculated with the CAM-B3LYP functional and the aug(sp)-cc-pVDZ basis set (green line) or the m-aug-cc-pV(T+d)Z basis set (purple line).

one, as is most often done, besides being physically inconsistent, can lead to significant errors in the calculated intensities.

5.5 Conclusions and Perspectives

In the present work we have shortly reported on the latest developments of our virtual chiroptical spectrometer to effectively deal with the tuning of the spectroscopic outcome by stereo-electronic, vibrational, and environmental effects. After a short sketch of the most important building blocks we analyzed in detail several kinds of spectra of nicotine in different solvents. Our results show that anharmonicity (for both frequencies and intensities) and subtle solvent effects (e.g. nonequilibrium and local fields) cannot be neglected when making a direct comparison with experiment. Thanks to software and hardware developments, all these effects

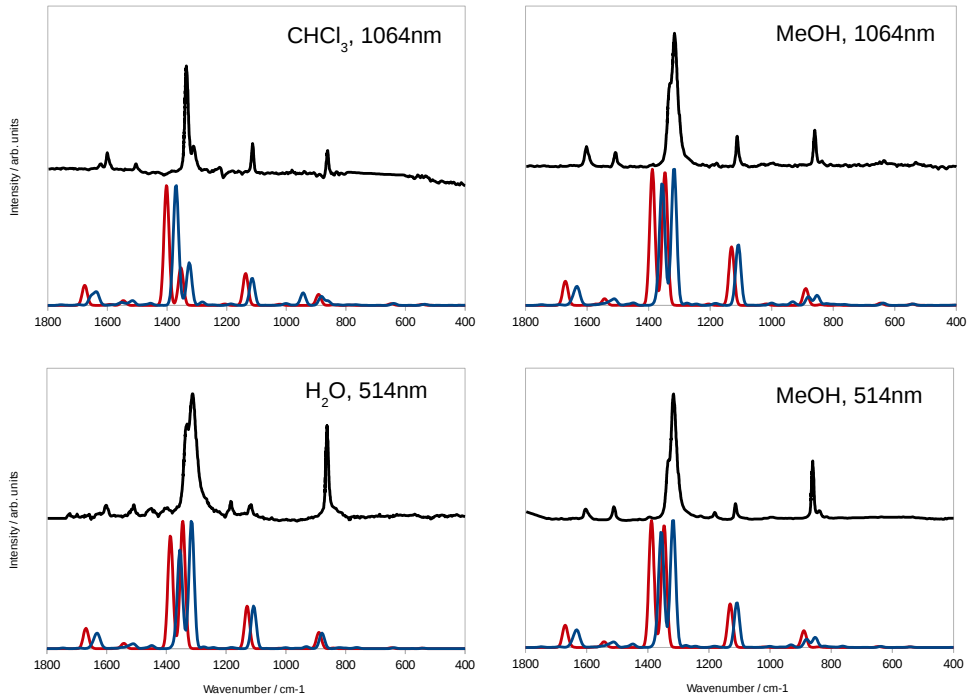

Figure 5.8: Calculated harmonic (red lines), anharmonic (blue lines) and experimental[174] (black lines) Raman spectra of pNA. The solvent and frequency of the incident radiation are reported on the top-right side of each spectrum. Wavenumbers are in cm^{-1} and intensities in arbitrary units.

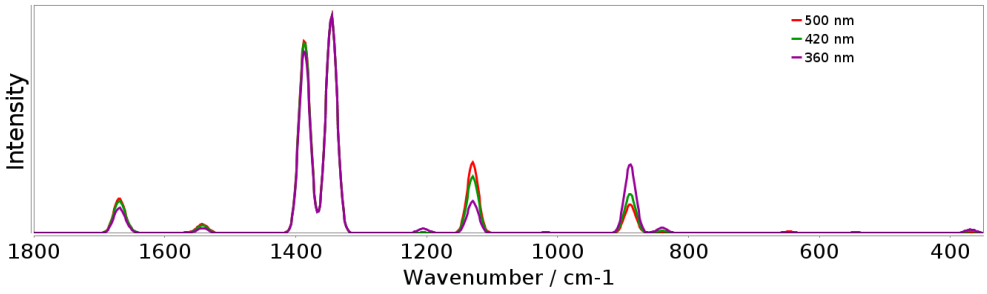

Figure 5.9: Harmonic spectra of pNA in water computed at different wavelengths: 500 nm (red line), 420 nm (green line), 360 nm (purple line). Wavenumbers are in cm^{-1} and intensities in arbitrary units.

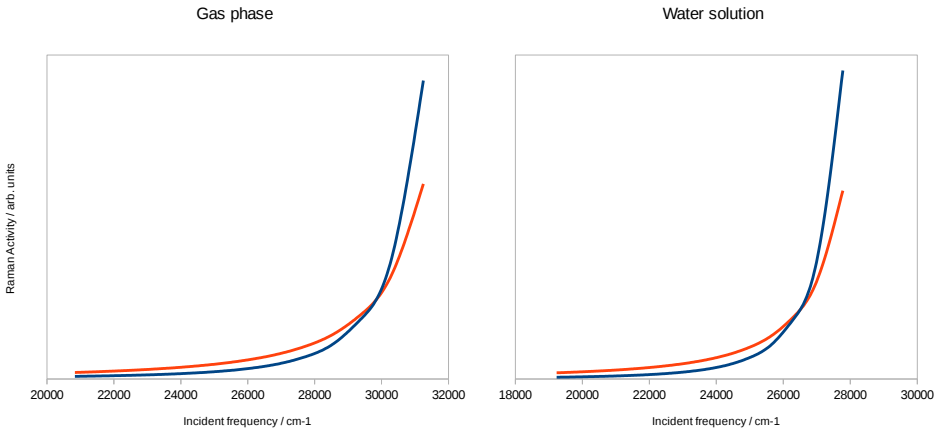

Figure 5.10: Excitation profiles of the peaks at of mode 5.6a at 900 cm^{-1} (blue line) and 5.6b at 1150 cm^{-1} (orange line) of pNA in vacuo and water. Wavenumbers are in cm^{-1} and Raman activities are in arbitrary units.

can now be effectively taken into account also for quite large molecules, thus allowing proper assignment of spectra and correct disentanglement of the role played by the different effects in tuning the overall experimental outcome. Together with the specific interest of the system at hand, in our opinion our results show that, though further developments are necessary and undergoing, we already dispose of a robust, powerful and user-friendly tool easily accessible also to non-specialists.

Chapter 6

Resonance Raman

In this final chapter we shall partake in the exploration of an efficient computational approach for the simulation of Raman spectra in the case where the incident radiation frequency is in resonance with one or more electronic excitations of the system. In particular, we present an effective time-independent implementation to model vibrational resonance Raman (RR) spectra of medium-large molecular systems with the inclusion of Franck-Condon (FC) and Herzberg-Teller (HT) effects and a full account of the possible differences between the harmonic potential energy surfaces of the ground and resonant electronic states. Thanks to a number of algorithmic improvements and very effective parallelization, the full computations of fundamentals, overtones, and combination bands can be routinely performed for large systems possibly involving more than two electronic states. In order to improve the accuracy of the results, an effective inclusion of the leading anharmonic effects is also possible, together with environmental contributions under different solvation regimes. Reduced-dimensionality approaches can further enlarge the range of applications of this new tool. Applications to imidazole, pyrene, and chlorophyll $a1$ in solution are reported, as well as comparisons with available experimental data. The text has been readapted from the original publication.[3]

6.1 Introduction

Resonance Raman spectroscopy (RR) has received much attention in recent years and has found applications in many areas such as analytical chemistry[186] and the study of metal complexes[187] and biological systems.[188–190] The first distinguishing feature that RR shows with respect to non-resonant Raman is the so-called resonance enhancement:[191] the intensity of the scattered radiation is 10^3-10^6 higher than the intensity of the regular Raman signal. This property facilitates experimental measurements and, in most cases, also causes the resulting spectrum to be free from any "contamination" arising from the non-resonant Raman signal, which has a much smaller intensity. Resonance enhancement is also responsible for granting RR spectroscopy other peculiar features. Since it is due to the interaction of the incoming radiation with an electronic transition of the system, a RR spectrum carries information about the excited state(s). Traditionally, the methods of choice to study excited-state properties of molecules are UV-vis absorption and fluorescence spectroscopies. Both these methods have two disadvantages: first, because of the naturally short lifetime of some excited states, and because of the inhomogeneous broadening caused by the environment, the band-width of most electronic transitions is usually very broad, especially in the case of molecules in solution; this "dilutes" the information that could be extracted from the spectrum, and it is usually difficult to record vibrationally resolved electronic spectra, even though the band-shape may be dominated by the vibronic structure. In RR, the band-width only depends on the initial and final states,[191] which both belong to the ground state potential energy surface (PES), therefore the peaks' width is comparable to the case of a non-resonant Raman spectrum. Another advantage of RR over traditional one-photon spectroscopies is that it is a vibrational spectroscopy, whence it is much easier to extract structural information about the system. A second consequence of the resonance enhancement is that only the molecular vibrations that are affected by the electronic transitions (in particular those vibrations that involve atoms close to the chromophore) will be vis-

ible in the spectrum because all other vibrational modes will not benefit from the enhancement and will have negligible intensity. This property is heavily exploited in the study of biological macromolecules,[189,190] in which one may tune the incident radiation's frequency to one particular chromophore within the system, obtaining information about the corresponding region of the macromolecule; if a regular Raman or infra-red spectrum is recorded, the high number of vibrational transitions of the molecule will produce an "overcrowded" spectrum which would be difficult to interpret.

All such characteristic features of RR have stimulated the research in this field, both experimentally[191] and theoretically,[192] but there is still much work to be done in both areas. In this contribution we present our work on the time-independent (TI) calculation of RR spectra[16] within a general-purpose quantum chemistry program, with an emphasis on the computational applicability and scaling of the method with respect to system size. The implementation was designed as an integrated module in the multi-frequency virtual spectrometer under development in our group;[101] in this way it can take advantage of the various features already present such as the handling of large systems through reduced-dimensionality schemes, the modeling of the solvation environment, and anharmonicity. The present work is organized as follows: after an introduction on the theoretical framework of RR, the inclusion of anharmonicity and of environmental effects is discussed. As an illustration of the versatility and reliability of our procedure, we analyze the spectra of three different systems: imidazole, pyrene, and chloropyll $a1$.

6.2 Resonance Raman scattering cross-section

Raman scattering can be formally thought as a two-photon phenomenon where an incident electromagnetic radiation is inelastically scattered by the system, which can either absorb (Stokes scattering) or release (anti-Stokes scattering) energy. The ability of a molecular system to give rise to Raman scattering is related to its transition polarizability tensor[10] be-

tween two different vibrational states belonging to the same electronic level. The Raman cross-section can be easily computed once the transition polarizability is known. For isotropic media it can be expressed as a combination of three isotropic invariants corresponding to the mean isotropic polarizability, the symmetric anisotropy, and the antisymmetric anisotropy, defined as[13] (summation over repeated indices is implied):

$$a^2 = \frac{1}{9}\,\mathrm{Re}\,\alpha^{\mathrm{s}*}_{aa}\alpha^{\mathrm{s}}_{bb} \qquad g^2 = \frac{1}{2}\mathrm{Re}(3\alpha^{\mathrm{s}*}_{ab}\alpha^{\mathrm{s}}_{ab} - \alpha^{\mathrm{s}*}_{aa}\alpha^{\mathrm{s}}_{bb}) \qquad d^2 = \frac{3}{2}\,\mathrm{Re}\,\alpha^{\mathrm{a}*}_{ab}\alpha^{\mathrm{a}}_{ab} \tag{6.1}$$

where α^{s} and α^{a} are the symmetric and antisymmetric components of the polarizability tensor. For example, in the case of 90 degrees scattering with an incident radiation of frequency ω perpendicularly polarized with respect to the scattering plane, and an unpolarized scattered radiation,[7] we have:

$$\sigma'(\pi/2, \|^{\mathrm{s}} + \perp^{\mathrm{s}}, \perp^{\mathrm{i}}) = \frac{\omega_{\mathrm{s}}^4}{c^4}\frac{45a^2 + 7g^2 + 5d^2}{45} \tag{6.2}$$

where $\omega_{\mathrm{s}} = \omega - \omega_{fi}$ is the angular frequency of the scattered radiation. These expressions are general, and are applicable to both the resonant and non-resonant cases. One important difference, however, is that the non-resonant transition polarizability is symmetric, giving a vanishing contribution from the d^2 term. There are several methods for the calculation of the RR polarizability, with different levels of approximations. The theoretical framework of RR can be traced back to the work of Placzek,[193] who obtained sum-over-state formulas for the Raman transition polarizability in the resonant and non-resonant cases starting from the perturbation expansion of the wavefunction, and later Albrecht[194] who gave separate expressions for the various contributions of the polarizability arising from the expansion of the transition dipole moments. The RR polarizability can then be written as a sum-over-state expression as follows:[10]

$$\tilde{\alpha}_{\alpha\beta} = \frac{1}{\hbar}\sum_{m'}\frac{\langle f|\mu_\alpha|m'\rangle\langle m'|\mu_\beta|i\rangle}{\omega_{mi} - \omega - i\gamma} \tag{6.3}$$

where $\langle f|$ and $|i\rangle$ represent the final and initial vibrational states respectively, $\omega_{mi} = \omega_m - \omega_i$ is the energy difference between the middle and initial state, μ_α and μ_β are the Cartesian components of the transition dipole moments between the ground and excited electronic states, γ is the excited state's phenomenological damping constant, and the (infinite) summation runs over all vibrational states m' belonging to the excited state PES. An equivalent expression for the RR polarizability can be obtained in the time domain:[195–197]

$$\tilde{\alpha}_{\alpha\beta} = \frac{i}{\hbar} \int_0^\infty \langle f|\mu_\alpha \, \mathrm{e}^{-i\hat{H}'t/\hbar} \, \mu_\beta|i\rangle \, \mathrm{e}^{i(\omega_i+\omega)t-\gamma t} \, \mathrm{d}\, t \tag{6.4}$$

Both the time-dependent and the time-independent expressions require a model for the ground and excited PESs, and for the transition electric dipole moment. Usually the harmonic approximation is invoked for both states, but even though a geometry optimization followed by a harmonic analysis can be routinely performed for the ground state with most electronic structure methods, the same task may prove to be much more difficult in the case of an excited state, and often requires a numerical differentiation of the energy gradient, which is much more time consuming. For this reason, further approximations are often invoked and most calculations of RR spectra assume that both states have the same normal modes and harmonic frequencies, and differ only in the equilibrium geometry, this assumption being known as the independent mode displaced harmonic oscillator[198] (IMDHO) model. The latter model has been extensively used to compute RR spectra,[199–205] based on either the time-dependent or the time-independent formulations. Additional methods used for the calculation of RR spectra can be derived by further manipulation of the time-dependent expression, which can be viewed as an equation for the motion of the starting vibrational wavepacket on the excited state PES. Under short-time dynamics conditions,[195–197] it is possible to write the relative RR peak intensity as a ratio between the excited-state gradients calculated along the normal modes under consideration.[206–209] The latter method is the simplest one for computing RR spectra and requires neither a sum-

over-state calculation, nor the evaluation of a half-Fourier transform. Following an alternative treatment, which also relies on the short-time dynamics approximation, it is possible to evaluate the RR spectrum by computing the geometrical derivative of the complex electronic polarizability under resonance conditions using linear response theory,[177–182,210] similarly to what is commonly done to compute frequency-dependent non-resonant Raman intensities, but with the additional complication that the finite lifetime of the excited state must be included in the calculation to avoid the singularities that appear in the undamped linear response equation. It should be clear from this brief discussion that there is currently a profusion of widely different methods that are used to compute RR spectra, each based on different assumptions and presenting its own challenges and advantages, and there are also a few works in the literature that have attempted to compare them against each other and also with respect to experimental data.[200,211,212] However, the majority of RR spectra calculations present in the literature still relies on the IMDHO model to describe the excited-state PES. This provides a rather unbalanced description of the two states involved since a geometry optimization followed by a full harmonic analysis is performed for the ground state, whereas only the gradients are usually computed for the excited state. If the excited state's normal modes are computed, the integrals which appear in the TI or TD polarizability expressions cannot be straightforwardly computed since the harmonic wavefunctions of the two PESs are expressed in different basis sets. In order to solve this problem, in the case of semi-rigid molecules without large-amplitude motions,[213] the excited state normal modes can be related to the ones of the ground state via an affine transformation known as the Duschinsky relation:[214]

$$\boldsymbol{Q'} = \mathbf{J}\boldsymbol{Q} + \boldsymbol{K} \tag{6.5}$$

Where $\boldsymbol{Q}$ and $\boldsymbol{Q'}$ are the ground and excited state normal modes respectively, and $\mathbf{J}$ and $\boldsymbol{K}$ are the Duschinsky matrix and the shift vector. By means of the Duschinsky relation it is possible to write down explicit equa-

tions that allow the calculation of RR intensities both in the TI and TD frameworks.[16,215–218] As already pointed out, the most straightforward way to compute the Duschinsky matrix is to perform a geometry optimization followed by a vibrational analysis for both states. This method is often called Adiabatic Hessian (AH),[219] but it is not the only way to obtain a meaningful description of the excited state normal modes. Indeed, the vibrational analysis for the excited state may also be performed at the ground state equilibrium geometry and the shift vector can be extrapolated from the gradient, a method known as Vertical Hessian (VH).[219,220] If the harmonic approximation is exact then the two methods are equivalent, otherwise the choice of using one or the other depends on whether one needs a better description of the vertical region or the minimum of the excited PES. If the Duschinsky rotation is ignored and excited-state frequencies are not computed, the simplified methods known as Vertical Gradient (VG) and Adiabatic Shift (AS) are obtained; in the first one, only the excited-state gradient at the ground-state equilibrium geometry is computed, whereas for the second one the excited-state geometry is optimized, but the shape of the PES is then assumed to be the same as in the ground state.

6.2.1 Time-Independent calculation of the RR polarizability

In this work, we chose the time-independent approach for the calculation of the RR polarizability tensor. The transition dipole moments that appear in equation 6.3 can be expanded in a Taylor series with respect to the excited-state normal modes around the molecule's equilibrium geometry. Keeping only the terms up to the second order in the polarizability we

obtain:

$$\begin{aligned}\tilde{\alpha} =&\frac{1}{\hbar}\sum_{m'}\Bigg[\vec{\mu}_0\vec{\mu}_0\frac{\langle f|m'\rangle\langle m'|i\rangle}{\omega_{mi}-\omega-i\gamma}+\\&+\sum_a\left(\vec{\mu}_a\vec{\mu}_0\frac{\langle f|Q'_a|m'\rangle\langle m'|i\rangle}{\omega_{mi}-\omega-i\gamma}+\vec{\mu}_0\vec{\mu}_a\frac{\langle f|m'\rangle\langle m'|Q'_a|i\rangle}{\omega_{mi}-\omega-i\gamma}\right)+\\&+\sum_{ab}\left(\vec{\mu}_a\vec{\mu}_b\frac{\langle f|Q'_a|m'\rangle\langle m'|Q'_b|i\rangle}{\omega_{mi}-\omega-i\gamma}+\vec{\mu}_0\vec{\mu}_{ab}\frac{\langle f|m'\rangle\langle m'|Q'_aQ'_b|i\rangle}{\omega_{mi}-\omega-i\gamma}+\right.\\&\left.+\vec{\mu}_{ab}\vec{\mu}_0\frac{\langle f|Q'_aQ'_b|m'\rangle\langle m'|i\rangle}{\omega_{mi}-\omega-i\gamma}\right)\Bigg]\end{aligned}\tag{6.6}$$

where $\vec{\mu}_a$ and $\vec{\mu}_{ab}$ are the transition dipole moment first and second derivatives with respect to the normal modes. This way of writing the expansion of the polarizability allows to draw a parallel with the non-resonant Raman polarizability, which is expanded directly in a Taylor series up to at least the first order (and more, whenever anharmonicity effects are considered). The zeroth and first order dipole expansion terms that appear in the resonant case are commonly referred to as Franck-Condon (FC), and Herzberg-Teller (HT), therefore the terms that appear in the polarizability expression can be classified as mixed FC-FC, FC-HT, etc. terms, which can be considered the different orders in the expansion of the RR polarizability in the normal modes. The full second order of the polarizability contains a HT-HT term, and two FC-D2 terms (where D2 refers to the second order derivative of the transition dipole moment). In this work we stop the dipole expansion up to the HT terms, therefore the polarizability contains all FC-FC, FC-HT, and HT-HT terms. Note that in these expressions the dipole moments are expanded with respect to the excited state normal modes (all quantities referring to the excited electronic state are denoted by an apex). This choice allows for a simplification of the formulas to calculate the required Herzberg-Teller integrals and, if HT can be considered a good approximation, the two approaches are equivalent. The inclusion of HT terms is especially crucial in the case of symmetry-forbidden transitions, or transitions with a very low oscillator strength, while their inclusion may be forgone in the case of strongly

allowed transitions.

The integrals that appear in equation 6.6 can be computed recursively.[221–223] The time-independent formulation of the RR polarizability has been implemented within the Gaussian suite development version[113] by taking advantage of the features previously developed for one-photon spectra calculation,[14,15] and in particular for one-photon absorption (OPA) which requires the very same transition integrals as RR. As already mentioned, the time-independent scheme requires a truncation of the summation in equation 6.6 in order to be of any use. There is in principle an infinite number of middle states $\langle m'|$, therefore we need to screen them to select beforehand the states that are expected to give the greatest contribution to the dipole integrals. We have accomplished this by using a class-based method, described in Refs.[14,15,219,224,225]. The convergence of each Raman peak's calculation can be gauged by evaluating the expression obtained by neglecting the denominator contribution in equation 6.6 both numerically and analytically, as described in Ref.[16]. Alternative methods for the screening of integrals have also been proposed.[226–228] While the prescreening method attempts to reduce the number of middle states that need to be included in the calculation, their number can still be significant, and does scale with the size of the system. Fortunately each middle state contributes independently to the total sum-over-state, therefore equation 6.6 can be implemented in an effective parallel way, allowing us to apply our procedure to systems of medium and large size, without the need to introduce further approximations. More specifically, the middle states are separated into "classes" of excitations according to the number of simultaneously excited modes, and the contribution of a class is computed before moving to the next. Within each class, the calculation is split between all available processors, using a shared-memory Open Multi-Processing (OpenMP) protocol, and each processor treats a different family of middle states $\langle m'|$, where by family we intend a set of states with the same simultaneously excited oscillators, hence differing only by the number of non-null quanta for each mode. The number of states belonging to a class grows very rapidly with the class order, which

makes it the bottleneck of the calculation. Parallelizing the latter step can speed up the calculation almost linearly with the number of processors. Additionally, each Raman peak can be computed independently of the others, therefore the evaluation of the different band intensities can also be parallelized if multiple machines are available.

The TI formulation has a few advantages. Since the recursion formulas used to compute the FC integrals are completely general, it is possible to compute the intensity of overtone and combination bands up to any order and the computational cost for a combination band is not significantly higher with respect to a fundamental band (though the raw number of possible combinations grows rapidly with the maximum allowed quantum number and with system size). This also allows the straightforward inclusion of temperature effects in the calculation, since this requires to select a finite number of different initial states according to their Boltzmann population. Finite temperature spectra may contain a greater number of bands, whose computation can also be parallelized. The efficient implementation of FC integral calculation, along with the parallelization of the code, allows us to apply the TI picture with the Duschinsky and temperature effects to systems of medium-large size. Note that as the size of the system increases and we wish to keep intact the level of theory (i.e. inclusion of Duschinsky mixing) the actual RR spectrum calculation will never be the bottleneck of the whole computation since the excited-state vibrational analysis is by far the most demanding step (see section 8 for a specific example). The applicability of our method can therefore be extended to ever-larger systems by reducing the cost of the latter step, e.g. by using a more affordable basis set or even by estimating the second derivatives using semi-empirical methods, or running the various steps involved in the numerical differentiation on separate machines.

6.3 Anharmonicity effects

Even though peaks' intensities carry information about the excited electronic state of the system, RR can still be considered a vibrational spec-

troscopy since the transition involves two vibrational states belonging to the same PES. While a harmonic description of the ground-state PES to model vibrational spectroscopies can give good qualitative results, inclusion of anharmonic effects is often needed to achieve sufficient accuracy to allow a direct comparison with experimental results. This is especially true in the case of RR because peak positions are determined by the energies of the vibrational states, and it has been shown[29,31,112] that anharmonicity can have huge effects, resulting in shifts of as much as 150 cm^{-1} for C-H stretchings, and, more crucially, anharmonicity can affect the ordering of the vibrational modes, which can lead to erroneous peak assignments. The anharmonicity of the PES also affects spectroscopic intensities, as demonstrated in many works in the case of infra-red and vibrational circular dichroism spectra.[2,29,229–232] In the case of non-resonant Raman spectroscopy, the inclusion of anharmonic contributions on the intensities calls for both an anharmonic description of the PES, and the inclusion of additional terms in the Taylor expansion of the Raman polarizability as a function of the normal modes of vibration up to the third order (the so-called electrical anharmonicity).[29] In the TI picture of RR the transition dipole moment is instead expanded as a Taylor series, giving rise to Franck-Condon, Herzberg-Teller, and possibly higher terms, so the inclusion of anharmonicity rests on the sole description of the vibrational states. An additional challenge faced in the case of RR is the fact that intensities rely on an accurate description of the excited state PES in addition to the ground-state one, and if performing a complete harmonic vibrational analysis for an excited state can itself be quite demanding, going beyond the harmonic approximation can prove to be truly herculean, unless the excited state can be computationally treated like a ground state, e.g. whenever it has a different symmetry or spin multiplicity with respect to the "true" ground state, or in cases like photon-induced ionizations where an electron is removed from the system. Anharmonicity effects can be included at different levels of approximation and with different methods.[233,234] In this work we used our implementation[20,21,25,30] of second order vibrational perturbation theory (VPT2) which can pro-

vide an accurate description of both anharmonic vibrational energies and wavefunctions. In VPT2 the perturbed wavefunctions are expressed as linear combinations of harmonic states, and in order to use this kind of expression in calculation of Franck-Condon integrals, we would have to perform a large number of computations for each RR peak, with a prohibitive computational cost, bar for the smallest molecules. Because we are interested in applying our methodology to medium-large sized systems, we choose instead to limit the treatment of anharmonicity effects to the vibrational energies, which are employed in equation 6.6, in place of the harmonic ones, with no additional computational cost for the vibronic part. As already pointed out, computing the excited-state anharmonic frequencies with a full VPT2 treatment is computationally too expensive, and can only be done in conjunction with an electronic structure method for which analytical second derivatives of the excitation energy are available. We choose instead to use the ground-state anharmonic frequencies to estimate the excited-state ones, following the scheme proposed by some of us.[234] Since in general the excited-state normal modes differ from the ground-state ones, the anharmonic shifts computed for the latter cannot be directly applied to the former. To solve this problem we compute the scaling factors between the harmonic ground-state energies and their anharmonic counterparts and then use the Duschinsky transformation to estimate the corresponding scaling factors for the excited state. The estimated excited state anharmonic frequencies can then be written as:[234]

$$\omega_b'^{\mathrm{anh}} = \Big(\sum_a J_{ba}^2 \frac{\omega_a^{\mathrm{anh}}}{\omega_a^{\mathrm{harm}}} \Big) \omega_b'^{\mathrm{harm}} \tag{6.7}$$

Empirical scaling factors are commonly used to estimate anharmonicity effects for the ground state, and in fact they have also been used in the context of RR calculations.[206,235–237] Computing the scaling factors using vibrational perturbation theory, as opposed to using empirical ones, poses no transferability problems and is therefore much more suited for the estimation of the excited-state frequencies. The excited-state anharmonic frequencies are then inserted into equation 6.6 along with the ground-

state ones, and are also used in the recursion formulas used to compute the Franck-Condon integrals. It is worth noting that anharmonic frequencies are systematically lower than their harmonic counterparts, therefore if anharmonicity effects were included only in the ground state vibrational energies, the denominators in equation 6.6 would increase, leading to systematically lower absolute intensities. Because the anharmonicity shift tends to be much higher for higher-energy modes, this effect is also heterogeneous along the spectrum, leading to an error in the relative intensities, in addition to the absolute ones. It is therefore crucial that anharmonicity effects be included for both electronic states.

This method of treating the anharmonicity of excited states can be validated by applying the full VPT2 treatment to excited states which, because of symmetry or other reasons, require no TDDFT response calculations. It should be noted that our vibronic method is not applicable in cases where there is a very large change in geometry and normal modes of the excited state with respect to the ground state's because in that case the Duschinsky transformation is not sufficient to faithfully describe the relation between the two sets of normal modes. To summarize, our method for estimating anharmonic frequencies in the excited state seems suitable for those systems for which the vibronic spectrum can be computed in this framework. To support our claim, we computed the anharmonic frequencies of imidazole in its ground singlet state, and in its first triplet (T_0) and ionized (D_0) states. We then computed the Duschinsky matrix and the anharmonic shifts for the T_0 and D_0 states using equation 6.7 and compared the results.

While this method of treating anharmonic effects exonerates us from the calculation of high-order geometric derivatives of the excitation energy, computing the anharmonic frequencies for the ground state alone is still very demanding, and scales unfavorably with system size. Fortunately, RR spectroscopy can benefit greatly from the use of a reduced-dimensionality scheme. Usually one is only interested in a specific region of the spectrum, therefore it is not necessary to compute the anharmonic frequencies of the normal modes which lie outside of it. Computationally, this means that

the energy Hessian need only be computed after displacing the molecular geometry along the selected normal modes rather than the full ensemble, with a proportional saving in computational time. Unless the modes that are not included in the anharmonic treatment are very strongly anharmonic and strongly coupled to the selected modes, the discarded terms contribute marginally to the anharmonic correction, and can safely be eliminated, so peak positions are almost unaffected.[238,239] In addition, a very small effect on the computed RR intensities can be expected because the harmonic frequencies will be used in place of the anharmonic ones for the non-selected modes in equation 6.6. In our examples, the effect of anharmonicity on intensities is not very big, therefore we can safely apply our reduced dimensionality scheme in the most complex cases.

6.4 Environmental effects on resonance Raman spectra

Though some reports of RR spectra of molecules in the gas phase exist,[240–243] RR spectral measurements are most often performed on molecules in solution or more complex environments. The connection between the RR spectral response and the molecular environment is in fact so strong that RR measurements have been used to evaluate solvent reorganization energies associated with the electronic transition.[244–246] The most evident environmental effect on the spectrum is the change in the positions of the peaks, related to the change in the vibrational energies, which can be quite significant.[112] This change is one of the consequences of the change in the PESs and, by extension, in the vibrational wavefunctions that enter equation 6.3, causing a change in the intensity of the peaks, as well as their positions. Therefore we need a suitable computational protocol able to model the effects of the environment on all these parameters, having the capability of accurately calculating the energies, geometries, frequencies and vibrational wavefunctions of the system. While these requirements can be met by means of numerical algorithms, there are other

issues which have to be solved before the model can be considered suitable for modeling RR spectroscopy. By limiting ourselves to solvated systems (similar considerations also apply to generic systems composed of a core molecule interacting with an external environment), it should be taken into account that RR scattering is a dynamical process. Therefore, the response of the solvent to the core system interacting with the external field will occur at different timescales, depending on the different degrees of freedom of the solvent molecules surrounding the core system. This results in both homogeneous and inhomogeneous broadening effects of the spectral response caused by the presence of the solvating environment.[247] The component of the solute-solvent interaction that acts at the polarizability level can be modeled by including an additional time-dependent dephasing term in the exponent of equation 6.4, and if this is simplified by a constant term, there is a resulting increase in the observed value for the damping constant γ that appears in equation 6.3, so it can no longer be attributed solely to the finite lifetime of the excited electronic state. The choice of an appropriate value for the damping constant to be used in the spectrum simulation should therefore take into account the experimental conditions. In addition, the spectral peaks will also be broadened because of the presence of the solvent, and this latter effect can be empirically considered by using an arbitrarily chosen lineshape, such as a Gaussian or Lorentzian distribution function.

Coming back to the modeling of solvent effects on PESs, vibrational wavefunctions, and electronic excited states, a possible strategy consists in performing QM calculations within the framework of the Polarizable Continuum Model (PCM),[35,36] which has been used in the past to model solvent effects in the context of RR spectroscopy.[16,201,207,248–252] PCM is a so-called focused model, which treats the solvent as a continuum polarizable dielectric medium that hosts the solute molecule, treated quantum mechanically, within a molecule-shaped cavity. The presence of the polarizable continuum alters the solute electronic density, via an effective solvent-dependent term in the molecular Hamiltonian, which in turn affects the solvent response, until self-consistency, which finally results in

mutual solute solvent polarization effects. Besides such direct effects on the molecular electronic wavefunction, the presence of the continuum dielectric also alters the solute PES, i.e. its equilibrium geometry, vibrational frequencies and normal modes, resulting in a change in RR peaks' positions, but it also affects all excited state properties required in RR calculations (i.e. transition dipole moments, excited state forces, etc.).

PCM has been extensively used to model solvent effects on both vibrational and electronic spectroscopies thanks to the development of algorithms to include solvent contributions in the different terms entering equation 6.3.

The peculiar nature of RR as a mixed vibrational-electronic property calls for care when considering the solvent time evolution, in order to correctly account for the dynamical aspects of the solute-solvent interaction,[253] which differ if purely electronic,[89,90] vibrational[31,71] or mixed electronic/vibrational phenomena[72,253] are considered.

In the simple case of electronic absorption spectra, a possible (and most often used) partition of the solvent response to the electronic changes in the solute assumes the solvent electronic degrees of freedom to quickly equilibrate to the time-evolving solute electronic density, whereas the rest stay equilibrated to the unaltered ground state solute charge density, thus resulting in a nonequilibrium solute-solvent regime.[89,90,253] The same also applies to vibrational spectroscopies,[31,71] however the partition of the solvent response has to be done differently, because both the electronic and vibrational solvent degrees of freedom can, in this case, follow the solute charge density evolving in time. This formally results in a different definition of the nonequilibrium solvation regime.[2,31,47]

Unlike simple one-photon (electronic or vibrational) absorption, RR is at the same time a vibrational and an electronic phenomenon, therefore the definition of the physically consistent solvation regime to be used in the calculation of the RR polarizability is to be done with care.[253] By adopting a time-dependent picture, the RR polarizability can be seen as originating from the evolution in time of the starting vibrational wavepacket on the excited state PES. Therefore, depending on the timescale of such an

evolution, it might be assumed that some of the solvent's nuclear degrees of freedom remain static. To simulate such behavior within the PCM framework, extension of the vibrational nonequilibrium approach[28,71] to excited states, within the further account of electronic nonequilibrium effects would be necessary. Such a model has never been proposed so far. In this paper, in order to partially account for such effects we will assume the PCM cavity to stay fixed, i.e. the geometrical arrangement of the solvent stay equilibrated to the solute equilibrium geometry. This implies the PCM cavity geometric derivatives to be discarded in the evaluation of excitation energy gradients and/or Hessians. As far as the ground state is concerned, we will instead make use of the aforementioned vibrational nonequilibrium regime[31,71] It is worth remarking that the use of a fixed cavity cannot completely freeze the solvent's nuclear degrees of freedom, because the nuclear solvent response, which contributes to the PCM excited state computed properties, is evaluated within the nuclear equilibrium regime. A further approximation which we will exploit in the following consists of performing a numerical differentiation of the (electronic) nonequilibrium excitation energy, where each atom is displaced along each cartesian coordinate first in the positive and then in the negative direction, and the derivative is then computed numerically. The PCM cavity is also kept fixed. A univocal assessment of the (nuclear+electronic) solvation regime to be exploited in modeling RR spectra is far from trivial. Therefore, in the following we will compare three different approaches to compute the parameters required for a RR calculation:

1. Equilibrium solvation: all solvent degrees of freedom are equilibrated with the solute. Both ground state and excitation properties are computed in this manner and the PCM cavity is mobile.

2. Fixed cavity: the PCM cavity is kept fixed in the calculation of all energy derivatives, for both the ground state and excitation properties, where the former are computed under the vibrational nonequilibrium regime, and the latter are computed in the electronic equilibrium solvation regime.

3. Nonequilibrium: in addition to keeping the cavity fixed, the vertical excitation energy is computed under (electronic) nonequilibrium conditions, and is numerically differentiated.

The choice of the solvation regime should also be coherent with the treatment of the excited-state PES: in an adiabatic scheme, where the excited-state geometry is optimized and the PCM cavity is displaced along with it during the optimization, the equilibrium solvation should be selected. The other two regimes can be used in vertical treatments (VG or VH). In order to apply the other two solvation regimes to adiabatic schemes, the excited-state geometry optimization must also be performed with a fixed PCM cavity.

6.5 Computational details

All DFT, RR, and vibronic absorption calculations were performed using a development version of the Gaussian suite of quantum chemistry programs.[113] The B3LYP[117,118] functional is adopted for imidazole and chlorophyll $a1$, while PBE0[120] is used in the case of pyrene, following previous studies establishing this functional as appropriate for this system.[251] Some test computations on pyrene were also performed with the CAM-B3LYP[114] and the M06-2X[119] functionals. The basis set was chosen taking each system's size and consequent computational cost of each task into account. For imidazole the aug-cc-pVTZ[122] was used for all calculations, for pyrene and chlorophyll $a1$ the ground state harmonic frequencies were computed with the double-zeta SNSD basis set[254] whereas anharmonic effects and excited state frequencies were computed with the smaller 6-31G* basis set.

Solvent effects were taken into account using the Polarizable Continuum Model (PCM).[35,36] The PCM cavity was built using a system of interlocking spheres with the following radii expressed in Ångstroms: 1.443 for hydrogen, 1.926 for carbon, and 1.830 for nitrogen, 1.7500 for oxygen, and 1.5105 for magnesium, each multiplied by a factor of 1.1. The solvents'

static and optical dielectric constants used are $\varepsilon_0 = 78.36$ and $\varepsilon_\infty = 1.78$ for water, $\varepsilon_0 = 35.69$ and $\varepsilon_\infty = 1.81$ for acetonitrile, and $\varepsilon_0 = 32.61$ and $\varepsilon_\infty = 1.77$ for methanol.

All Complete Active Space Self-Consistent Field (CASSCF) and Multi-State Complete Active Space Second-Order Perturbation Theory (MS-CASPT2)[255] calculations were performed using the MOLCAS package (version 7.8).[256–258]

6.6 Imidazole in aqueous solution

Imidazole was chosen for its role in biological systems and because its small size and solubility in water allow for a very extensive analysis of the various contributions to the final spectra and of the different levels of approximation involved. For our study, we focused on the very bright $\pi - \pi^*$ transition, which appears around 210 nm. Because this transition is strongly allowed,[259] we performed our calculations at the FC level.

6.6.1 Anharmonicity effects

As already mentioned, imidazole is an ideal candidate to illustrate our method for treating anharmonicity effects in RR spectroscopy. We performed the full VPT2 anharmonic analysis[20,21,25,30] for imidazole in its ground S_0 state and first triplet state T_0, and for the radical cation ImH^+ in the lowest energy D_0 state. The calculations in each case involve a geometry optimization (see figure 6.1 for the three optimized geometries), followed by the calculation of harmonic force constants (to obtain the normal modes of vibration), and finally the numerical differentiations of the energy Hessian.

From the harmonic analysis of the three species, it is possible to compute the Duschinsky matrix and shift vector that relate the normal modes of the cation and the triplet to the normal modes of the singlet. Using equation 6.7 the anharmonic frequencies of the ground singlet state were used to estimate the anharmonic frequencies of the cation and triplet,

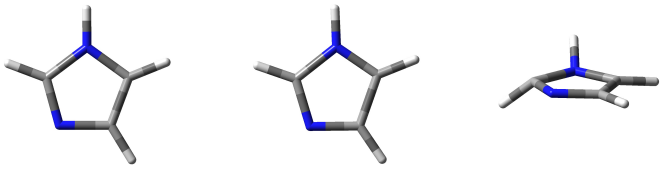

(a) ImH S_0 **(b)** ImH^+ D_0 **(c)** ImH T_0

Figure 6.1: Optimized structures of imidazole (singlet), imidazole cation (doublet), and imidazole (triplet).

which were compared to their VPT2 counterparts to assess the validity of our scaling scheme. The results are reported in table 6.1. The anharmonic frequencies obtained with the Duschinsky method are in excellent agreement with the VPT2 ones in the case of the doublet cation, with an average deviation of 0.4% and a maximum deviation of 1.1% for normal mode 15. A much larger deviation is observed in the case of the triplet state, with deviations as high as 43% for the first normal mode. This behavior can be explained from the observation of the optimized structures (figure 6.1). The optimized structure for the triplet state presents a significant pyramidalization of two atoms in the ring, resulting in a different molecular symmetry. The normal modes of the triplet state are poorly described in terms of the singlet state normal modes using a simple affine transformation such as the Duschinsky relation, leading to a very dense Duschinsky matrix (see figure 6.2), with many elements of significant magnitude for each row (or column). In this case our vibronic model is not applicable. From these results it is reasonable to suggest that this method of estimating anharmonic frequencies rests upon the same assumptions behind the vibronic model itself, i.e. there should be a limited structural deformation associated with the electronic transition. The Duschinsky matrix that relates the singlet and ionized imidazole is comparatively much more diagonal.

Figure 6.3 shows the harmonic and anharmonic RR spectra calculated for an incident wavelength of 224 nm, a damping of 500 cm^{-1}, and with

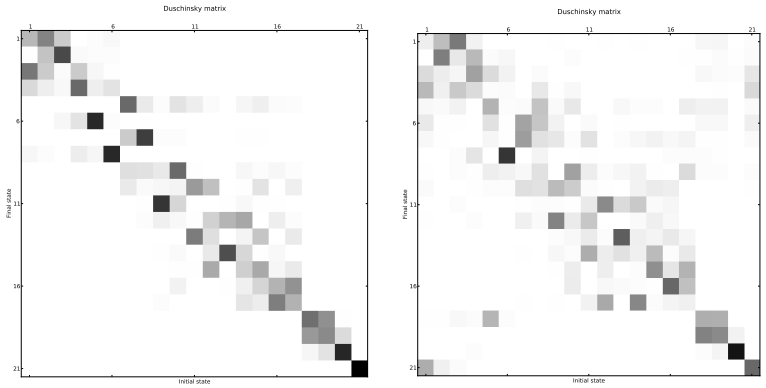

(a) ImH$^+$ D_0 **(b)** ImH T_0

Figure 6.2: Duschinsky matrices for the doublet cation (left) and neutral triplet (right). The figure shows two 21×21 matrices, where 21 is the number of normal modes. A darker shade denotes a higher absolute value of the matrix element.

		ImH S_0 (C_s)		ImH$^+$ D_0 (C_s)				ImH T_0 (C_1)			
#	Sym	Harm	VPT2	Harm	VPT2	Dusch.	% dev	Harm	VPT2	Dusch.	% dev
1	A”	540	533	496	491	487	0.78	201	137	196	43.14
2	A”	647	633	544	531	534	0.73	404	328	394	20.15
3	A”	683	673	707	690	694	0.70	467	392	455	16.00
4	A”	743	724	799	778	781	0.42	599	545	586	7.42
5	A’	827	810	825	806	810	0.57	736	611	719	17.80
6	A”	885	864	890	872	871	0.20	809	775	793	2.25
7	A’	908	895	923	907	908	0.14	832	801	815	1.86
8	A”	946	932	936	917	913	0.42	914	865	892	3.14
9	A’	1073	1049	964	942	944	0.26	916	871	895	2.75
10	A’	1093	1069	1043	1018	1021	0.24	1008	966	982	1.72
11	A’	1144	1121	1125	1105	1100	0.47	1049	1025	1024	0.05
12	A’	1159	1133	1212	1186	1184	0.21	1107	1074	1080	0.58
13	A’	1286	1261	1265	1242	1237	0.45	1262	1232	1229	0.25
14	A’	1363	1323	1295	1270	1267	0.22	1305	1271	1272	0.11
15	A’	1427	1389	1416	1365	1380	1.12	1358	1317	1322	0.40
16	A’	1499	1470	1453	1415	1421	0.41	1396	1346	1366	1.45
17	A’	1556	1524	1539	1494	1506	0.79	1541	1507	1501	0.37
18	A’	3242	3115	3235	3112	3109	0.09	3110	2988	2984	0.13
19	A’	3244	3118	3241	3116	3115	0.04	3180	3054	3055	0.05
20	A’	3272	3145	3248	3124	3122	0.05	3230	3083	3105	0.69
21	A’	3652	3484	3565	3399	3401	0.07	3467	3223	3325	3.17

Table 6.1: Comparison between VPT2 anharmonic frequencies and the ones estimated with the anharmonic scaling scheme based on the Duschinsky transformation. ImH denotes neutral imidazole, ImH$^+$ is the radical cation. Note that the optimized structure for the triplet state of imidazole has a different symmetry with respect to the singlet; the symmetry labels therefore do not apply in this case.

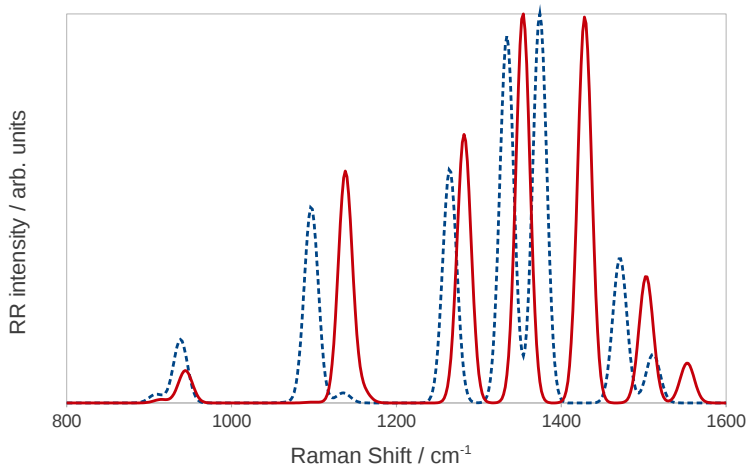

Figure 6.3: Harmonic (continuous red line) and anharmonic (dashed blue line) RR spectra of imidazole in water.

peaks convoluted with Gaussian functions with a half-width at half maximum (HWHM) of 10 cm^{-1}. The spectra were scaled to have the same maximum intensity to compare them more easily. As expected, anharmonic bands are systematically redshifted with respect to the harmonic ones, and there is also a significant difference in the computed relative peak intensities. Notice also that in the anharmonic spectrum there is a very small peak at 1136 cm^{-1} which, in the harmonic spectrum, is obscured by the intense peak close to it. We finally note that imidazole is a small system, i.e. it has a limited number of vibrational modes, thus the resulting spectrum is relatively simple. In case of more complex systems, the combination of peak displacements and changes in relative intensities can potentially lead to notable differences in the bandshapes.

6.6.2 Effect of the solvation regime

As pointed out previously, solvent effects can be crucial in RR spectroscopy, and the choice of the solvation regime is of particular relevance. Because of water's high polarity, the distinction between equilibrium and nonequilibrium solvation can have very dramatic consequences on spectro-

scopic properties. As already pointed out in section 4, for RR, as well as vibrationally resolved absorption and fluorescence spectra, it is necessary to make a distinction between electronic and vibrational nonequilibrium solvation, depending on which degrees of freedom of the solvent are allowed to relax and thus remain at equilibrium with the solute evolving with a timescale characteristic of the spectroscopic phenomenon. In the framework of a time-dependent picture, the vibronic structure characteristic of any electronic excitation and the RR response arise from the evolution of the initial vibrational wavepacket on the excited state PES, which may last long enough to allow for the relaxation of the solvent's electronic (and, possibly, nuclear) degrees of freedom. The choice of the most appropriate solvation regime depends on the system and is by no means trivial. We have investigated the effect of the different approaches on RR and vibrationally resolved OPA spectra of imidazole in water by performing the calculations under the three distinct conditions described in section 4. First we considered the solvent in full equilibrium with the system, both in its electronic and nuclear degrees of freedom, then we considered the effect of keeping the PCM cavity fixed (where the vibrational nonequilibrium regime is employed in the computation of the harmonic or anharmonic vibrational ground state frequencies and normal modes), and finally we performed the calculation with the addition of electronic nonequilibrium effects on excited state properties. Note that we also included anharmonicity effects in all cases.

Electronic and nuclear nonequilibrium affects the computed spectra at different levels. Keeping the PCM cavity fixed only influences the calculation of the gradients (and, if required, Hessian and higher order derivatives) of the ground state energy and excitation energy that are used to model the PESs. Conversely, under equilibrium conditions, it is necessary to include in the derivatives additional terms accounting for the displacement of the cavity. This effect does not change the vertical energy or dipole strength of the transition (the latter accounted for by the FC terms), since neither involves any geometrical derivatives, but affects the shape of the excited-state PES and the HT and higher terms in the

Taylor expansion of the dipole moments. It should be clear that the question of the vibrational nonequilibrium does not arise in the modeling of one-photon spectroscopies (e.g. absorption and fluorescence) unless one is interested in the vibronic bandshape, but is always present in the case of RR, for which even the simplest computational models require the calculation of the excited state gradient. Electronic nonequilibrium has a more dramatic effect, as it influences the calculated vertical excitation energies and can even affect the order of the excitations. Figure 6.5 shows the computed vibronic OPA spectra, the RR excitation profile (i.e. a plot of the RR intensity against the incident frequency at a fixed Raman shift) corresponding to the 8th normal mode (an in-plane bending motion, see figure 6.4 for a pictorial representation of the normal modes mentioned throughout the article), and the RR spectrum, under the three solvation regimes discussed in section 4. All spectra were computed at the Vertical-Gradient Franck-Condon (VG|FC) level, with the inclusion of anharmonic effects. Each band in the vibronic OPA spectrum was convoluted with a Gaussian function with a HWHM of 150 cm^{-1}, while the peaks in the RR spectra were convoluted with Gaussian functions with a HWHM of 10 cm^{-1}. The RR and RR excitation profile spectra employ a value for the damping constant of 500 cm^{-1}. All spectra are shown in arbitrary units. The RR spectra were computed for an incident wavelength of 224 nm and, since we are more interested in comparing relative intensities rather than absolute ones, they were subsequently scaled to have the same maximum intensity.

All three vibronic OPA spectra show a similar convolution; the lowest energy band corresponds to the 0-0 transition, while the other bands arise mainly from the superposition of different peaks corresponding to transitions from the vibrational ground state to a combination of normal modes 11, 13, 14, and 15 in the excited state PES. The spectra show that there is only a slight change when the PCM cavity is held fixed (dashed orange line), and the resulting spectrum is almost superimposed to the spectrum obtained with a mobile cavity. The position of the peaks is expected to be almost identical in the two cases, as keeping the cavity fixed does not di-

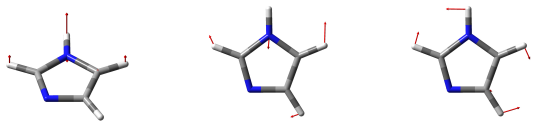

(a) Mode 1 **(b)** Mode 8 **(c)** Mode 11

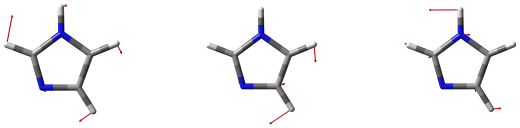

(d) Mode 13 **(e)** Mode 14 **(f)** Mode 15

Figure 6.4: Normal modes of imidazole mentioned throughout the work.

rectly affect the vertical transition energy. The same behavior is observed in the case of the RR excitation profile. The RR spectrum instead shows a much more pronounced difference: the position of the peaks is heavily influenced by the solvation regime employed to compute the ground state anharmonic frequencies, with a smaller yet clearly discernible effect on relative intensities. A much larger change can be observed in the case of the electronic nonequilibrium: in this case the vertical transition energy is blueshifted by about 1500 cm^{-1} (roughly 7.5 nm) and both the OPA spectrum and the RR excitation profile appear translated. In addition, the relative intensities of the absorption peaks are affected by the variation of the solvation regime, and the same behavior is observed in the excitation profile. The change in both intensity patterns is a consequence of the change in the computed excited-state forces under the two different solvation regimes. The RR spectrum shows a very different behavior, as there is very little change with respect to the fixed-cavity regime. The position of the peaks is a property of the ground state, therefore it is not influenced by the way excitation properties are calculated, and while a small change in the intensity pattern is noticeable, it is by no means as significant as in the case of the RR excitation profile, though this depends upon the chosen incident wavelength.

These results greatly highlight the nature of RR spectroscopy as a

mixed electronic-vibrational phenomenon which is heavily influenced by the environment and the choice of solvation regime.

6.6.3 Comparison with experiment

So far we have analyzed the effect of anharmonicity and solvation environment employing the simplest model for the vibronic transition (VG|FC). Before comparing our results with experimental data we needed to study the effect of Duschinsky mixing on the spectrum. To do so we compared the anharmonic (VH|FC) RR spectrum with the (VG|FC) one represented as a dashed orange line in figure 6.5 (whithin the fixed-cavity solvation regime). The results are represented in figure 6.6 a. Of course, peak positions are unaffected by the introduction of Duschinsky mixing, but relative intensities experience significant changes.

The comparison with experiment is complicated by the great number of parameters involved. First, one has to choose an incident frequency and a suitable damping constant, which can assume a wide range of different values. The incident frequency may be chosen to differ from the calculated vertical energy by the same amount as the experimental laser frequency differs from the measured absorption maximum.[251] If the absorption spectrum is very broad this method may not be very precise. Note also that a lower damping constant may cause the spectrum to depend more strongly upon the chosen incident frequency.[16] In addition, the solvation regime greatly affects both the vertical transition energy and the RR intensity pattern. The comparison may be greatly facilitated if both the experimental RR spectrum and RR excitation profile are available. We compare our results with experimental one by Balakrishnan et al,[260] (see figure 6.6b), who measured the RR spectrum at an excitation wavelength of 229 nm, which corresponds to the very start of the absorption band of imidazole. The comparison of the experimental spectrum with the calculated VH one (figure 6.6a) shows that peak positions are reproduced well enough to permit an assignment. The band that appears around 1100 cm^{-1} is enhanced with respect to the experimental one, while the

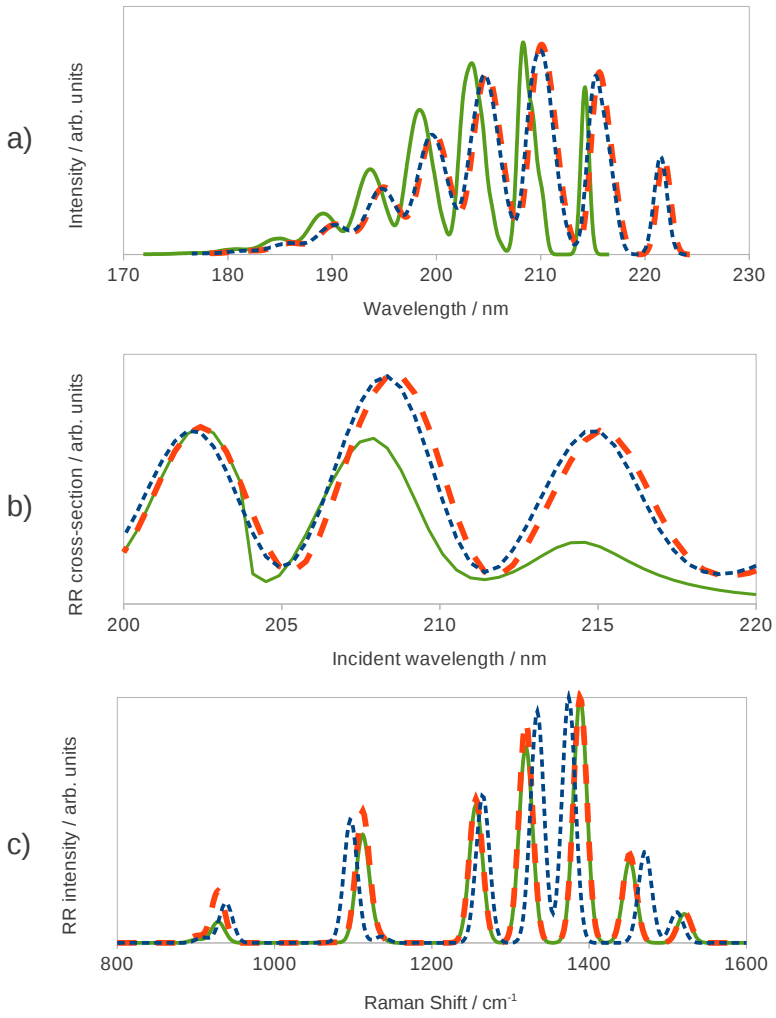

Figure 6.5: UV-Vis (Top panel), RR excitation profile (middle panel), and RR spectra (bottom panel) of imidazole in water calculated with three different solvation regimes: equilibrium solvation (finely dashed blue line), fixed cavity (dashed orange line), and nonequilibrium (continuous green line).

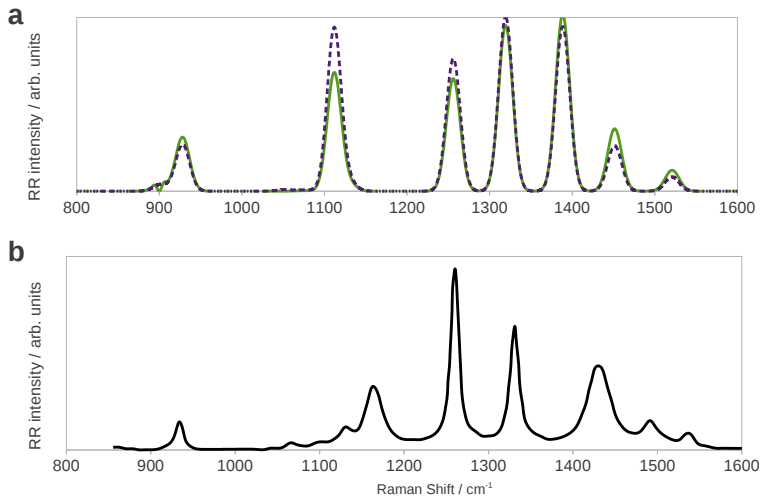

Figure 6.6: Calculated VG|FC (top, solid green line) and VH|FC (top, dashed purple line) RR spectra, and experimental[260] (bottom, black line) RR spectrum of imidazole in water.

one at 1260 cm^{-1} has a lower than expected intensity, otherwise the agreement is fairly good, and the VH spectrum shows a better agreement with experiment than the VG one, owing to the effect of Duschinsky mixing. The small peaks between 1050 cm^{-1} and 1150 cm^{-1} are in-plane bending motions of the C-H bonds;[260] they are not visible in the theoretical spectrum because of their negligible calculated intensity or because they are obscured by the higher-intensity peak at 1100 cm^{-1}. One possible source of errors may be that imidazole in water can form hydrogen bonds with solvent molecules, whose effect is not fully captured by our implicit solvation model. A way to overcome this limitation is to use atomistic models for the environment, such as the QM/FQ/PCM model we have recently implemented.[59–61] Because the experimental incident frequency is on the tail of the absorption bandshape there may also be contamination from the non-resonant Raman spectrum.

6.7 Pyrene in acetonitrile solution

The RR spectra of pyrene (D_{2h} symmetry) and its derivatives have been previously studied both experimentally[261] and theoretically.[251,262,263] In this contribution we wish to draw upon the previous work by some of us[251] and expand it by including anharmonicity and nonequilibrium solvent effects in the spectrum calculation. The interesting property of the RR spectra of pyrene is the interference between different excited states. Contrary to what happens in the case of OP spectra, in RR the contributions from different electronic states must be added at the amplitude (polarizability) level rather than at the intensity level (the Raman cross section is quadratically dependent on the polarizability). The result is that the total spectrum is not simply the sum of the spectra arising from the different electronic states. The three excited states that should be taken into consideration are, in order of increasing energy, the $1B_{1u}$, $2B_{2u}$, and $2B_{1u}$ states.[251,261] In the case of pyrene calculations we chose the intermediate solvation regime, with ground state harmonic and anharmonic frequency calculations performed with vibrational nonequilibrium effects, and we kept the cavity fixed in all calculations involving the excited states. We performed a ground state geometry optimization followed by a normal mode calculation at the PBE0/SNSD[254] level of theory. We also optimized the ground-state geometry and computed the anharmonic vibrational frequencies using the smaller 6-31G* basis set in order to obtain them at a reduced computational cost. The PBE0/SNSD harmonic frequencies were combined with the PBE0/6-31G* anharmonic shifts to obtain the anharmonic vibrational energies to be used in the subsequent RR calculations. The PBE0/6-31G* level of theory was also used for all excited-state calculations, and the model chosen for the excited PESs is AH, which requires a geometry optimization followed by harmonic frequency calculations. All RR spectra were computed using a damping constant of 500 cm^{-1} and the RR peaks were convoluted with Gaussian functions with a HWHM of 15 cm^{-1}.

As already pointed out, it is not essential to accurately reproduce the

excitation energy to compute a RR spectrum because the incident frequency used in the calculation can be easily adjusted to compensate for this error. However, whenever multiple states are involved it may be crucial to correctly reproduce the energy difference between the states. For example, a spectrum may contain peaks which are enhanced by resonance with different electronic states, and if the energy difference between those states is overestimated, it may be impossible to find an incident frequency for which all peaks are visible. A comparison between the experimental and theoretical vibronic absorption spectrum can be used to check the reliability of the chosen electronic structure model. Moreover, if the vibronic resolution is clearly visible in the experimental spectrum, the latter can be used to extract the energy of the 0-0 transitions for each electronic state, and those energies can then be employed in the calculation of the RR spectra. This is the case of pyrene, whose experimental and calculated vibronic absorption spectra are shown in figure 6.7. While the bandshapes are correctly reproduced, the calculated spectrum is not merely shifted with respect to the experimental one because the energy of the $1B_{1u}$ state is underestimated by a larger amount with respect to the $2B_{2u}$, and $2B_{1u}$ states. To compensate for this error we therefore shifted the energy of each state individually before computing the RR spectra and excitation profiles.

We also checked whether other DFT functionals or a multireference method would yield better results. We therefore computed the vertical excitation energies using the CAM-B3LYP[114] and M06-2X[119] functionals with the SNSD basis set, as well as by MS-CASPT2[255] with the ANO basis set with the contraction 4s3p1d for carbon atoms, and 2s1p for hydrogen atoms.[264,265] A full valence π space which comprised 16 electrons distributed in 16 orbitals (16,16) was used. The DFT calculations included solvent effects by means of PCM, while the MS-CASPT2 calculations were performed for the molecule in the gas phase, so we also computed the excitations with PBE0 without PCM, to estimate the solvent shift. The PBE0/SNSD ground state optimized geometry was used in all cases. The calculated vertical transition energies cannot be directly compared with

the energy of the 0-0 transition obtained from the experimental spectrum, though their difference can be estimated theoretically from the vibronic spectrum calculated with the PBE0 functional, giving 2690 cm^{-1} for the $1B_{1u}$ state, 2188 cm^{-1} for the $2B_{2u}$ state, and 2967 cm^{-1} for the $2B_{1u}$ state. These values were then subtracted from the calculated vertical excitation energies. Table 6.2 summarizes the results. M06-2X gives the best results for the excitation energies, however it has been shown that it is less reliable for calculation of harmonic frequencies,[266] therefore we still preferred to use PBE0 to compute all spectra because, as shown in figure 6.7 and in the analysis by Avila Ferrer *et al.*[251] this functional gives a very good description of the shape of the PESs. The MS-CASPT2 results do not show a significant improvement with respect to the TDDFT ones, though they lack a description of solvation effects which, as can be seen from the comparison of the gas-phase and acetonitrile solution results obtained for PBE0, give a large contribution.

Often the resolution of the experimental spectrum is not sufficient to clearly identify the energy of the 0-0 transition (especially if the states are very close in energy and their spectra overlap). In that case it may be useful to perform additional calculations with different electronic structure methods to estimate the energy differences between the excited states.

Table 6.2: Energies of the 0-0 transitions (in cm^{-1}) computed with different methods, and their experimental counterparts.[261] $PBE0_{(g)}$ denotes gas-phase excitation energies, while all other TDDFT results include solvent effects.

State	MS-CASPT2	$PBE0_{(g)}$	PBE0	CAM-B3LYP	M06-2X	Exp[261]
$1B_{1u}$	25688	27333	25773	27219	27700	29940
$2B_{2u}$	36180	35271	33761	35944	35931	36765
$2B_{1u}$	41469	40768	38328	39527	39902	41667

To show the effect of the excitation-energy shift and of anharmonicity on the RR spectrum we computed the harmonic and anharmonic spectra using the PBE0/SNSD excitation energy, as well as the anharmonic spectrum calculated using the excitation energies from experiment. We chose an incident frequency of 42000 cm^{-1} (238 nm) to compute the latter spec-

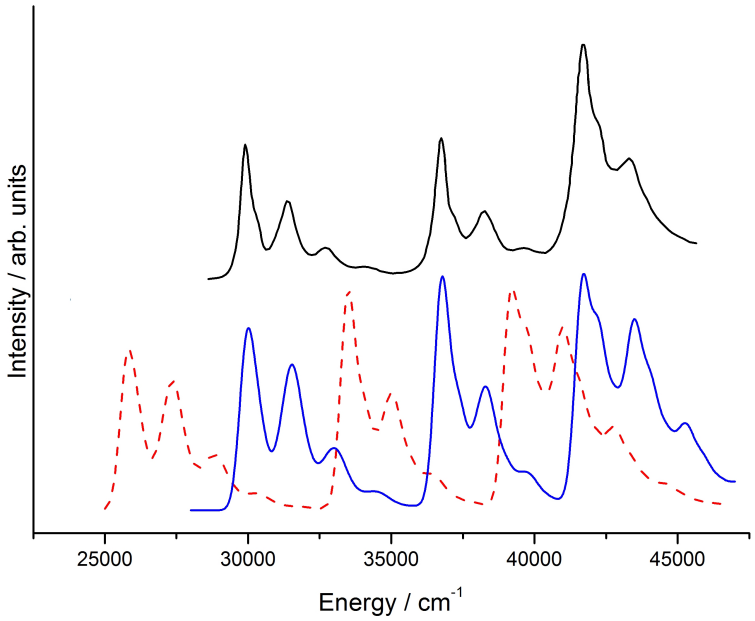

Figure 6.7: Experimental (top black line) and calculated (bottom lines) vibronic absorption spectra of pyrene in acetonitrile. The dashed red line is the unshifted spectrum (PBE0/SNSD band positions), the continuous blue line is the shifted spectrum according to the experimental transition energies.

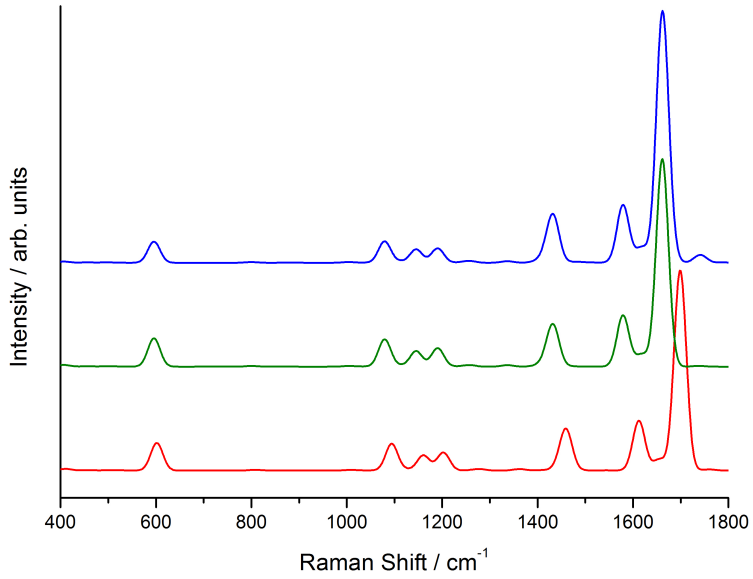

Figure 6.8: Calculated harmonic (bottom red line) and anharmonic (middle green line) RR spectra obtained using the PBE0/SNSD excitation energies, and anharmonic spectrum (top blue line) obtained using the experimental excitation energies of pyrene in acetonitrile.

trum, and an incident frequency of 39500 cm^{-1} (253 nm) to compute the two former ones (in order to adjust the energy of the $2B_{1u}$ state without touching the energy differences, as would be normally done). The incident energy is at the edge of the $2B_{1u}$ band in the experimental spectrum in figure 6.7, so it is affected by interference with the lower-energy $2B_{2u}$ state. Figure 6.8 shows the results. As in the case of imidazole, anharmonicity causes a redshift of all bands, as well as minor intensity changes. The spectrum computed using the experimental excitation energies shows an additional change in intensity, especially visible for the band that appears around 1700 cm^{-1}. This kind of effects are not very big in the case of pyrene because there is quite a large separation between the three electronic states, but they may be more relevant in cases where the energy difference between the states is grossly overestimated or underestimated by the chosen electronic structure method.

6.8 Chlorophyll a1 in methanol solution

To illustrate how our approach can be applied to larger systems we computed the RR spectrum of chlorophyll $a1$ (ChlA1, figure 6.9), a large system of 46 atoms that is often used as a model for chlorophyll a, a pigment found at the heart of the biological machinery responsible for photosynthesis.[267] RR spectroscopy has already proved to be an invaluable tool in the study of multichromophoric systems, such as those involved in photosynthesis, thanks to the possibility of tuning the incident frequency to selectively excite the different chromophores.[268,269] In this work we studied the influence of a solvent on the RR spectrum, postponing the case of more complex environments, such as proteins, to future works. We also compared our results with the experimental ones by Hanf *et al.*[270] who measured the RR spectrum of protochlorophyllide a (PChlide) in methanol solution. PChlide has an identical π structure to chlorophyll $a1$, but with additional alkylic substituents which do not significantly alter the shape of the absorption spectrum. We calculated the RR spectrum of ChlA1 in methanol solution with the inclusion of Duschinsky mixing, Herzberg-Teller, solvent, and anharmonicity effects combined (anharmonic AH|FCHT model with equilibrium solvation). The RR spectrum was calculated for the bright Soret band which appears at about 420 nm in the experimental spectrum,[271,272] and the solvation regime chosen in this case is the equilibrium one. Since the magnesium atom at the center of the ring is expected to be hexacoordinated, with one solvent molecule on either side of the ring, to overcome the limitations of the continuum solvent model we explicitly added these solvent molecules to the part of the system treated quantum-mechanically.

We first note that the dimensionality of the system requires great care in the choice of the computational level. The most demanding step in our calculations is by far the evaluation of ground state anharmonic frequencies, which is accomplished by displacing the molecular geometry along each normal mode in the positive and negative directions, computing the energy Hessian at each step, and obtaining the numerical third

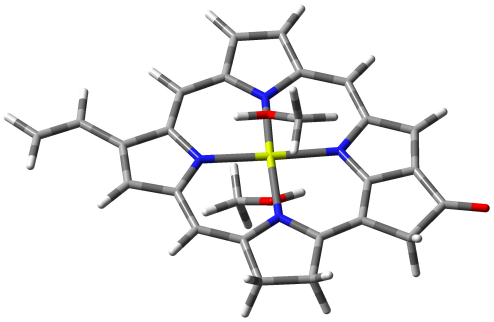

Figure 6.9: Structure of chlorophyll $a1$ with two additional methanol solvent molecules.

and semi-diagonal fourth energy derivatives. The computational cost of this approach scales unfavorably with system size (even though the calculations can be done in parallel if multiple machines are available). Similarly to what was reported for pyrene, we employed the SNSD[254] basis set to compute the harmonic frequencies while resorting to the smaller 6-31G* basis set to compute the anharmonic shifts. In the case of ChlA1, even with the smaller basis set, the full anharmonic calculation is computationally too expensive so, to further reduce its cost, we resorted to a reduced-dimensionality approach,[238,239] limiting the evaluation of the required anharmonic derivatives to the normal modes in the 1100-1800 cm^{-1} region, and thus restricting the computed RR spectrum as well. The reduced-dimensionality approach is especially useful for the calculation of anharmonic RR spectra because it is always possible to focus on the frequency region in which the final RR spectrum is to be computed, while for vibronic OP spectra this is not possible. Restricting the calculation to a smaller region also saves time in the subsequent TI-RR spectrum calculation, though it must be emphasized that, notwithstanding the large number of peaks and the great number of states included in the TI expression for each peak, this is still the cheapest step in the overall calculation. To present this last point in deeper detail we show in figure 6.10a the relative computational times for each step leading to the final spectrum. Note that, even with a reduced-dimensionality approach, the most expen-

sive step is by far the calculation of anharmonic frequencies, followed by the calculation of excited state frequencies. Anharmonicity and Duschinsky effects can sometimes be ignored, but the calculation of ground state frequencies is essential for vibrational spectroscopies and it is still more expensive than the final spectrum calculation. Note in addition that in figure 6.10a we report the time needed to obtain the RR spectrum in the selected spectral region with the inclusion of first overtones and combination bands (the calculation of the fundamental bands only is in fact so cheap that it would not be visible in the reported pie chart). Thanks to our parallel implementation we are able to compute the RR spectrum of medium-large systems with a reasonable cost, and the limiting factor is represented by all other steps that are necessary to define the two PESs. Figure 6.10b shows the relative computational time required for the TI-RR spectrum calculation as a function of the number of processors used. The computational gain is close to the maximum theoretically possible: with 8 processors the computational time is reduced to 15.4% (as opposed to ⅛=12.5%).

Before computing the RR spectrum, we simulated the vibronic bandshape of the UV-vis absorption spectrum in order to assess the quality of our approach for the specific system. A TD-DFT vertical excitation energy calculation reveals that the band we are interested in is a superposition of two different $\pi - \pi^*$ excited states, S_3 (HOMO-1–LUMO+1) and S_4 (HOMO–LUMO+1). The S_1 (HOMO–LUMO) and S_2 (HOMO-1–LUMO) states, have lower intensity and calculated vertical excitation wavelengths of 637 nm and 618 nm respectively. Figure 6.11 shows a graphical representation of the Kohn-Sham orbitals involved in the transitions.

Figure 6.12 shows the comparison between the experimental spectra of PChlide[270] and ChlA1[271] and the calculated vibronic spectrum of ChlA1, which was obtained by convoluting each peak with a Gaussian function with a HWHM of 250 cm^{-1}. For both electronic states that appear in the calculated spectrum, the band with highest intensity corresponds to the 0-0 transition, and both show a similar vibronic progression, which

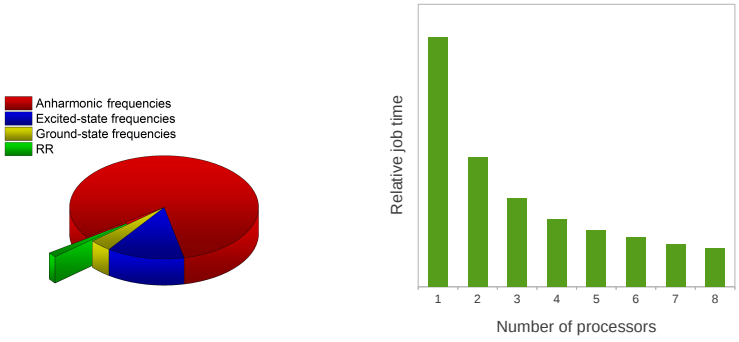

(a) **(b)**

Figure 6.10: (a) Relative computational cost of the different steps leading to the final RR spectrum of ChlA1. Ground state frequencies (SNSD basis set) are in blue, anharmonic shifts (6-31G* basis set) are in orange, excited state frequencies (6-31G* basis set) are in yellow, and the final RR spectrum between 1100 and 1800 cm^{-1}, up to the first overtones and 1+1 combination bands is in green. (b) Relative cost of the RR spectrum calculation with increasing number of processors.

is due to the excitation of several very diffuse in-plane bending motions. The experimental spectra of PChlide and ChlA1 show a similar band-shape which justifies the use of the latter as a model for the former in the calculation of the RR spectrum. The calculated band-shape reproduces experiment fairly well, even though DFT predicts the two excited states to be further apart than they would appear from the experimental spectrum. The calculated spectrum almost overlaps with the experimental PChlide one, with the maximum appearing at 434 nm and 437 nm in the experimental and calculated spectrum, respectively, whereas the maximum of the experimental ChlA1 spectrum appears at 417 nm. Overall, the chosen model seems appropriate for the description of our system.

Figure 6.14 shows the calculated and experimental[270] RR spectra. The calculations were performed with an incident frequency of 24550 cm^{-1} (407 nm), and a damping constant of 500 cm^{-1}. The experimental spectrum of PChlide was also recorded with a 407 nm incident radiation. Because the calculated ChlA1 UV-vis spectrum overlaps with the exper-

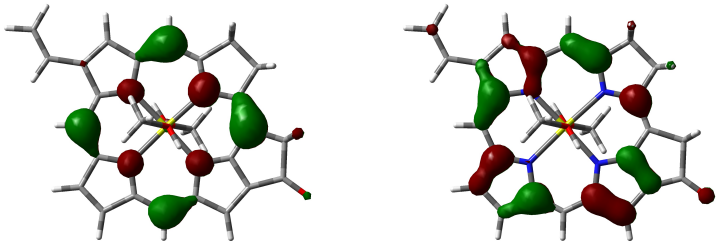

(a) HOMO-1 **(b)** HOMO

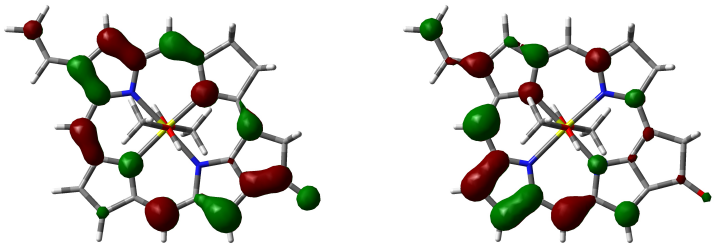

(c) LUMO **(d)** LUMO+1

Figure 6.11: Kohn-Sham orbitals of chlorophyll $a1$.

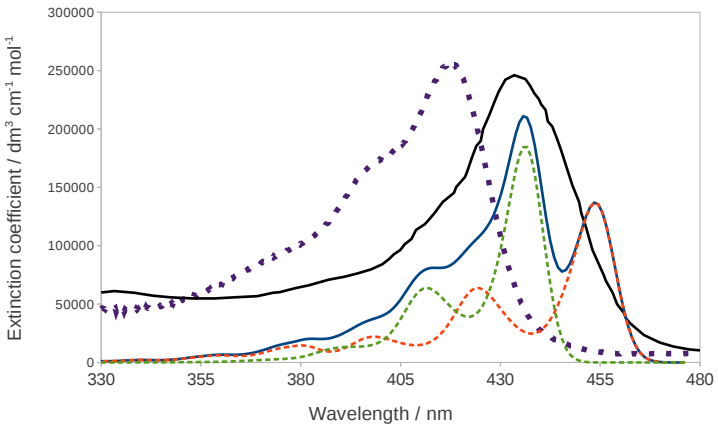

Figure 6.12: Calculated (continuous blue line) and experimental[271] (dotted purple line) absorption spectra of ChlA1 in methanol. The continuous black line is the experimental absorption spectrum of PChlide,[270] and the dashed orange and green lines are the calculated absorption spectra for the S_3 and S_4 states respectively.

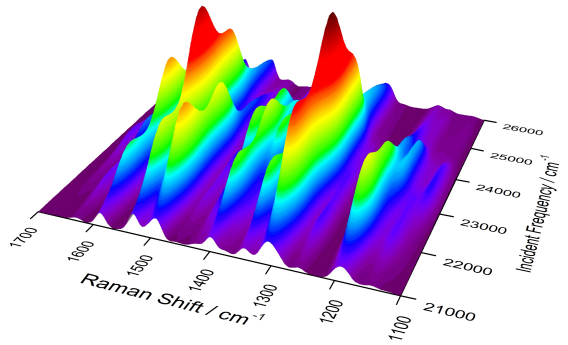

Figure 6.13: Calculated 2D-RR spectrum of ChlA1 in methanol, where the spectrum and excitations profiles are shown at the same time.

imental PChlide one, we did not need to apply any shift to the incident frequency. The peaks were convoluted with Gaussian functions with a HWHM of 10 cm^{-1}. The top and middle panels show the harmonic and anharmonic spectra, respectively. As already reported for imidazole, the effect of anharmonicity mainly consists of a redshift of all bands but, because the shift is different for each peak, the convoluted spectrum also shows some clearly visible differences in the bandshape. Figure 6.14 also shows the separate contribution of each excited state: the S_4 state gives a greater contribution, as is expected from its greater intensity in the absorption spectrum and from the fact that it lies closer to the incident frequency. The S_3 state still gives a non-negligible contribution thanks to the fact that the tail in its absorption spectrum reaches the value of the incident frequency. As explained above, the total spectrum is not simply the sum of the two separate spectra because of interference effects acting at the polarizability level. We also computed the spectrum with the inclusion of overtones and combination bands of up to two quanta transitions, but we found that they all have negligible intensities resulting in an almost identical spectrum.

The bottom panel in figure 6.14 shows for comparison the experimental spectrum of PChlide recorded with a 407 nm laser frequency.[270] The experimental spectrum shows a strong band around 1360 cm^{-1} which the au-

thors assign to C-C breathing vibrations of the porphyrin, a band around 1570 cm^{-1} assigned to C=C stretching vibrations, and one at 1700 cm^{-1} assigned to the C=O bending of the ciclopentanone ring. These features are all reproduced in the calculated spectrum, though with notable differences. The computed frequencies are lower than the experimental ones, causing a shift of the whole spectrum. The 1400 cm^{-1} zone in the computed spectrum shows a few bands of significant intensities, which correspond to very diffuse C=C bendings, that are not observed in the experimental spectrum. The high-intensity peaks that appear between 1500 and 1600 cm^{-1} in the anharmonic calculated spectrum are due to C=C stretching motions and they are separated by a gap which is not found in the experimental spectrum, but our calculations reveal that there are actually no normal modes with an energy that would place them whithin that gap. These differences may be attributed to the additional side chains of PChlide, which would result in a greater number of peaks.

The effect of changing the incident frequency can be grasped by looking at the 3D plot in figure 6.13, where the axes hold the Raman shift, incident frequency, and spectrum intensity. The behavior of the different bands seems irregular because the two excited states affect the various peaks in different ways, and their large number means that they often overlap to give rise to the visible bands. The potential interpretative power of theoretical calculation is then evident as it can help to unravel complex spectroscopic responses such as RR which, as an additional complication, does not benefit from the simple selection rules valid for non-resonant Raman scattering.

6.9 Conclusions and perspectives

In this work we have presented a parallel implementation of the TI calculation of RR spectra with the inclusion of anharmonicity and solvent effects. We have shown that it is possible, by carefully choosing the computational methods and employing appropriate reduced-dimensionality schemes, to coherently include anharmonicity, Duschinsky, and solvent effects in the

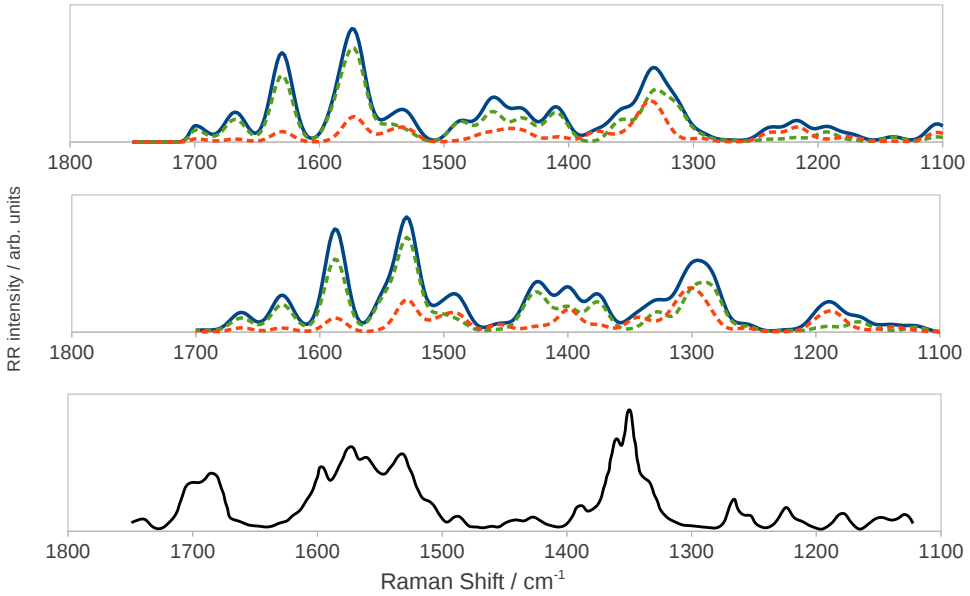

Figure 6.14: Harmonic (top panel) and anharmonic (middle panel) RR spectra of ChlA1 in methanol. The continuous blue line is the total spectrum, the dashed orange and green lines the spectra for the S_3 and S_4 states respectively. The bottom panel shows the experimental RR spectrum of PChlide.[270]

calculation of RR spectra of medium-to-large sized systems. We have demonstrated that the cost of the calculations required to accurately model the ground-state and excited-state PESs far outweighs the simulation of the final TI-RR spectrum, therefore the best way to extend the applicability of the method to ever-larger systems is to find cheaper means to perform the former tasks. This goal may be accomplished through analytic implementations of excited state energy second derivatives,[273,274] which scale very favorably with system size with respect to their numerical counterparts, and through the use of less expensive methods such as semi-empirical ones, especially for the evaluation of anharmonic frequencies.[275]

With the goal of extending the method to larger and more complex systems, another issue calling for deeper investigations is the choice of internal coordinates for the simultaneous description of electronic states possibly characterized by quite different geometries. Several studies have shown that normal modes built from Cartesian coordinates represent the most straightforward and robust choice when small displacements occur. In such circumstances the full adiabatic Hessian (AH) model, possibly including leading anharmonic corrections, shows a remarkable agreement with experiment, provided that the quantum mechanical method chosen to build the PES is accurate enough. When large structural displacements take place between the different electronic states, the situation is more involved, especially if inversions and/or torsions are present.[276] Recent works suggest that in such circumstances Cartesian coordinates face significant difficulties for a correct description of curvilinear displacements and a proper account of the Duschinsky mixing within the AH model, where the PESs of the different electronic states are quadratically expanded around their own equilibrium geometry.[276–278] Although the theory behind the use of internal coordinates is well known[276] and several works have been published concerning specific systems,[277,278] a general implementation of this model is still lacking and is one of the most important tasks on which our group is concentrating its efforts. On the other hand, the good agreement between the results issuing from the vertical Hessian (VH) model

and experimental line shapes indicates that this approximation, in which all the normal modes are evaluated at the equilibrium geometry of a single reference electronic state, is a good alternative to deal with systems exhibiting large displacements. The use of this model can be, however, problematic when imaginary frequencies arise.[279]

Motivated by the fact that there is a well-known strong relationship between the RR spectral response and the molecular environment, we have also studied the effect of the solvation regime on the final spectrum. We have employed three different solvation regimes with the intent of modeling the behavior of the different degrees of freedom of the solvent as they either remain fixed or equilibrate with the time-dependent evolution of the starting vibrational wavepacket of the solute that generates the spectral response, according to their characteristic timescales. It should be noted that the different solvation regimes we have considered can be viewed as limiting cases of the real behavior of the solvent: in reality the solvent's degrees of freedom always start from a nonequilibrium situation, and then, if the lifetime of the vibrational wavepacket on the excited state PES is long enough to allow it, they gradually evolve to re-equilibrate with the solute. Nonetheless, our results show that the change in the solvation regime does have a great influence on the final RR spectrum and excitation profile, which could stimulate more research in this area. In particular, by performing the calculation in the time-dependent picture, it could be possible to model the evolution of the solvent's polarization more accurately by considering an additional time-dependence of all the terms in the equation caused by the solvent, though the assessment of how the solvent's evolution affects the excited state PES and the transition moments is far from trivial. The choice of the appropriate solvation regime may be particularly important in the case of more complex environments, such as a chromophore embedded in a protein, which cannot freely rearrange itself to adapt to the evolution of the chromophore. In this case though, implicit solvent models may fail to capture the specificity of the interactions, therefore atomistic models may be more appropriate. A possible strategy to overcome such limitations can be the hybrid multi-scale QM/FQ/PCM

scheme[59–61] we have recently proposed, to treat explicit interactions between a molecular system and its environment. An additional limitation of the implicit model used in this work is the absence of non-electrostatic effects in the solvent response in its basic formulation. Several methods have been proposed to include non-electrostatic effects within the PCM framework,[43,44,46] though, to the best of our knowledge, none have been applied to RR spectroscopy.

Bibliography

[1] Egidi, F.; Giovannini, T.; Piccardo, M.; Bloino, J.; Cappelli, C.; Barone, V. Stereo-electronic, vibrational, and environmental contributions to polarizabilities of large molecular systems: a feasible anharmonic protocol. *J. Chem. Theory Comput.* **2014**, *10*, 2456–2464.

[2] Egidi, F.; Bloino, J.; Cappelli, C.; Barone, V. Development of a Virtual Spectrometer for Chiroptical Spectroscopies: The Case of Nicotine. *Chirality* **2013**, *25*, 701–708.

[3] Egidi, F.; Bloino, J.; Cappelli, C.; Barone, V. A robust and effective time-independent route to the calculation of Resonance Raman spectra of large molecules in condensed phases with the inclusion of Duschinsky, Herzberg-Teller, anharmonic, and environmental effects. *J. Chem. Theory Comput.* **2014**, *10*, 346–363.

[4] Egidi, F.; Bloino, J.; Cappelli, C.; Barone, V.; Tomasi, J. Tuning of NMR and EPR parameters by vibrational averaging and environmental effects: an integrated computational approach. *Mol. Phys.* **2013**, *111*, 1345–1354.

[5] Egidi, F.; Bloino, J.; Barone, V.; Cappelli, C. Toward an Accurate Modeling of Optical Rotation for Solvated Systems: Anharmonic Vibrational Contributions Coupled to the Polarizable Continuum Model. *J. Chem. Theory Comput.* **2012**, *8*, 585–597.

[6] Lipparini, F.; Egidi, F.; Cappelli, C.; Barone, V. The Optical Rotation of Methyloxirane in Aqueous Solution: A Never Ending Story? *J. Chem. Theory Comput.* **2013**, *9*, 1880–1884.

[7] Long, D. A. *The Raman Effect: A Unified Treatment of the Theory of Raman Scattering by Molecules*; John Wiley & Sons Ltd : New York, 2002.

[8] Raman, C. V.; Krishnan, K. S. A New Type of Secondary Radiation. *Nature* **1928**, *121*, 501–502.

[9] Craig, D. P.; Thirunamachandran, T. *Molecular Quantum Electrodynamics*; Dover Books on Chemistry; Dover Publications; Unabridged edition, 1998.

[10] Barron, L. *Molecular Light Scattering and Optical Activity*, 2nd ed.; Cambridge University Press: New York, 2004.

[11] McWeeny, R. *Methods of Molecular Quantum Mechanics*, 2nd ed.; Academic Press, 1992.

[12] Andrews, S. S. Using Rotational Averaging To Calculate the Bulk Response of Isotropic and Anisotropic Samples from Molecular Parameters. *J. Chem. Ed.* **2004**, *135*, 877–885.

[13] Hecht, L.; Nafie, L. A. Theory of natural Raman Optical Activity Part I. Complete circular polarization formalism. *Mol. Phys.* **1991**, *72*, 441–469.

[14] Barone, V.; Bloino, J.; Biczysko, M.; Santoro, F. Fully Integrated Approach to Compute Vibrationally Resolved Optical Spectra: From Small Molecules to Macrosystems. *J. Chem. Theory Comput.* **2009**, *5*, 540–554.

[15] Bloino, J.; Biczysko, M.; Santoro, F.; Barone, V. General Approach to Compute Vibrationally Resolved One-Photon Electronic Spectra. *J. Chem. Theory Comput.* **2010**, *6*, 1256–1274.

[16] Santoro, F.; Cappelli, C.; Barone, V. Effective Time-Independent Calculations of Vibrational Resonance Raman Spectra of Isolated and Solvated Molecules Including Duschinsky and Herzberg-Teller Effects. *J. Chem. Theory Comput.* **2011**, *7*, 1824–1839.

[17] Aliev, M.; Watson, J. In *Molecular spectroscopy: modern research*; Rao, N. K., Ed.; Academic Press, 1985; pp 1–67.

[18] Papoušek, D.; Aliev, M. *Molecular vibrational-rotational spectra*; Elsevier, 1982.

[19] Nielsen, H. H. The vibration-rotation energies of molecules. *Rev. Mod. Phys.* **1951**, *23*, 90–136.

[20] Barone, V. Accurate Vibrational Spectra of Large Molecules by Density Functional Computations beyond the Harmonic Approximation: The Case of Azabenzenes. *J. Phys. Chem. A* **2004**, *108*, 4146–4150.

[21] Barone, V. Anharmonic vibrational properties by a fully automated second-order perturbative approach. *J. Chem. Phys.* **2005**, *122*, 014108.

[22] Amos, R. D.; Handy, N. C.; Green, W. H.; Jayatilaka, D.; Willets, A.; Palmieri, P. Anharmonic vibrational properties of CH_2F_2: A comparison of theory and experiment. *J. Chem. Phys* **1991**, *95*, 8323.

[23] Kuhler, K. M.; Truhlar, D. G.; Isaacson, A. D. General method for removing resonance singularities in quantum mechanical perturbation theory. *J. Chem. Phys.* **1996**, *104*, 4664–4671.

[24] Daněček, P.; Bouř, P. Comparison of the numerical stability of methods for anharmonic calculations of vibrational molecular energies. *J. Comput. Chem.* **2007**, *28*, 1617–1624.

[25] Bloino, J.; Biczysko, M.; Barone, V. General Perturbative Approach for Spectroscopy, Thermodynamics, and Kinetics: Methodological Background and Benchmark Studies. *J. Chem. Theory Comput.* **2012**, *8*, 1015–1036.

[26] Helgaker, T.; Coriani, S.; Jørgensen, P.; Kristensen, K.; Olsen, J.; Ruud, K. Recent Advances in Wave Function-Based Methods of Molecular-Property Calculations. *Chem. Rev.* **2012**, *112*, 543–631.

[27] Bishop, D. M.; Norman, P. In *Handbook of Advanced Electronic and Photonic Materials and Devices*; Nalwa, H. S., Ed.; Academic Press, 2001; pp 1–62.

[28] Cappelli, C.; Lipparini, F.; Bloino, J.; Barone, V. Towards an accurate description of anharmonic infrared spectra in solution within the polarizable continuum model: Reaction field, cavity field and nonequilibrium effects. *J. Chem. Phys.* **2011**, *135*, 104505.

[29] Bloino, J.; Barone, V. A second-order perturbation theory route to vibrational averages and transition properties of molecules: General formulation and application to infrared and vibrational circular dichroism spectroscopies. *J. Chem. Phys.* **2012**, *136*, 124108.

[30] Barone, V.; Bloino, J.; Guido, C. A.; Lipparini, F. A fully automated implementation of VPT2 Infrared intensities. *Chem. Phys. Lett.* **2010**, *496*, 157–161.

[31] Cappelli, C.; Bloino, J.; Lipparini, F.; Barone, V. Towards Ab-Initio Anharmonic Vibrational circular dichroism spectra in the condensed phase. *J. Phys. Chem. Lett.* **2012**, *3*, 1766–1773.

[32] Tomasi, J.; Persico, M. Molecular Interactions in Solution: An Overview of Methods Based on Continuous Distributions of the Solvent. *Chem. Rev.* **1994**, *94*, 2027–2094.

[33] Š. Miertus,; Scrocco, E.; Tomasi, J. Electrostatic interaction of a solute with a continuum. *Chem. Phys.* **1981**, *55*, 117–129.

[34] Cramer, C. J.; Truhlar, D. G. Implicit Solvation Models: Equilibria, Structure, Spectra, and Dynamics. *Chem. Rev.* **1999**, *99*, 2161–2200.

[35] Tomasi, J.; Mennucci, B.; Cammi, R. Quantum Mechanical Continuum Solvation Models. *Chem. Rev.* **2005**, *105*, 2999–3093.

[36] Mennucci, B. Polarizable Continuum Model. *WIREs Comput. Mol. Sci.* **2012**, *2*, 386–404.

[37] Cancès, E.; Mennucci, B.; Tomasi, J. A new integral equation formalism for the polarizable continuum model: Theoretical background and applications to isotropic and anisotropic dielectrics. *J. Chem. Phys.* **1997**, *107*, 3032–3041.

[38] Cancès, E.; Mennucci, B. The escaped charge problem in solvation continuum models. *J. Chem. Phys.* **2001**, *115*, 6130–6135.

[39] Scalmani, G.; Frisch, M. J. Continuous surface charge polarizable continuum models of solvation. I. General formalism. *J. Chem. Phys.* **2010**, *132*, 114110–114114.

[40] Lipparini, F.; Stamm, B.; amd Yvon Maday, E. C.; Mennucci, B. Fast Domain Decomposition Algorithm for Continuum Solvation Models: Energy and First Derivatives. *J. Chem. Theory Comput.* **2013**, *9*, 3637–3648.

[41] Cappelli, C.; Mennucci, B.; Monti, S. Environmental Effects on the Spectroscopic Properties of Gallic Acid: A Combined Classical and

Quantum Mechanical Study. *J. Phys. Chem. A* **2005**, *109*, 1933–1943.

[42] Cappelli, C.; Mennucci, B. Modeling the Solvation of Peptides. The Case of (*S*)-N-Acetylproline Amide in Liquid Water. *J. Phys. Chem. B* **2008**, *112*, 3441–3450.

[43] Amovilli, C.; Mennucci, B. Self-Consistent-Field Calculation of Pauli Repulsion and Dispersion Contributions to the Solvation Free Energy in the Polarizable Continuum Model. *J. Phys. Chem. B* **1997**, *101*, 1051–1057.

[44] Weijo, V.; Mennucci, B.; Frediani, L. Toward a General Formulation of Dispersion Effects for Solvation Continuum Models. *J. Chem. Theory Comput.* **2010**, *6*, 3358–3364.

[45] Marenich, A. V.; Cramer, C. J.; Truhlar, D. G. Universal solvation model based on solute electron density and a continuum model of the solvent defined by the bulk dielectric constant and atomic surface tensions. *J. Phys. Chem. B* **2009**, *113*, 6378–6396.

[46] Cammi, R.; Cappelli, C.; Mennucci, B.; Tomasi, J. Calculation and analysis of the harmonic vibrational frequencies in molecules at extreme pressure: Methodology and diborane as a test case. *J. Chem. Phys.* **2012**, *137*, 154112.

[47] Cappelli, C.; Corni, S.; Mennucci, B.; Cammi, R.; Tomasi, J. Vibrational Circular Dichroism within the Polarizable Continuum Model: A Theoretical Evidence of Conformation Effects and Hydrogen Bonding for (S)-(-)-3-Butyn-2-ol in CCl_4 Solution. *J. Phys. Chem. A* **2002**, *106*, 12331–12339.

[48] Mennucci, B. Hydrogen Bond versus Polar Effects: An Ab Initio Analysis on n-π^* Absorption Spectra and N Nuclear Shieldings of Diazines in Solution. *J. Am. Chem. Soc.* **2002**, *124*, 1506–1515.

[49] Brancato, G.; Rega, N.; Barone, V. Microsolvation of uracil anion radical in aqueous solution: a QM/MM study. *Chem. Phys. Lett.* **2010**, *500*, 104–110.

[50] Rega, N.; Cossi, M.; Barone, V. Structure and Magnetic Properties of Glycine Radical in Aqueous Solution at Different pH Values. *J. Am. Chem. Soc.* **1998**, *120*, 5723–5732.

[51] Aidas, K.; Møgelhøj, A.; Nielsen, C. B.; Mikkelsen, K. V.; Ruud, K.; Christiansen, O.; Kongsted, J. Solvent Effects on NMR Isotropic Shielding Constants. A Comparison between Explicit Polarizable Discrete and Continuum Approaches. *J. Phys. Chem. A* **2007**, *111*, 4199–4210.

[52] Hopmann, K. H.; Ruud, K.; Pecul, M.; Kudelski, A.; Dračínský, M.; Bouř, P. Explicit versus Implicit Solvent Modeling of Raman Optical Activity Spectra. *J. Phys. Chem. B* **2011**, *115*, 4128–4137.

[53] Curutchet, C.; Muñoz-Losa, A.; Monti, S.; Kongsted, J.; Scholes, G. D.; Mennucci, B. Electronic Energy Transfer in Condensed Phase Studied by a Polarizable QM/MM Model. *J. Chem. Theory Comput.* **2009**, *5*, 1838–1848.

[54] Steindal, A. H.; Ruud, K.; Frediani, L.; Aidas, K.; Kongsted, J. Excitation Energies in Solution: The Fully Polarizable QM/MM/PCM Method. *J. Phys. Chem. B* **2011**, *115*, 3027–3037.

[55] Schwabe, T.; Olsen, J. M. H.; Sneskov, K.; Kongsted, J.; Christiansen, O. Solvation Effects on Electronic Transitions: Exploring the Performance of Advanced Solvent Potentials in Polarizable Embedding Calculations. *J. Chem. Theory Comput.* **2011**, *7*, 2209–2217.

[56] Nielsen, C. B.; Christiansen, O.; Mikkelsen, K. V.; Kongsted, J. Density functional self-consistent quantum mechanics/molecular mechanics theory for linear and nonlinear molecular properties: Applications to solvated water and formaldehyde. *J. Chem. Phys.* **2007**, *126*, 154112.

[57] Brancato, G.; Rega, N.; Barone, V. A hybrid explicit/implicit solvation method for first-principle molecular dynamics simulations. *J. Chem. Phys.* **2008**, *128*, 144501.

[58] Brancato, G.; Barone, V.; Rega, N. Theoretical modeling of spectroscopic properties of molecules in solution: toward an effective dynamical discrete/continuum approach. *Theor. Chem. Acc.* **2007**, *117*, 1001–1015.

[59] Lipparini, F.; Barone, V. Polarizable Force Fields and Polarizable Continuum Model: A Fluctuating Charges/PCM Approach. 1. Theory and Implementation. *J. Chem. Theory Comput.* **2011**, *7*, 3711–3724.

[60] Lipparini, F.; Cappelli, C.; Barone, V. Linear Response Theory and Electronic Transition Energies for a Fully Polarizable QM/Classical Hamiltonian. *J. Chem. Theory Comput.* **2012**, *8*, 4153–4165.

[61] Lipparini, F.; Cappelli, C.; Scalmani, G.; De Mitri, N.; Barone, V. Analytical First and Second Derivatives for a Fully Polarizable QM/Classical Hamiltonian. *J. Chem. Theory Comput.* **2012**, *8*, 4270–4278.

[62] Lipparini, F.; Cappelli, C.; Barone, V. A gauge invariant multiscale approach to magnetic spectroscopies in condensed phase: general three-layer model, computational implementation and pilot applications. *J. Chem. Phys.* **2013**, *138*, 234108.

[63] Cammi, R. *Molecular Response Functions for the Polarizable Continuum Model*; Springer, 2013.

[64] Cammi, R.; Tomasi, J. Analytical derivatives for molecular solutes. I. Hartree-Fock energy first derivatives with respect to external parameters in the polarizable continuum model. *J. Chem. Phys.* **1994**, *100*, 7495–7502.

[65] Cammi, R.; Tomasi, J. Analytical derivatives for molecular solutes. II. Hartree-Fock energy first and second derivatives with respect to nuclear coordinates. *J. Chem. Phys.* **1994**, *101*, 3888–3897.

[66] Cancès, E.; Mennucci, B. Analytical derivatives for geometry optimization in solvation continuum models. I. Theory. *J. Chem. Phys.* **1998**, *109*, 249–259.

[67] Cancès, E.; Mennucci, B.; Tomasi, J. Analytical derivatives for geometry optimization in solvation continuum models. II. Numerical applications. *J. Chem. Phys.* **1998**, *109*, 260–266.

[68] Cancès, E.; Mennucci, B.; Tomasi, J. Analytical free energy second derivatives with respect to nuclear coordinates: Complete formulation for electrostatic continuum solvation models. *J. Chem. Phys.* **1998**, *110*, 6858–6870.

[69] Rivail, J.-L.; Rinaldi, D.; Dillet, V. Solvent effects in infrared spectroscopy a computational approach. *Mol. Phys.* **1996**, *113*, 1521–1529.

[70] Cammi, R.; Cappelli, C.; Corni, S.; Tomasi, J. On the Calculation of Infrared Intensities in Solution within the Polarizable Continuum Model. *J. Phys. Chem. A* **2000**, *104*, 9874–9879.

[71] Cappelli, C.; Corni, S.; Cammi, R.; Mennucci, B.; Tomasi, J. Nonequilibrium formulation of infrared frequencies and intensities in solution. *J. Chem. Phys.* **2000**, *113*, 11270–11279.

[72] Cappelli, C.; Corni, S.; Tomasi, J. Electronic and vibrational dynamic solvent effects on Raman spectra. *J. Chem. Phys.* **2001**, *115*, 5531–5535.

[73] Corni, S.; Cappelli, C.; Cammi, R.; Tomasi, J. Theoretical Approach to the Calculation of Vibrational Raman Spectra in Solution within the Polarizable Continuum Model. *J. Phys. Chem. A* **2001**, *105*, 8310–8316.

[74] Corni, S.; Cappelli, C.; Del Zoppo, M.; Tomasi, J. Prediction of Solvent Effects on Vibrational Absorption Intensities and Raman Activities in Solution within the Polarizable Continuum Model: A Study on Push-Pull Molecules. *J. Phys. Chem. A* **2003**, *107*, 10261–10271.

[75] Pecul, M.; Lamparska, E.; Cappelli, C.; Frediani, L.; Ruud, K. Solvent Effects on Raman Optical Activity Spectra Calculated Using the Polarizable Continuum Model. *J. Phys. Chem. A* **2006**, *110*, 2807–2815.

[76] Cammi, R.; Cossi, M.; Mennucci, B.; Tomasi, J. Analytical Hartree-Fock calculation of the dynamical polarizabilities α, β, and γ of molecules in solution. *J. Chem. Phys.* **1996**, *105*, 10556–10564.

[77] Cammi, R.; Mennucci, B.; Tomasi, J. An Attempt To Bridge the Gap between Computation and Experiment for Nonlinear Optical Properties: Macroscopic Susceptibilites in Solution. *J. Phys. Chem. A* **2000**, *104*, 4690–4698.

[78] Cappelli, C.; Mennucci, B.; Cammi, R.; Rizzo, A. Quantum Mechanical Polarizable Continuum Model Approach to the Kerr Effect of Pure Liquids. *J. Phys. Chem. B* **2005**, *109*, 18706–18714.

[79] Ferrighi, L.; Frediani, L.; Cappelli, C.; Sałek, P.; Ågren, H.; Helgaker, T.; Ruud, K. Density-functional-theory study of the electric-field-induced second harmonic generation (EFISHG) of push-pull phenylpolyenes in solution. *Chem. Phys. Lett.* **2006**, *425*, 267–272.

[80] Ferrighi, L.; Frediani, L.; Ruud, K. Degenerate Four-Wave Mixing in Solution by Cubic Response Theory and the Polarizable Continuum Model. *J. Phys. Chem. B* **2007**, *111*, 8965–8973.

[81] Cammi, R. The Hartree–Fock calculation of the magnetic properties of molecular solutes. *J. Chem. Phys.* **1998**, *109*, 3185–3196.

[82] Cammi, R.; Mennucci, B.; Tomasi, J. Nuclear magnetic shieldings in solution: Gauge invariant atomic orbital calculation using the polarizable continuum model. *J. Chem. Phys.* **1999**, *110*, 7627–7638.

[83] Ruud, K.; Frediani, L.; Cammi, R.; Mennucci, B. Solvent Effects on the Indirect Spin–Spin Coupling Constants of Benzene: The DFT-PCM Approach. *Int. J. Mol. Sci.* **2003**, *4*, 119–134.

[84] Mennucci, B.; Martínez, J. M.; Tomasi, J. Solvent Effects on Nuclear Shieldings: Continuum or Discrete Solvation Models To Treat Hydrogen Bond and Polarity Effects? *J. Phys. Chem. A* **2001**, *105*, 7287–7296.

[85] Jansík, B.; Rizzo, A.; Frediani, L.; Ruud, K.; Coriani, S. Combined density functional/polarizable continuum model study of magnetochiral birefringence: Can theory and experiment be brought to agreement? *J. Chem. Phys.* **2006**, *125*, 234105.

[86] Rinkevicius, Z.; Telyatnyk, L.; Vahtras, O.; Ruud, K. Electronic g-tensors of solvated molecules using the polarizable continuum model. *J. Chem. Phys.* **2004**, *121*, 5051.

[87] Cammi, R.; Tomasi, J. Nonequilibrium solvation theory for the polarizable continuum model: A new formulation at the SCF level with application to the case of the frequency-dependent linear electric response function. *Int. J. Quantum Chem.* **1995**, *56*, 465–474.

[88] Sanchez, M. L.; Aguilar, M. A.; Olivares del Valle, F. J. Solvent Effects on Optical Emission and Absorption Spectra: Theoretical Calculation of the 1(n,.pi.) Transition of Formaldehyde in Solution. *J. Phys. Chem.* **1995**, *99*, 15758–15764.

[89] Mennucci, B.; Cammi, R.; Tomasi, J. Excited states and solvatochromic shifts within a nonequilibrium solvation approach. *J. Chem. Phys.* **1998**, *109*, 2798–2807.

[90] Cossi, M.; Barone, V. Time-dependent density functional theory for molecules in liquid solutions. *J. Chem. Phys.* **2001**, *115*, 4708–4717.

[91] Onsager, L. Electric Moments of Molecules in Liquids. *J. Am. Chem. Soc.* **1936**, *58*, 1486–1493.

[92] Pipolo, S.; Corni, S.; Cammi, R. The cavity electromagnetic field within the polarizable continuum model of solvation. *J. Chem. Phys.* **2014**, *140*, 164114.

[93] Segeistein, D. J. The complex refractive index of water. Ph.D. thesis, University of Missouri-Kansas City, 1981.

[94] Dalton, L. *Polymers for Photonics Applications I*; Springer, 2002; Vol. 7; pp 1–86.

[95] Kanis, D. R.; Ratner, M. A.; Marks, T. J. Design and construction of molecular assemblies with large second-order optical nonlinearities. Quantum chemical aspects. *Chem. Rev.* **1994**, *94a*, 195–242.

[96] Verbiest, T.; Houbrechts, S.; Kauranen, M.; Clays, K.; Persoons, A. Second-order nonlinear optical materials: recent advances in chromophore design. *J. Mater. Chem.* **1997**, *7*, 2175–2189.

[97] Limacher, P. A.; Mikkelsen, K. V.; Lüthi, H. P. On the accurate calculation of polarizabilities and second hyperpolarizabilities of polyacetylene oligomer chains using the CAM-B3LYP density functional. *J. Chem. Phys.* **2009**, *130*, 194114.

[98] Bishop, D. M. Molecular vibrational and rotational motion in static and dynamic electric Fields. *Rev. Mod. Phys.* **1990**, *62*, 343–374.

[99] Bishop, D. M.; Champagne, B.; Kirtman, B. Relationship between static vibrational and electronic hyperpolarizabilities of π-conjugated push-pull molecules within the two-state valence-bond charge-transfer model. *J. Chem. Phys.* **1998**, *109*, 9987–9994.

[100] Bishop, D. M.; Champagne, B.; Kirtman, B. Static and dynamic polarizabilities and first hyperpolarizabilities for CH_4, CF_4, and CCl_4. *J. Chem. Phys.* **1998**, *109*, 8407–8415.

[101] Barone, V.; Baiardi, A.; Biczysko, M.; Bloino, J.; Cappelli, C.; Lipparini, F. Implementation and validation of a multi-purpose virtual spectrometer for large systems in complex environments. *Phys. Chem. Chem. Phys.* **2012**, *14*, 12404–12422.

[102] Bishop, D. M.; Kirtman, B. A perturbation method for calculating vibrational dynamic dipole polarizabilities and hyperpolarizabilities. *J. Chem. Phys.* **1991**, *95*, 2646–2658.

[103] Bishop, D. M.; Kirtman, B. Compact formulas for vibrational dynamic dipole polarizabilities and hyperpolarizabilities. *J. Chem. Phys.* **1992**, *97*, 5255–5256.

[104] Liptay, W.; Becker, J.; Wehning, D.; Lang, W.; Burkhard, O. The Determination of Molecular Quantities from Measurements on Macroscopic Systems. II. The Determination of Electric Dipole Moments. *Z. Naturforsch.* **1982**, *37a*, 1396–1408.

[105] Quinet, O.; Champagne, B.; Kirtman, B. Analytical TDHF Second Derivatives of Dynamic Electronic Polarizability with Respect to Nuclear Coordinates. Application to the Dynamic ZPVA Correction. *J. Comput. Chem.* **2001**, *22*, 1920–1932.

[106] Quinet, O.; Champagne, B. Analytical time-dependent Hartree–Fock schemes for the evaluation of the hyper-Raman intensities. *J. Chem. Phys.* **2002**, *117*, 2481–2488.

[107] Quinet, O.; Champagne, B.; Kirtman, B. Analytical time-dependent Hartree-Fock evaluation of the dynamic zero-point vibrationally averaged (ZPVA) first hyperpolarizability. *J. Chem. Phys.* **2003**, *118*, 505–513.

[108] Wortmann, R.; Bishop, D. M. Effective polarizabilities and local field corrections for nonlinear optical experiments in condensed media. *J. Chem. Phys.* **1998**, *108*, 1001–1007.

[109] Cappelli, C. In *Continuum Solvation Models in Chemical Physics*; Cammi, R., Mennucci, B., Eds.; John Wiley & Sons Inc.: Chichester, 2012; pp 167–179.

[110] Orr, B. J.; Ward, J. F. Perturbation theory of the non-linear optical polarization of an isolated system. *Mol. Phys.* **1971**, *20*, 513–526.

[111] Thicoipe, S.; Carbonniere, P.; Pouchan, C. Comparison of static and dynamic methods of treatment of anharmonicity for the vibrational study of isolated and aqueous forms of guanine. *Chem. Phys. Lett.* **2014**, *591*, 243–247.

[112] Cappelli, C.; Monti, S.; Scalmani, G.; Barone, V. On the Calculation of Vibrational Frequencies for Molecules in Solution Beyond the Harmonic Approximation. *J. Chem. Theory Comput.* **2010**, *6*, 1660–1669.

[113] Frisch, M. J.; Trucks, G. W.; Schlegel, H. B.; Scuseria, G. E.; Robb, M. A.; Cheeseman, J. R.; Scalmani, G.; Barone, V.; Mennucci, B.; Petersson, G. A.; Nakatsuji, H.; Caricato, M.; Li, X.; Hratchian, H. P.; Izmaylov, A. F.; Bloino, J.; Zheng, G.; Sonnenberg, J. L.; Hada, M.; Ehara, M.; Toyota, K.; Fukuda, R.; Hasegawa, J.; Ishida, M.; Nakajima, T.; Honda, Y.; Kitao, O.; Nakai, H.; Vreven, T.; J. A. Montgomery, J.; Peralta, J. E.; Ogliaro, F.; Bearpark, M.; Heyd, J. J.; Brothers, E.; Kudin, K. N.; Staroverov, V. N.; Kobayashi, R.; Normand, J.; Raghavachari, K.; Rendell, A.; Burant, J. C.; Iyengar, S. S.; Tomasi, J.; Cossi, M.; Rega, N.; Millam, J. M.; Klene, M.; Knox, J. E.; Cross, J. B.; Bakken, V.; Adamo, C.; Jaramillo, J.; Gomperts, R.; Stratmann, R. E.; Yazyev, O.; Austin, A. J.; Cammi, R.; Pomelli, C.; Ochterski, J. W.; Martin, R. L.; Morokuma, K.; Zakrzewski, V. G.; Voth, G. A.; Salvador, P.; Dannenberg, J. J.; Dapprich, S.; Daniels, A. D.; Farkas, Ö.; Foresman, J. B.; Ortiz, J. V.; Cioslowski, J.; Fox, D. J. Gaussian 09 Revision D.01. Gaussian Inc. Wallingford CT 2009.

[114] Yanai, T.; Tew, D. P.; Handy, N. C. A new hybrid exchange-correlation functional using the Coulomb-attenuating method (CAM-B3LYP). *Chem. Phys. Lett.* **2004**, *393*, 51–57.

[115] Bulik, I. W.; Zaleśny, R.; Bartkowiak, W.; Luis, J. M.; Kirtman, B.; Scuseria, G. E.; Avramopoulos, A.; Reis, H.; Papadopoulos, M. G. Performance of density functional theory in computing nonresonant vibrational (hyper)polarizabilities. *J. Comput. Chem.* **2013**, *34*, 1775–1784.

[116] Baranowska-Łaczkowska, A.; Bartkowiak, W.; Góra, R. W.; Pawłowski, F.; Zaleśny, R. On the performance of long-range-corrected density functional theory and reduced-size polarized LPol-n basis sets in computations of electric dipole (hyper)polarizabilities of π-conjugated molecules. *J. Comput. Chem.* **2013**, *34*, 819–826.

[117] Becke, A. D. Density-functional thermochemistry. III. The role of exact exchange. *J. Chem. Phys.* **1993**, *98*, 5648–5652.

[118] Lee, C.; Yang, W.; Parr, R. G. Development of the Colle-Salvetti correlation-energy formula into a functional of the electron density. *Phys. Rev. B* **1988**, *37*, 785–789.

[119] Zhao, Y.; Truhlar, D. G. The M06 suite of density functionals for main group thermochemistry, thermochemical kinetics, noncovalent interactions, excited states, and transition elements: two new functionals and systematic testing of four M06-class functionals and 12 other functionals. *Theor. Chem. Acc.* **2008**, *393*, 215–241.

[120] Adamo, C.; Barone, V. Toward reliable density functional methods without adjustable parameters: The PBE0 model. *J. Chem. Phys.* **1999**, *110*, 6158–6169.

[121] Chai, J.-D.; Head-Gordon, M. Systematic optimization of long-range corrected hybrid density functionals. *J. Chem. Phys.* **2008**, *128*, 084106.

[122] Kendall, R. A.; Dunning Jr., T. H.; Harrison, R. J. Electron affinities of the first-row atoms revisited. Systematic basis sets and wave functions. *J. Chem. Phys.* **1992**, *96*, 6796–6806.

[123] Daniel, C.; Dupuis, M. Nonlinear optical properties of organic solids: ab initio polarizability and hyperpolarizabilities of nitroaniline derivatives. *Chem. Lett.* **1990**, *171*, 209–216.

[124] Karna, S. P.; Prasad, P. N.; Dupuis, M. Nonlinear optical properties of p-nitroaniline: An ab initio time-dependent coupled perturbed Hartree-Fock study. *J. Chem. Phys.* **1991**, *94*, 1171.

[125] Sim, F.; Chin, S.; Dupuis, M.; Rice, J. E. Electron correlation effects in hyperpolarizabilities of p-nitroaniline. *J. Phys. Chem.* **1993**, *97*, 1158–1163.

[126] Champagne, B. Vibrational polarizability and hyperpolarizability of p-nitroaniline. *Chem. Phys. Lett.* **1996**, *261*, 57–65.

[127] Cammi, R.; Frediani, L.; Mennucci, B.; Ruud, K. Multiconfigurational self-consistent field linear response for the polarizable continuum model: Theory and application to ground and excited-state polarizabilities of para-nitroaniline in solution. *J. Chem. Phys.* **2003**, *119*, 5818–5827.

[128] Soscún, H.; Castellano, O.; Bermúdez, Y.; Toro, C.; Cubillán, N.; Hinchliffe, A.; Phu, X. N. B3LYP study of the dipole moment and the static dipole (hyper) polarizabilities of para-nitroaniline in gas phase. *Int. J. Quantum Chem.* **2006**, *106*, 1130–1137.

[129] Cheng, L. T.; Tam, W.; Stevenson, S. H.; Meredith, G. R.; Rikken, G.; Marder, S. R. Experimental investigations of organic molecular nonlinear optical polarizabilities. 1. Methods and results on benzene and stilbene derivatives. *J. Phys. Chem.* **1991**, *95*, 10631–10643.

[130] Luis, J. M.; Reis, H.; Papadopoulos, M.; Kirtman, B. Treatment of nonlinear optical properties due to large amplitude anharmonic vibrational motions: Umbrella motion in NH_3. *J. Chem. Phys.* **2009**, *131*, 034116.

[131] Garcia-Borràs, M.; Sola, M.; Lauvergnat, D.; Reis, H.; Luis, J. M.; Kirtman, B. A Full Dimensionality Approach to Evaluate the Nonlinear Optical Properties of Molecules with Large Amplitude Anharmonic Tunneling Motions. *J. Chem. Theory Comput.* **2013**, *9*, 520–532.

[132] Reis, H.; Luis, J. M.; Garcia-Borràs, M.; Kirtman, B. Computation of Nonlinear Optical Properties of Molecules with Large Amplitude Anharmonic Motions. III. Arbitrary Double-Well Potentials. *J. Chem. Theory Comput.* **2014**, *10*, 236–242.

[133] Wortmann, R.; Krämer, P.; Glania, C.; Lebus, S.; Detzer, N. Deviations from Kleinman symmetry of the second-order polarizability tensor in molecules with low-lying perpendicular electronic bands. *Chem. Phys.* **1993**, *173*, 99–108.

[134] Wortmann, R.; Poga, C.; Twieg, R. J.; Geletneky, C.; Moylan, C. R.; Lundquist, P. M.; DeVoe, R. G.; Cotts, P. M.; Horn, H.; Rice, J. E.; Burland, D. M. Design of optimized photorefractive polymers: A novel class of chromophores. *J. Chem. Phys.* **1996**, *105*, 10637–10647.

[135] Kang, Y. K.; Jhon, M. S. Additivity of atomic static polarizabilities and dispersion coefficients. *Theo. Chim. Acta* **1982**, *61*, 41–48.

[136] Liptay, W.; Wortmann, R.; Schaffrin, H.; Burkhard, O.; Reitinger, W.; Detzer, N. Excited State Dipole Moments and Polariz-

abilities of Centrosymmetric and Dimeric Molecules. I. Model Study of a Bichromophoric Molecule. *Chem. Phys.* **1988**, *120*, 429–438.

[137] Berova, N.; Polavarapu, P. L.; Nakanishi, K.; Woody, R. W. *Comprehensive Chiroptical Spectroscopy*; Wiley, 2011.

[138] Nafie, L. A. *Vibrational Optical Activity: Principles and Applications*; Wiley, 2001.

[139] Stephens, P. J.; Devlin, F. J.; Cheeseman, J. R. *VCD Spectroscopy for Organic Chemists*; Wiley, 2001.

[140] Barone, V. *Computational Strategies for Spectroscopy*; John Wiley & Sons Inc.: Hoboken, New Jersey, 2012.

[141] Barone, V.; Improta, R.; Rega, N. Quantum Mechanical Computations and Spectroscopy: From Small Rigid Molecules in the Gas Phase to Large Flexible Molecules in Solution. *Acc. Chem. Res.* **2008**, *41*, 605–616.

[142] Lessi, M.; Manzini, C.; Minei, P.; Perego, L. A.; Bloino, J.; Egidi, F.; Barone, V.; Pucci, A.; Bellina, F. Synthesis and Optical Properties of Imidazole-Based Fluorophores having High Quantum Yields. *ChemPlusChem* **2014**, *79*, 366–370.

[143] Elmore, D. E.; Dougherty, D. A. A Computational Study of Nicotine Conformations in the Gas Phase and in Water. *J. Org. Chem.* **2000**, *65*, 742–747.

[144] Takeshima, T.; Fukumoto, R.; Egawa, T.; Konaka, S. Molecular Structure of Nicotine As Studied by Gas Electron Diffraction Combined with Theoretical Calculations. *J. Phys. Chem. A* **2002**, *106*, 8734–8740.

[145] Mora, M.; Castro, M. E.; Nino, A.; Melendez, F. J.; Muñoz-Caro, C. Analysis of B3LYP and MP2 Conformational Population Distributions in trans-Nicotine, Acetylcholine, and ABT-594. *Int. J. Quantum Chem.* **2005**, *103*, 25–33.

[146] Muñoz-Caro, C.; Nino, A.; Mora, M.; Reyes, S.; Melendez, F. J.; Castro, M. E. Conformational population distribution of acetylcholine, nicotine and muscarine in vacuum and solution. *J. Mol. Struc.-THEOCHEM* **2005**, *726*, 115–124.

[147] Whidby, J. F.; Edwards III, W. B.; Pitner, T. P. Isomeric Nicotines. Their Solution Conformation and Proton, Deuterium, Carbon-13, and Nitrogen- 15 Nuclear Magnetic Resonance. *J. Org. Chem.* **1979**, *44*, 794–798.

[148] Testa, B.; Jenner, P. Circular Dichroic Determination of the Preferred Conformation of Nicotine and Related Chiral Alkaloids in Aqueous Solution. *Mol. Pharm.* **1972**, *9*, 10–16.

[149] Clayton, P. M.; Vas, C. A.; Bui, T. T. T.; Drake, A. F.; McAdam, K. Spectroscopic Studies on Nicotine and Nornicotine in the UV Region. *Chirality* **2013**, *5*, 288–293.

[150] Clayton, P. M.; Vas, C. A.; Bui, T. T. T.; Drake, A. F.; McAdam, K. Spectroscopic investigations into the acid–base properties of nicotine at different temperatures. *Anal. Methods* **2013**, *5*, 81–88.

[151] Baranska, M.; Dobrowolski, J. C.; Kaczor, A.; Chruszcz-Lipska, K.; Gorza, K.; Rygula, A. Tobacco alkaloids analyzed by Raman spectroscopy and DFT calculations. *J. Raman Spectrosc.* **2012**, *43*, 1065–1073.

[152] Cammi, R.; Mennucci, B. *Continuum Solvation Models in Chemical Physics*; John Wiley & Sons Inc., 2007.

[153] Frediani, L.; Cammi, R.; Corni, S.; Tomasi, J. A polarizable continuum model for molecules at diffuse interfaces. *J. Chem. Phys.* **2004**, *120*, 3893–3907.

[154] Mennucci, B.; Caricato, M.; Ingrosso, F.; Cappelli, C.; Cammi, R.; Tomasi, J.; Scalmani, G.; Frisch, M. J. How the Environment Controls Absorption and Fluorescence Spectra of PRODAN: A Quantum-Mechanical Study in Homogeneous and Heterogeneous Media. *J. Phys. Chem. B* **2008**, *112*, 414–423.

[155] Bertoldo, M.; Bronco, S.; Cappelli, C.; Gragnoli, T.; Andreotti, L. Combining Theory and Experiment to Study the Photooxidation of Polyethylene and Polypropylene. *J. Phys. Chem. B* **2003**, *107*, 11880–11888.

[156] Stephens, P. J.; Devlin, F. J.; Cheeseman, J. R.; Frisch, M. J. Calculation of Optical Rotation Using Density Functional Theory. *J. Phys. Chem. A* **2001**, *105*, 5356–5371.

[157] Epstein, S. T. Gauge Invariance of the Hartree-Fock Approximation. *J. Chem. Phys.* **1965**, *42*, 2897–2898.

[158] Ditchfield, R. Self-consistent perturbation theory of diamagnetism. *Mol. Phys.* **1974**, *27*, 789–807.

[159] Cheeseman, J. R.; Frisch, M. J.; Devlin, F. J.; Stephens, P. J. Hartree-Fock and Density Functional Theory ab Initio Calculation of Optical Rotation Using GIAOs: Basis Set Dependence. *J. Phys. Chem. A* **2000**, *104*, 1039–1046.

[160] Mennucci, B.; Tomasi, J.; Cammi, R.; Cheeseman, J. R.; Frisch, M. J.; Devlin, F. J.; Gabriel, S.; Stephens, P. J. Polarizable Continuum Model (PCM): Calculations of Solvent Effects on Optical Rotations of Chiral Molecules. *J. Phys. Chem. A* **2002**, *106*, 6102–6113.

[161] Ruud, K.; Taylor, P. R.; Åstrand, P.-O. Zero-point vibrational effects on optical rotation. *Chem. Phys. Lett.* **2001**, *337*, 217–223.

[162] Ruud, K.; Zanasi, R. The Importance of Molecular Vibrations: The Sign Change of the Optical Rotation of Methyloxirane. *Angew. Chem. Int. Ed.* **2005**, *44*, 3594–3596.

[163] Kongsted, J.; Pedersen, T. B.; Jensen, L.; Hansen, A. E.; Mikkelsen, K. V. Coupled Cluster and Density Functional Theory Studies of the Vibrational Contribution to the Optical Rotation of (S)-Propylene Oxide. *J. Am. Chem. Soc.* **2006**, *128*, 976–982.

[164] Kongsted, J.; Ruud, K. Solvent effects on zero-point vibrational corrections to optical rotations and nuclear magnetic resonance shielding constants. *Chem. Phys. Lett.* **2008**, *451*, 226–232.

[165] Auer, A. A.; Gauss, J.; Stanton, J. F. Quantitative prediction of gas-phase shielding constants 13C nuclear magnetic shielding constants. *J. Chem. Phys.* **2003**, *118*, 10407–10417.

[166] Grigoleit, S.; Bühl, M. Thermal Effects and Vibrational Corrections to Transition Metal NMR Chemical Shifts. *Chem. Eur. J.* **2004**, *10*, 5541–5552.

[167] Mort, B. C.; Autschbach, J. Magnitude of Zero-Point Vibrational Corrections of Optical Rotation in Rigid Organic Molecules. *J. Phys. Chem. A* **2005**, *109*, 8617–8623.

[168] Mennucci, B.; Cappelli, C.; Cammi, R.; Tomasi, J. Modeling Solvent Effects on Chiroptical Properties. *Chirality* **2011**, *23*, 717–729.

[169] Barone, V.; Cimino, P.; Stendardo, E. Development and Validation of the B3LYP/N07D Computational Model for Structural Parameter and Magnetic Tensors of Large Free Radicals. *J. Chem. Theory Comput.* **2008**, *4*, 751–764.

[170] Barone, V.; Biczysko, M.; Bloino, J.; Egidi, F.; Puzzarini, C. Accurate structure, thermodynamics, and spectroscopy of medium-sized radicals by hybrid coupled cluster/density functional theory approaches: The case of phenyl radical. *J. Phys. Chem.* **2013**, *138*, 234303.

[171] Papajak, E.; Leverentz, H. R.; Zheng, J.; Truhlar, D. G. Efficient Diffuse Basis Sets: cc-pVxZ+ and maug-cc-pVxZ. *J. Chem. Theory Comput.* **2009**, *5*, 1197–1202.

[172] Cheeseman, J. R.; Frisch, M. J. Basis Set Dependence of Vibrational Raman and Raman Optical Activity Intensities. *J. Chem. Theory Comput.* **2011**, *7*, 3323–3334.

[173] Infrared spectrum from the Bio-Rad/Sadtler IR Data Collection, obtained from Bio-Rad Laboratories, Philadelphia, PA (US).

[174] Milani, A.; Tommasini, M.; Del Zoppo, M.; Castiglioni, C. In *Continuum Solvation Models in Chemical Physics*; Cammi, R., Mennucci, B., Eds.; John Wiley & Sons Inc.: Chichester, 2012; pp 558–579.

[175] Baitinger, W. F.; Von R. Schleyer, P.; Murty, T. S. S. R.; Robinson, L. Nitro groups as proton acceptors in hydrogen bonding. *Tetrahedron* **1964**, *20*, 1635–1647.

[176] Thomsen, C. L.; Thøgersen, J.; Keiding, S. R. Ultrafast Charge-Transfer Dynamics: Studies of *p*-Nitroaniline in Water and Dioxane. *J. Phys. Chem. A* **1998**, *102*, 1062–1067.

[177] Jensen, L.; Autschbach, J.; Schatz, G. C. Finite lifetime effects on the polarizability within time-dependent density-functional theory. *J. Chem. Phys.* **2005**, *122*, 224115.

[178] Jensen, L.; Zhao, L. L.; Autschbach, J.; Schatz, G. C. Theory and method for calculating resonance Raman scattering from resonance polarizability derivatives. *J. Chem. Phys.* **2005**, *123*, 174110.

[179] Norman, P.; Bishop, D. M.; Jensen, H. J. A.; Oddershede, J. Nonlinear response theory with relaxation: The first-order hyperpolarizability. *J. Chem. Phys.* **2005**, *123*, 194103.

[180] Ågren, A. M. H.; Norman, P. Resonance enhanced Raman scattering from the complex electric-dipole polarizability: A theoretical study on N_2. *Chem. Phys. Lett.* **2009**, *468*, 119–123.

[181] Ågren, A. M. H.; Norman, P. Time-dependent density functional theory for resonant properties: resonance enhanced Raman scattering from the complex electric-dipole polarizability. *Phys. Chem. Chem. Phys.* **2009**, *11*, 4539–4548.

[182] Latorre, M. T. F.; Marquetand, P. Resonance Raman spectra of ortho-nitrophenol calculated by real-time time-dependent density functional theory. *J. Chem. Phys.* **2013**, *138*, 044101.

[183] Quinet, O.; Champagne, B. Time-dependent Hartree-Fock schemes for analytical evaluation of the Raman intensities. *J. Chem. Phys.* **2001**, *115*, 6293–6299.

[184] Quinet, O.; Champagne, B. Investigation of the frequency-dispersion effects on the Raman spectra of small polyenes. *Int. J. Quantum Chem.* **2002**, *89*, 341–348.

[185] Quinet, O. Vibrational spectroscopies: Description of general analytical TDHF schemes for their simulation. *Int. J. Quantum Chem.* **2005**, *104*, 727–743.

[186] Efremov, E. V.; Ariese, F.; Gooijer, C. Achievements in resonance Raman spectroscopy. Review of a technique with a distinct analytical chemistry potential. *Anal. Chim. Acta* **2008**, *606*, 119–134.

[187] Horvath, R.; Gordon, K. C. Understanding excited-state structure in metal polypyridyl complexes using resonance Raman excitation profiles, time-resolved resonance Raman spectroscopy and density functional theory. *Coord. Chem. Rev.* **2010**, *254*, 2505–2518.

[188] Boereboom, L. M.; van Hemert, M. C.; Neugebauer, J. The Resonance Raman Spectra of Spheroidene Revisited with a First-Principles Approach. *ChemPhysChem* **2011**, *12*, 3157–3169.

[189] Oladepo, S. A.; Xiong, K.; Hong, Z.; Asher, S. A. Elucidating Peptide and Protein Structure and Dynamics: UV Resonance Raman Spectroscopy. *J. Phys. Chem. Lett.* **2011**, *2*, 334–344.

[190] Oladepo, S. A.; Xiong, K.; Hong, Z.; Asher, S. A.; Handen, J.; Lednev, I. K. UV Resonance Raman Investigations of Peptide and Protein Structure and Dynamics. *Chem. Rev.* **2012**, *112*, 2604–2628.

[191] Kelley, A. M. Resonance Raman and Resonance hyper-Raman Intensities: Structure and Dynamics of Molecular Excited States in Solution. *J. Phys. Chem. A* **2008**, *112*, 11975–11991.

[192] Warshel, A.; Dauber, P. Calculations of resonance Raman spectra of conjugated molecules. *J. Chem. Phys.* **1997**, *66*, 5477–5488.

[193] Placzek, G. In *Handbuch der Radiologie VI*; Marx, E., Ed.; Akademische Verlagsgesellshaft: Leipzig, Germany, 1934; Vol. 2; pp 209–374.

[194] Albrecht, A. C. On the Theory of Raman Intensities. *J. Chem. Phys.* **1961**, *34*, 1476–1484.

[195] Lee, S.-Y.; Heller, E. J. Time-dependent theory of Raman scattering. *J. Chem. Phys.* **1979**, *71*, 4777–4788.

[196] Tannor, D. J.; Heller, E. J. Polyatomic Raman Scattering for General Harmonic Potentials. *J. Chem. Phys.* **1982**, *77*, 202–218.

[197] Yan, Y. J.; Mukamel, S. Eigenstate-free, Green function, calculation of molecular absorption and fluorescence line shapes. *J. Chem. Phys.* **1986**, *85*, 5908–5922.

[198] Blazej, D. C.; Peticolas, W. L. Ultraviolet resonance Raman excitation profiles of pyrimidine nucleotides. *J. Chem. Phys.* **1980**, *72*, 3134–3142.

[199] Peticolas, W. L.; Rush III, T. Ab Initio Calculations of the Ultraviolet Resonance Raman Spectra of Uracil. *J. Comput. Chem.* **1995**, *16*, 1261–1260.

[200] Neugebauer, J.; Hess, B. A. Resonance Raman spectra of uracil based on Kramers–Kronig relations using time-dependent density functional calculations and multireference perturbation theory. *J. Chem. Phys.* **2004**, *120*, 11564–11477.

[201] Guthmuller, J.; Champagne, B. Time dependent density functional theory investigation of the resonance Raman properties of the julolidinemalononitrile push-pull chromophore in various solvents. *J. Chem. Phys.* **2007**, *127*, 164507.

[202] Guthmuller, J.; Gonzalez, L. Simulation of the resonance Raman intensities of a ruthenium–palladium photocatalyst by time dependent density functional theory. *Phys. Chem. Chem. Phys.* **2010**, *12*, 14812–14821.

[203] Petrenko, T.; Neese, F. Analysis and prediction of absorption band shapes, fluorescence band shapes, resonance Raman intensities, and excitation profiles using the time-dependent theory of electronic spectroscopy. *J. Chem. Phys.* **2007**, *127*, 164319.

[204] Petrenko, T.; Neese, F. Efficient and automatic calculation of optical band shapes and resonance Raman spectra for larger molecules within the independent mode displaced harmonic oscillator model. *J. Chem. Phys.* **2012**, *137*, 234107.

[205] Romanova, J.; Liégeois, V.; Champagne, B. Analysis of the Resonant Raman Spectra of Viologens and of Their Radical Cations Using Range-Separated Hybrid Density Functionals. *J. Phys. Chem. C* **2014**, *118*, 12469–12484.

[206] Jarzecki, A. A.; Spiro, T. G. Ab initio computation of the UV resonance Raman intensity pattern of aqueous imidazole. *J. Raman Spectrosc.* **2001**, *32*, 599–605.

[207] Mennucci, B.; Cappelli, C.; Cammi, R.; Tomasi, J. A quantum mechanical polarizable continuum model for the calculation of resonance Raman spectra in condensed phase. *Theor. Chem. Acc.* **2007**, *117*, 1029–1039.

[208] Guthmuller, J. Assessment of TD-DFT and CC2 Methods for the Calculation of Resonance Raman Intensities: Application to o-Nitrophenol. *J. Chem. Theory Comput.* **2011**, *7*, 1082–1089.

[209] Kupfer, S.; Guthmuller, J.; Gonzàlez, L. An Assessment of RASSCF and TDDFT Energies and Gradients on an Organic Donor-Acceptor Dye Assisted by Resonance Raman Spectroscopy. *J. Chem. Theory Comput.* **2013**, *9*, 543–554.

[210] Aquino, F. W.; Schatz, G. C. Time-Dependent Density Functional Methods for Raman Spectra in Open-Shell Systems. *J. Phys. Chem. A* **2014**, *118*, 517–525.

[211] Kane, K. A.; Jensen, L. Calculation of Absolute Resonance Raman Intensities: Vibronic Theory vs Short-Time Approximation. *J. Phys. Chem. C* **2010**, *114*, 5540–5546.

[212] Al-Saidi, W. A.; Asher, S. A.; Norman, P. Resonance Raman Spectra of TNT and RDX Using Vibronic Theory, Excited-State Gradient, and Complex Polarizability Approximations. *J. Phys. Chem. A* **2012**, *116*, 7862–7872.

[213] Lucas, N. J. D. The Franck-Condon principle for polyatomic molecules. *J. Phys. B: Atom. Molec. Phys.* **1973**, *6*, 155–163.

[214] Duschinsky, F. *Acta Physicochim. URSS* **1937**, *7*, 551.

[215] Ma, H.; Liu, J.; Liang, W. Time-Dependent Approach to Resonance Raman Spectra Including Duschinsky Rotation and Herzberg-Teller Effects: Formalism and Its Realistic Applications. *J. Chem. Theory Comput.* **2012**, *8*, 4474–4482.

[216] Banerjee, S.; Kröner, D.; Saalfrank, P. Resonance Raman and vibronic absorption spectra with Duschinsky rotation from a time-dependent perspective: Application to β-carotene. *J. Chem. Phys.* **2012**, *137*, 22A534.

[217] Banerjee, S.; Saalfrank, P. Vibrationally resolved absorption, emission and resonance Raman spectra of diamondoids: a study based on time-dependent correlation functions. *Phys. Chem. Chem. Phys.* **2014**, *16*, 144–158.

[218] Baiardi, A.; Bloino, J.; Barone, V. A general time-dependent route to Resonance-Raman spectroscopy including Franck-Condon, Herzberg-Teller and Duschinsky effects. *J. Chem. Phys.* **2014**, *141*, 114108.

[219] Biczysko, M.; Bloino, J.; Santoro, F.; Barone, V. In *Computational Strategies for Spectroscopy*; Barone, V., Ed.; John Wiley & Sons Inc.: Hoboken, New Jersey, 2012; pp 361–443.

[220] Nooijen, M. *Int. J. Quantum Chem.* **2006**, *106*, 2489–2510.

[221] Sharp, T. E.; Rosenstock, H. M. *J. Chem. Phys.* **1964**, *41*, 3453–3463.

[222] Ruhoff, P. T. *Chem. Phys.* **1994**, *186*, 355–374.

[223] Ruhoff, P. T.; Ratner, M. A. *Int. J. Quantum Chem.* **2000**, *77*, 383–392.

[224] Santoro, F.; Improta, R.; Lami, A.; Bloino, J.; Barone, V. Effective method to compute Franck-Condon integrals for optical spectra of large molecules in solution. *J. Chem. Phys.* **2007**, *126*, 084509.

[225] Santoro, F.; Lami, A.; Improta, R.; Bloino, J.; Barone, V. Effective method for the computation of optical spectra of large molecules at finite temperature including the Duschinsky and Herzberg–Teller effect: The Qx band of porphyrin as a case study. *J. Chem. Phys.* **2008**, *128*, 224311.

[226] Jankowiak, H. C.; Stuber, J. L.; Berger, R. Vibronic transitions in large molecular systems: Rigorous prescreening conditions for Franck-Condon factors. *J. Chem. Phys.* **2007**, *127*, 234101.

[227] Huh, J.; Berger, R. Application of time-independent cumulant expansion to calculation of Franck–Condon profiles for large molecular systems. *Faraday Discuss.* **2011**, *150*, 363–373.

[228] Huh, J.; Berger, R. Coherent state-based generating function approach for Franck–Condon transitions and beyond. *J. Phys.: Conf. Ser.* **2012**, *380*, 012019.

[229] Vázquez, J.; Stanton, J. F. Simple(r) algebraic equation for transition moments of fundamental transitions in vibrational second-order perturbation theory. *Mol. Phys.* **2006**, *104*, 377–388.

[230] Bludský, O.; Bak, K. L.; Jørgensen, P.; Špirko, V. Ab initio calculations of anharmonic vibrational transition intensities of trans-2,3-dideuteriooxirane. *J. Chem. Phys.* **1995**, *103*, 10110.

[231] Bak, K. L.; Bludský, O.; Jørgensen, P. Ab initio calculations of anharmonic vibrational circular dichroism intensities of trans-2,3-dideuteriooxirane. *J. Chem. Phys.* **1995**, *103*, 10548.

[232] Yamaguchi, M. Calculation of infrared absorption intensities of combination bands of cyclic acid dimers by vibrational second order perturbation theory. *Comput. Theor. Chem.* **2013**, *1022*, 70–74.

[233] Luis, J. M.; Kirtman, B.; Christiansen, O. A variational approach for calculating Franck-Condon factors including mode-mode anharmonic coupling. *J. Chem. Phys.* **2006**, *125*, 154114.

[234] Bloino, J.; Biczysko, M.; Crescenzi, O.; Barone, V. Integrated computational approach to vibrationally resolved electronic spectra: Anisole as a test case. *J. Chem. Phys.* **2008**, *128*, 244105.

[235] Rauhut, G.; Pulay, P. Transferable Scaling Factors for Density Functional Derived Vibrational Force Fields. *J. Phys. Chem.* **1995**, *99*, 3093–3100.

[236] Sinha, P.; Boesch, S. E.; Gu, C.; Wheeler, R. A.; Wilson, A. K. Harmonic Vibrational Frequencies: Scaling Factors for HF, B3LYP, and MP2 Methods in Combination with Correlation Consistent Basis Sets. *J. Phys. Chem. A* **2004**, *108*, 9213–9217.

[237] Andersson, M. P.; Uvdal, P. New Scale Factors for Harmonic Vibrational Frequencies Using the B3LYP Density Functional Method with the Triple-ζ Basis Set 6-311+G(d,p). *J. Phys. Chem. A* **2005**, *109*, 2937–2941.

[238] Carnimeo, I.; Biczysko, M.; Bloino, J.; Barone, V. Reliable structural, thermodynamic, and spectroscopic properties of organic molecules adsorbed on silicon surfaces from computational modeling: the case of glycine@Si(100). *Phys. Chem. Chem. Phys.* **2011**, *13*, 16713–16727.

[239] Barone, V.; Biczysko, M.; Bloino, J.; Borkowska-Panek, M.; Carnimeo, I.; Panek, P. Toward Anharmonic Computations of Vibrational Spectra for Large Molecular Systems. *Int. J. Quantum Chem.* **2012**, *112*, 2185–2200.

[240] Holzer, W.; Murphy, W. F.; Bernstein, H. J. Resonance Raman Effect and Resonance Fluorescence in Halogen Gases. *J. Chem. Phys.* **1970**, *52*, 399–407.

[241] Asher, S. A.; Murtaugh, J. Metalloporphyrin Gas and Condensed-Phase Resonance Raman Studies: The Role of Vibrational Anharmonicities as Determinants of Raman Frequencies. *J. Am. Chem. Soc.* **1983**, *105*, 7244–7251.

[242] Myers, A. B.; Li, B.; Ci, X. A resonance Raman intensity study of electronic spectral broadening mechanisms in CS_2/cyclohexane. *J. Chem. Phys.* **1988**, *89*, 1876–1886.

[243] Ziegler, L. D.; Chung, Y. C.; Wang, P.; Zhang, Y. P. Metalloporphyrin Gas and Condensed-Phase Resonance Raman Studies: The

Role of Vibrational Anharmonicities as Determinants of Raman Frequencies. *J. Chem. Phys.* **1989**, *90*, 4125–4143.

[244] Yamaguchi, T.; Kimura, Y.; Hirota, N. Solvent and Solvent Density Effects on the Spectral Shifts and the Bandwidths of the Absorption and the Resonance Raman Spectra of Phenol Blue. *J. Phys. Chem. A* **1997**, *101*, 9050–9060.

[245] Kelley, A. M. Resonance Raman Intensity Analysis of Vibrational and Solvent Reorganization in Photoinduced Charge Transfer. *J. Phys. Chem. A* **1999**, *103*, 6891–6903.

[246] Leng, W.; Würthner, F.; Kelley, A. M. Solvent-Dependent Vibrational Frequencies and Reorganization Energies of Two Merocyanine Chromophores. *J. Phys. Chem. A* **1999**, *103*, 6891–6903.

[247] Myers, A. B. Molecular Electronic Spectral Broadening in Liquids and Glasses. *Annu. Rev. Phys. Chem.* **1998**, *49*, 267–295.

[248] Guthmuller, J.; Champagne, B. Resonance Raman scattering of rhodamine 6G as calculated by time-dependent density functional theory: Vibronic and solvent effects. *J. Phys. Chem. A* **2008**, *112*, 3215–3223.

[249] Guthmuller, J.; Champagne, B. Resonance Raman Spectra and Raman Excitation Profiles of Rhodamine 6G from Time-Dependent Density Functional Theory. *ChemPhysChem* **2008**, *9*, 1667–1669.

[250] Guthmuller, J.; Champagne, B.; Moucheron, C.; Andree, K. Investigation of the Resonance Raman Spectra and Excitation Profiles of a Monometallic Ruthenium(II) [Ru(bpy)(2)(HAT)](2+) Complex by Time-Dependent Density Functional Theory. *J. Phys. Chem. B* **2010**, *114*, 511–520.

[251] Avila Ferrer, F. J.; Barone, V.; Cappelli, C.; Santoro, F. Duschinsky, Herzberg–Teller, and Multiple Electronic Resonance Interferential Effects in Resonance Raman Spectra and Excitation Profiles. The Case of Pyrene. *J. Chem. Theory Comput.* **2013**, *9*, 3597–3611.

[252] Jarzecki, A. A. Quantum-Mechanical Calculations of Resonance Raman Intensities: The Weighted-Gradient Approximation. *J. Phys. Chem. A* **2009**, *113*, 2926–2934.

[253] Mennucci, B.; Cappelli, C.; Guido, C. A.; Cammi, R.; Tomasi, J. Structures and Properties of Electronically Excited Chromophores in Solution from the Polarizable Continuum Model Coupled to the Time-Dependent Density Functional Theory. *J. Phys. Chem. A* **2009**, *113*, 3009–3020.

[254] Carnimeo, I.; Puzzarini, C.; Tasinato, N.; Stoppa, P.; Charmet, A. P.; Biczysko, M.; Cappelli, C.; Barone, V. Anharmonic theoretical simulations of infrared spectra of halogenated organic compounds. *J. Chem. Phys.* **2013**, *139*, 074310.

[255] Finley, J.; Malmqvist, P.-Å.; Roos, B. O.; Serrano-Andrés, L. The multi-state CASPT2 method. *Chem. Phys. Lett.* **1998**, *288*, 299–306.

[256] Aquilante, F.; De Vico, L.; Ferré, N.; Ghigo, G.; Malmqvist, P.-Å.; Neogrády, P.; Pedersen, T.; Pitonak, M.; Reiher, M.; Roos, B.; Serrano-Andrès, L.; Urban, M.; Veryazov, V.; Lindh, R. MOLCAS 7: The Next Generation. *J. Comput. Chem.* **2010**, *31*, 224–247.

[257] Veryazov, V.; Widmark, P.-O.; Serrano-Andres, L.; Lindh, R.; Roos, B. 2MOLCAS as a development platform for quantum chemistry software. *Int. J. Quantum Chem.* **2004**, *100*, 626–635.

[258] Karlström, G.; Lindh, R.; Malmqvist, P.-Å.; Roos, B. O.; Ryde, U.; Veryazov, V.; Widmark, P.-O.; Cossi, M.; Schimmelpfennig, B.; Neogràdy, P.; Seijo, L. MOLCAS: a program package for computational chemistry. *Comput. Mater. Sci.* **2003**, *28*, 222–239.

[259] Caswell, D. S.; Spiro, T. G. Ultraviolet Resonance Raman Spectroscopy of Imidazole, Histidine, and Cu(imidazole)$_4{}^{2+}$: Implications for Protein Studies. *J. Am. Chem. Soc.* **1986**, *108*, 6470–6477.

[260] Balakrishnan, G.; Jarzecki, A. A.; Wu, Q.; Kozlowski, P. M.; Wang, D.; Spiro, T. G. Mode Recognition in UV Resonance Raman Spectra of Imidazole: Histidine Monitoring in Proteins. *J. Phys. Chem. B* **2012**, *116*, 9387–9395.

[261] Jones, C. M.; Asher, S. A. Ultraviolet resonance Raman study of the pyrene S4, S3, and S2 excited electronic states. *J. Chem. Phys.* **1988**, *89*, 2649–2661.

[262] Neugebauer, J.; Baerends, E. J.; Efremov, E. V.; Ariese, F.; Gooijer, C. Combined Theoretical and Experimental Deep-UV Resonance Raman Studies of Substituted Pyrenes. *J. Phys. Chem. A* **2005**, *109*, 2100–2106.

[263] Jensen, L.; Schatz, G. C. Resonance Raman Scattering of Rhodamine 6G as Calculated Using Time-Dependent Density Functional Theory. *J. Phys. Chem. A* **2006**, *110*, 5973–5977.

[264] Malmqvist, P.-O. W. P.-Å.; Roos, B. O. Density matrix averaged atomic natural orbital (ANO) basis sets for correlated molecular wave functions. *Theor. Chim. Acta* **1990**, *77*, 291–306.

[265] Angeli, C.; Pastore, M. The lowest singlet states of octatetraene revisited. *J. Phys. Chem.* **2011**, *134*, 184302.

[266] Biczysko, M.; Panek, P.; Scalmani, G.; Bloino, J.; Barone, V. Harmonic and Anharmonic Vibrational Frequency Calculations with the Double-Hybrid B2PLYP Method: Analytic Second Derivatives and Benchmark Studies. *J. Chem. Theory Comput.* **2010**, *6*, 2115–2125.

[267] Milgrom, L. R. *The Colours of Life: An Introduction to the Chemistry of Porphyrins and Related Compounds*; Oxford University Press: Oxford, U.K., 1997.

[268] Robert, B. Resonance Raman spectroscopy. *Photosynth. Res.* **2010**, *101*, 147–155.

[269] Premvardhan, L.; Robert, B.; Beer, A.; Büchel, C. Pigment organization in fucoxanthin chlorophyll a/c2 proteins (FCP) based on resonance Raman spectroscopy and sequence analysis. *Biochim. Biophys. Acta* **2010**, *1797*, 1647–1656.

[270] Hanf, R.; Tschierlei, S.; Dietzek, B.; Seidel, S.; Hermann, G.; Schmitt, M.; Popp, J. Probing the structure and Franck–Condon region of protochlorophyllide a through analysis of the Raman and resonance Raman spectra. *J. Raman Spectrosc.* **2010**, *41*, 414–423.

[271] Du, H.; Fuh, R.-C. A.; Li, J.; Corkan, L. A.; Lindsey, J. S. PhotochemCAD: A Computer-Aided Design and Research Tool in Photochemistry. *Photochem. Photobiol.* **1998**, *68*, 141–142.

[272] Vassiliev, S.; Bruce, D. Toward understanding molecular mechanisms of light harvesting and charge separation in photosystem II. *Photosynth. Res.* **2008**, *97*, 75–89.

[273] Liu, J.; Liang, W. Analytical Hessian of electronic excited states in time-dependent density functional theory with Tamm-Dancoff approximation. *J. Chem. Phys.* **2011**, *135*, 014113.

[274] Liu, J.; Liang, W. Analytical approach for the excited-state Hessian in time-dependent density functional theory: Formalism, implementation, and performance. *J. Chem. Phys.* **2011**, *135*, 184111.

[275] Barone, V.; Scalmani, I. C. G. Computational Spectroscopy of Large Systems in Solution: The DFTB/PCM and TD-DFTB/PCM Approach. *J. Chem. Theory Comput.* **2013**, *9*, 2052–2071.

[276] Reimers, J. R. A practical method for the use of curvilinear coordinates in calculations of normal-mode-projected displacements and Duschinsky rotation matrices for large molecules. *J. Chem. Phys.* **2001**, *115*, 9103.

[277] Borrelli, R.; Peluso, A. The electron photodetachment spectrum of c-$C_4F_8^-$: A test case for the computation of Franck-Condon factors of highly flexible molecules. *J. Chem. Phys.* **2008**, *123*, 044303.

[278] Borrelli, R.; Capobianco, A.; Peluso, A. Franck-Condon factors-Computational approaches and recent developments. *Can. J. Chem.* **2013**, *91*, 495–504.

[279] Avila Ferrer, F. J.; Santoro, F. Comparison of vertical and adiabatic harmonic approaches for the calculation of the vibrational structure of electronic spectra. *Phys. Chem. Chem. Phys.* **2013**, *14*, 13549–13563.

Publications

1. Egidi, F.; Giovannini, T.; Piccardo, M.; Bloino, J.; Cappelli, C; Barone, V. Stereo-electronic, vibrational, and environmental contributions to polarizabilities of large molecular systems: a feasible anharmonic protocol. *J. Chem. Theory Comput.* **2014**, *10*, 2456–2464

2. Egidi, F.; Bloino, J.; Cappelli, C.; Barone, V. Development of a Virtual Spectrometer for Chiroptical Spectroscopies: The Case of Nicotine. *Chirality* **2013**, *25*, 701–708

3. Egidi, F.; Bloino, J.; Cappelli, C.; Barone, V. A robust and effective time-independent route to the calculation of Resonance Raman spectra of large molecules in condensed phases with the inclusion of Duschinsky, Herzberg-Teller, anharmonic, and environmental effects. *J. Chem. Theory Comput.* **2014**, *10*, 346–363

4. Egidi, F.; Bloino, J.; Cappelli, C.; Barone, V.; Tomasi, J. Tuning of NMR and EPR parameters by vibrational averaging and environmental effects: an integrated computational approach. *Mol. Phys.* **2013**, *111*, 1345–1354

5. Egidi, F.; Bloino, J.; Barone, V.; Cappelli, C. Toward an Accurate Modeling of Optical Rotation for Solvated Systems: Anharmonic Vibrational Contributions Coupled to the Polarizable Continuum Model. *J. Chem. Theory Comput.* **2012**, *8*, 585–597

6. Lipparini, F.; Egidi, F.; Cappelli, C.; Barone, V. The Optical Rotation of Methyloxirane in Aqueous Solution: A Never Ending Story? *J. Chem. Theory Comput.* **2013**, *9*, 1880–1884

7. Lessi, M.; Manzini, C.; Minei, P.; Perego, L. A.; Bloino, J.; Egidi, F.; Barone, V.; Pucci, A.; Bellina, F. Synthesis and Optical Properties of Imidazole-Based Fluorophores having High Quantum Yields. *ChemPlusChem* **2014**, *79*, 366–370

8. Barone, V.; Biczysko, M.; Bloino, J.; Egidi, F.; Puzzarini, C. Accurate structure, thermodynamics, and spectroscopy of medium-sized radicals by hybrid coupled cluster/density functional theory approaches: The case of phenyl radical. *J. Phys. Chem.* **2013**, *138*, 234303

Acknowledgements

The work presented here is hardly the result of my effort alone, and should more truthfully be described as a collaborative project. Most of it was in fact born out of the collaboration between my two *sensei*, Chiara Cappelli and Vincenzo Barone. Yet, more people were involved in this work in many different ways: the first to be acknowledged is no doubt Julien Bloino who, among other things, oversaw all the coding. I am also very grateful for the help I received from Goska Biczysko, who gave me very useful suggestions for the computational part. But there are others whom I cannot fail to mention: Ivan Carnimeo, Mireia Segado, Matteo Piccardo, Nicola De Mitri, Giordano Mancini, and many more, too many to be listed. Suffice it to say that without the collective effort of all these people, there would be very little to present, and for that I am grateful.